Universiteit Antwerpen
Faculteit Wetenschappen
Departement Fysica

Superconductivity in Nanofilms and Nanocylinders

Supergeleiding in Nanofilms en Nanocilinders

Proefschrift voorgelegd tot het behalen van de graad van
Doctor in de Wetenschappen
aan de Universiteit Antwerpen, te verdedigen door

Yajiang Chen

Promotoren
Dr. A. A. Shanenko
Prof. Dr. F. M. Peeters

Antwerpen
June, 2012

Members of the Jury:

Chairman
Prof. Dr. Staf Van Tendeloo, Universiteit Antwerpen, Belgium

Members
Prof. Dr. Jacques Tempère, Universiteit Antwerpen, Belgium
Dr. Arkady Shanenko (Promoter), Universiteit Antwerpen, Belgium
Prof. Dr. Francois Peeters (Promoter), Universiteit Antwerpen, Belgium
Dr. Rolando Saniz, Universiteit Antwerpen, Belgium
Prof. Dr. Andrea Perali, University of Camerino, Italy
Prof. Dr. Mauro Doria, Universidade Federal do Rio de Janeiro, Brazil

Contact Information

Yajiang Chen
Universiteit Antwerpen
Departement Fysica
Groenenborgerlaan 171
2020 Antwerpen
België
Yajiang.Chen@ua.ac.be

Acknowledgments

Since I was in the second grade of middle school, I am amused by nature and it has been my dream to do scientific research. At that time, I even had an interesting idea that I might buy an optical microscope with all my gift money (which was the money I received during every Chinese New Year from my parents and relative) and discover what is going on in all kinds of biological cells. Fifteen years have passed since then, eventually I got bachelor degree of Science in Physics and master degree of Nanophysics. At this moment, I am finishing my doctoral thesis which is the biggest challenge in my life up to now. All of these could not be done without the help of my family, teachers, friends and classmates. I would like to express my heartfelt gratitude to all of them.

First of all, I would like to thank my promoters Dr. Arkady Shanenko and Prof. Dr. Francois Peeters, who provided me this precious opportunity to carry out my PhD study in the CMT group, and patiently guided me to the right way to do scientific research. Their infectious enthusiasm encourages me to choose fundamental scientific research as my future career. Moreover, with their massive erudition and preciseness, they set me excellent examples of what a good physicist should be like.

I am grateful to Prof. Dr. Milorad Milosevic for the nice collaboration, discussions and instructive suggestions to my research work. I also would like to thank Prof. Dr. Bart Partoens for his patient help on parallel programming and numerical methods. Hereby, I also want to thank Prof. Dr. Mauro Doria, who was my co-promoter during my master study in the CMT group, for his guidance and help.

It is my honor to study in the CMT group. Particular thanks to my officemate Dr. Roeland Geurts, Michael Barbier, Hemant Dixit, Andrey Kapra, Eduardo Galvan, Dr. Golibjon Berdiyorov, Dr. Kwinten Nelissen, Dr. An Slachmuylders and our IT support Nikolas Garofil, for their help on my work and study.

时光飞逝，转眼留学比利时已近六年。零六年九月十二日清晨踏上全然陌生的异国土地时的那种感觉，仍记忆犹新。留学生活不易，衷心地感谢同窗多年的谭海燕，赵海军，李斌和王斌杰，很幸运能够和你们一起出国留学；也感谢安特大学物理系的师兄弟姐妹们：徐贲，柯小行，麦振华，孙栋，曹姗姗，张亮，梁多多，田贺，梁灵志，林南省，石慧，凌云，刘超宇，张凌峰，在生活和工作中给予的热情细心的帮助和照顾。同时，对郝运铼师兄表示深深的怀念，愿师兄在天国安好。另外，很荣幸能够和周世平教授，查国桥教授，苟富军博士，张振中博士，朱家骥博士，娄文凯博士，敖志敏夫妇，李爽博士，许英教授，杨翠红教授，杨雯博士，董海明博士，李龙龙博士，李吉吉(Zhe)，李瑾俞，张斌，虞枫，潘菊富，杨志，相识于安特。感谢浙江大学的张孝彬教授，沙健教授和我的本科导师罗民兴教授，给了我留学比利时的珍贵机会和宝贵的留学忠告。

最后，感谢我的父母和亲人对我的养育和教导， 感谢我的夫人，黄海燕女士，长期以来对我的支持，帮助和鼓励！

Yajiang Chen
May 2012

Contents

1

Introduction

Due to the significant progress in nanofabrication, *high-quality* superconducting metallic nanofilms and nanowires are now attainable where effects due to quantum confinement are not destroyed or shadowed by the scattering on structural imperfections and impurities. As a result, such nanoscale superconducting systems may have properties significantly different as compared to bulk superconductors. Their potential applications in microscopic electronic circuits and nano-sensors require a solid knowledge of the geometrical and magnetic effects on nanoscale superconductivity.

Recently, single-crystalline metallic nanofilms [1–7] and single-crystalline and polycrystalline nanowires [8–12] have been fabricated. In particular, robust superconductivity in single-crystalline Pb and In nanofilms has been observed even for film thickness down to one atomic layer [13]. This is opposed to previously investigated metallic films where superconductivity was strongly suppressed due to significant structural imperfections and impurities. For nanowires, their quality and crystalline structure are also crucial for their superconducting properties. In particular, amorphous MoGe nanowires [14] exhibit a pronounced decrease of the critical temperature T_c when decreasing the nanowire width. Here the electron mean free path is significantly smaller than the diameter of the nanowire. On the contrary, the polycrystalline (but made of strongly coupled grains) Al nanowires [9, 15] and single-crystalline Sn [16] and Pb [17]) nanowires exhibit an increase of T_c with decreasing width of the nanowire. The electron mean free path in the high-quality nanowires is larger than or compatible to the nanowire diameter. Similarly, the mean free path in single-crystalline metallic nanofilms exceeds the nanofilms thickness (see e.g., [2]). Thus, a remarkable feature of both high-quality nanofilms

and nanowires is that the transverse (perpendicular) electron motion is not significantly influenced by scattering on imperfections.

In this case the single-particle energy spectrum is discretized in the transverse (perpendicular) quantum-confined direction due to the formation of discrete electron levels. As a result, the conduction band splits up into a series of single-electron subbands, and the bottom of each subband measures the corresponding discrete energy. The existence of the subband structure in nanofilms has been confirmed by angle-resolved photoemission spectroscopy of atomically uniform Ag nanofilms on Fe(111) [18], and by scanning tunneling spectroscopy of Pb nanofilms on Si(111) [5, 19]. The single-electron subbands shift in energy when changing the nanofilm thickness of the nanowire width. When the bottom of a subband passes through the Fermi surface, an increase in density of the contributing single-electron states occurs which leads to an enhancement of the superconducting order parameter and other basic superconducting characteristics, i.e., *the superconducting resonance* predicted by Blatt and Thompson more than 50 years ago [20]. As a result, the superconducting properties oscillate with the thickness, i.e., *quantum-size oscillations*. The subsequent 40 years after the paper by Blatt and Thompson [20], very few experimental groups reported the observation of possible signatures of such behavior. Structural defects were a serious obstacle preventing a definite conclusion that time. Recently, such oscillations of the critical superconducting temperature and critical magnetic field were finally observed with high accuracy in single-crystalline Pb nanofilms [3, 5, 19, 21]. This renewed interest in the interplay of quantum confinement with superconductivity. In particular, it was predicted that quantum confinement results in: (i) the formation of Andreev-type quasiparticles [22]; (ii) in the cascade scenario of the superconducting-to-normal transition [23]; (iii) in an enhanced spatially distributed pair condensate [20, 22–27], etc. Motivated by significant experimental achievements and recent theoretical developments, in this thesis we concentrate on the key question: *What is the effect of the quantum confinement on superconductivity of high-quality nanofilms and nanowires?* This thesis is focused on the clean limit and based on a numerical solution of the Bogolibov-de Gennes (BdG) equations arranged for a superconducting nanoslab (modeling the nanofilm) and for superconducting nanocylinder and hollow nanocylinder (modeling the nanowire).

The present thesis is organized as follows:

Chapter 1 introduces a brief historical survey of superconductivity and outlines the phenomenological London and Ginzburg-Landau equations. Furthermore, the microscopic theories including the Bardeen-Cooper-Schrieffer (BCS) theory, the BdG equations and spin-generalized BdG equations are discussed, and the numerical approaches to solving these equations are described. In the last part of this chapter, two kinds of nanofabrication technologies, i.e., the molecular beam epitaxy and the lift-off lithography, are introduced, as well as the scanning tunneling spectroscopy.

Chapter 2 is focused on the effect of the spatially dependent Hartree-Fock potential in the BdG equations on the superconducting order parameter $\Delta(\mathbf{r})$ and the critical temperature T_c. In bulk superconductors, the Hartree-Fock mean-field potential is spatially uniform and so gives the same contribution to both the single-electron energies and to the chemical potential. Thus, $\Delta(\mathbf{r})$ and T_c that depend on the single-electron energies measured from the chemical potential, is unaltered when switching on the Hartree-Fock interaction. This is not the case in nanosized superconductors where the presence of quantum confinement breaks the translational invariance. Investigating a nanocylinder, we find that the curve representing the thickness-dependent oscillations of the critical superconducting temperature is shifted up to larger diameters in the presence of the spatially dependent Hartree-Fock field.

In **Chapter3** we study multi-band(subband) superconductivity in a hollow nanocylinder. When changing the inner radius and thickness of the hollow nanocylinder, we find a crossover from an irregular pattern of quantum-size superconducting oscillations typical of nanowires to an almost regular regime specific for superconducting nanofilms. We show that the formation of single-electron subbands results in multiple superconducting gaps due to the interplay between quantum confinement and the Andreev-reflection mechanism. The difference between the subband superconducting gaps is significant in the irregular regime (which is similar to the pattern of quantum-size oscillations of the superconducting gap shown in typical nanowires) but the gaps are almost equal when coming to the regular side of the crossover. Here the ratio of the energy gap to the critical temperature approaches its bulk value while it is reduced by 20%-30% because of the confinement-driven Andreev-type states proliferating in the irregular regime.

In **Chapter 4** we investigate the superconductor-to-normal transition driven by a parallel magnetic field in a superconducting hollow nanocylinder. In particular, we show that the formation of multiple single-electron subbands results in the cascade scenario of the superconductor-to-normal transition. When increasing the parallel magnetic field, the order parameter decays through a cascade of jumps, and each jump is associated with the onset of the depairing in one of the occupied subbands. Such quantum-size cascades vary with the confining geometry i.e., when changing the inner radius (R) and wall thickness (d) of the hollow nanocylinder. The jumps in the order parameter as function of the magnetic field become less pronounced when increasing the ratio R/d, i.e., when the nanofilm-like regime is approached. We also investigate the thermal smoothing of the cascades and the smoothing that occurs due to surface roughness.

Chapter 5 describes an intriguing possibility of molecule-like superconducting pairing in single-crystalline superconducting nanofilms. Quantum confinement of the perpendicular motion of electrons results in the formation of a series of single-electron subbands. The energetic position of each subband

can vary significantly with changing nanofilm thickness, substrate material, protection cover and other details of the fabrication process. One may realize the situation that the bottom of one of the available subbands is situated in the vicinity of the Fermi level. We demonstrate that the character of the superconducting pairing in such a subband changes dramatically and exhibits a clear molecule-like trend, which is very similar to the crossover from the BCS regime to Bose-Einstein condensation observed in trapped ultracold fermions. For Pb nanofilms with thickness of 4 and 5 monolayers this will lead to a spectacular scenario: up to half of all the Cooper pairs nearly collapse i.e., their in-plane radius shrinks down to a few nanometers.

In **Chapter 6** we investigate the impact of the thickness-dependent variations of the phonon mediated electron-electron coupling on the critical temperature and excitation gap in single-crystalline superconducting nanofilms. To date, several experimental groups reported measurements of the thickness dependence of T_c in atomically uniform single-crystalline Pb nanofilms. The reported amplitude of the T_c-oscillations varies significantly from one experiment to another. Here we demonstrate that the reason for this unresolved issue is an interplay of the quantum-size variations in the single-electron density of states with thickness-dependent oscillations in the phonon mediated electron-electron coupling. Such oscillations in the coupling depend on the substrate material, the quality of the interface, the protection cover and other details of the fabrication process, changing from one experiment to another. This explains why the available data do not exhibit one-voice consistency about the amplitude of the T_c-oscillations.

In **Chapter 7** we investigate a single-vortex numerical solution of the BdG equations for a two-band s-wave superconductor quantum-confined in a cylinder with radius of about the Ginzburg-Landau coherence length. We calculate the healing lengths of the two band condensates and determine how they depend on temperature and the interband Josephson-like coupling γ. We show that two-band superconductors harbor hidden criticality deep in the superconducting state, stemming from the critical temperature of the weaker band taken as an independent system. For sufficiently small interband coupling γ the coherence length of the weaker band exhibits a remarkable deviation from the conventional monotonic increase with temperature, namely, a pronounced peak close to the hidden critical point.

1.1 INTRODUCTION TO SUPERCONDUCTIVITY

1.1.1 Historical survey

Superconductivity was first observed in 1911 by Heike Kamerkingh Onnes [28]. When he cooled mercury to the temperature of liquid helium around 4.2 K, its electrical resistance suddenly disappeared rather than gradually as seen in Fig. 1.1. This phenomenon was called *superconductivity*, and the transition temperature is called the critical temperature T_c. Two year later, he was awarded the Nobel Prize in Physics "for his investigations on the properties of matter at low temperatures which led, inter alia, to the production of liquid helium". In more accurate experiments, it was found that the resistivity of bulk superconductors is zero at the level of $10^{-24}\,\Omega\,\mathrm{cm}$, which is 15 orders of magnitude less than the resistance of high-purity copper at 4.2 K [29]. Besides mercury, many other metals (e.g., lead, tin, aluminum, etc.), alloys and intermetallic compounds also become superconducting as the temperature drops to a certain value. In superconductors, once an electric current has been set up it will persist for ever. Such non-dissipative current is called supercurrent. Superconductors were simply regarded as ideal conductors with zero resistance, until the discovery of the Meissner-Ochsenfeld effect.

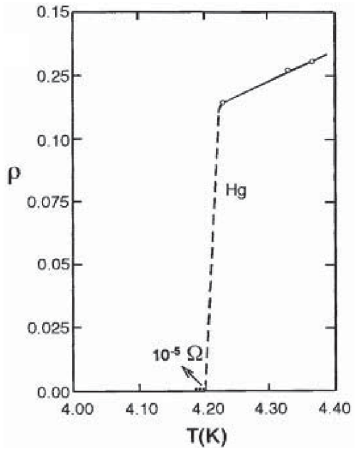

Fig. 1.1 Resistance versus temperature of mercury measured in 1911 [28].

In 1933, Walter Meissner and Robert Ochsenfeld discovered that a macroscopic superconductor repels a magnetic field if it is relatively weak [30] as shown in Fig. 1.2. Such repulsion of magnetic flux is independent of the sample's history, i.e., the sequence of applying of the magnetic field and adjusting the temperature. It means that the superconducting state is a new thermodynamical state and the transition from the normal state to the super-

conducting state can be treated as a phase transition. It was also found that superconductivity can be destroyed when increasing the external magnetic field up to a certain value, which is called the critical magnetic field H_c. The Meissner-Ochsenfeld effect shows that the superconducting state has a lower free energy than the normal state. From the analysis of the entropy [29] of a superconductor and the empirical temperature dependence of H_c, one can find that the superconducting state is more ordered than the normal state, and in the presence of a magnetic field all the transitions from the superconducting state to the normal state are first-order phase transitions, while without a magnetic field the transition at the critical temperature is a second-order phase transition [29].

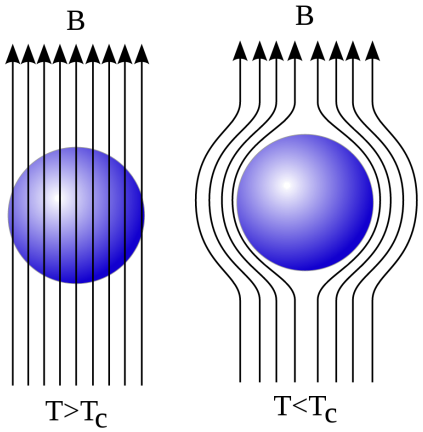

Fig. 1.2 In the left panel, a normal sphere sample is located in the presence of a relatively weak magnetic field in the left panel. In the right panel, the sample becomes superconducting and repulses the magnetic flux when cooling the temperature under T_c. For a ideal conductor, in this procedure the magnetic field remains inside of the sample as the temperature drops.

In 1935, Fritz and Heinz London represented two equations which can phenomenologically explain the above two basic electrodynamic properties [31]. These equations can be derived from the Drude model for the electrical conductivity and minimization of the free energy with respect to the external magnetic field [32]. In this theory, both the electric and magnetic fields are assumed to be weak enough, and the density of superconducting electrons is position-independent. Although London equations can not describe the spatial distribution of the density of the superconducting electrons, it introduces one of the most important characteristic lengths in superconductivity: the magnetic field penetration depth λ (see in Fig. 1.3).

In 1950, Ginzburg and Landau developed a very powerful phenomenological theory of superconductivity [33] based on the Landau's theory of second-order

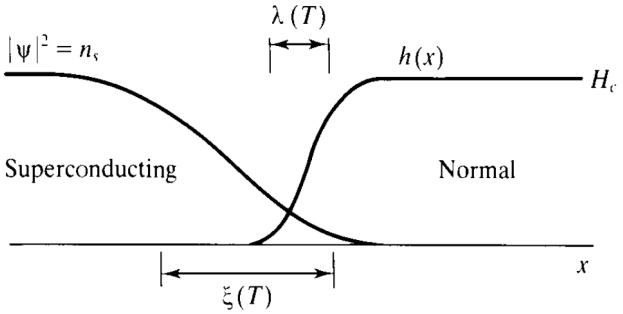

Fig. 1.3 Variations of square of the superconducting order parameter $\psi(x)$ and the external magnetic field $h(x)$ in the interface between the normal and superconducting domains [32]. $\xi(T)$ and $\lambda(T)$ are the temperature dependent coherence length and magnetic field penetration depth, respectively.

phase transitions. In 2003, Ginzburg won a shared Nobel Prize in Physics "for pioneering contributions to the theory of superconductors". The Ginzburg-Landau (GL) theory consists of two equations which are obtained by minimizing the free energy expanded in terms of the order parameter with respect to the fluctuations in the order parameter and the vector potential [32]. The physical meaning of the order parameter was explained by the later microscopic BCS theory, however, the square of its absolute value in GL theory is regarded as the density of the superconducting electrons. Without exploring the underlying microscopic mechanism of superconductivity, this theory correctly describes some of the superconducting phenomenon and introduces both of the two characteristic lengths in superconductivity (see in Fig. 1.3): the magnetic field penetration depth λ and the coherence length ξ which characterizes the spatial variations of the order parameter. The GL theory is valid in the vicinity of T_c.

In 1957, John Bardeen, Leon Cooper, and John Schrieffer proposed the first widely-accepted microscopic theory for superconductivity, i.e., *BCS theory* [34]. They were awarded jointly the Nobel Prize in Physics 1972 "for their jointly developed theory of superconductivity, usually called the BCS-theory". The superconductors well described by this theory are called the conventional superconductors or BCS superconductors, differing from the high-T_c superconductors. The foundation of the BCS theory is that electrons in the Debye window around the Fermi level with opposite momenta and spins are bounded into Cooper pairs due to the attractive electron-electron interaction mediated by phonons. Based on the trial wave function of the ground state of superconductivity, BCS theory gives the difference in energy between the superconducting state and the normal state, the temperature dependent energy gap in the energy spectrum and density of states of quasiparticles, the ground state

of superconductivity, and so on. In contrary to the Ginzburg-Landau theory, BCS theory works at all the temperature bellow T_c, and has been extended for inhomogeneous superconductivity, known as the BdG equations [35] which is the major theory applied in this thesis.

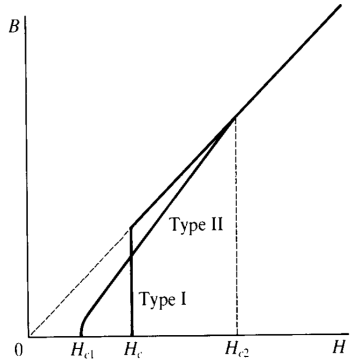

Fig. 1.4 The magnetic induction **B** (i.e., the flux per area) as a function of the external magnetic field **H** in type I and type II superconductors [32].

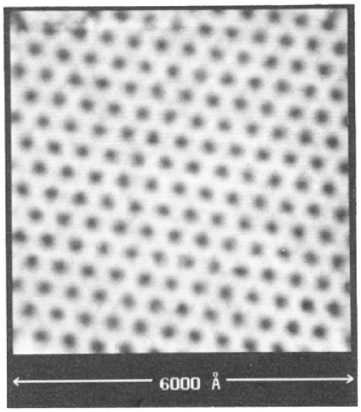

Fig. 1.5 Abrikosov flux lattice (vortex array) produced by a magnetic field $H = 1$ T in $NbSe_2$ [36].

It was in the same year that Abrikosov classified the superconductors as type I and type II (see in Fig. 1.4) according to the parameter $\kappa = \lambda/\xi$ and predicted the existence of vortex array (see in Fig. 1.5) in the mixed state of type II superconductors [37] which was confirmed in experiment in 1967 [38]. Abrikosov won a shared Nobel Prize in Physics "for pioneering contributions to the theory of superconductors" in 2003. For a type I superconductor,

with increasing the external magnetic field the system exhibits only Meissner-Ochsenfeld effect before superconductivity is destroyed, i.e., the field reaches H_c. For a type II superconductor, under a certain magnetic field H_{c1} (the lower critical magnetic field) the system shows Meissner-Ochsenfeld effect. With increasing the field, the magnetic flux deeply penetrates the sample and coexists with the superconductivity. When the magnetic field reaches a certain value H_{c2} (the upper critical field) the superconductivity of the sample is destroyed. By using Green functions, Lev Petrovich Gor'kov showed in 1959 that in the case of a contact interaction of the electron-electron coupling, the GL theory is in fact a limiting form of the BCS theory in the vicinity of T_c and the order parameter in the GL theory is proportional to the energy gap in the BCS theory.

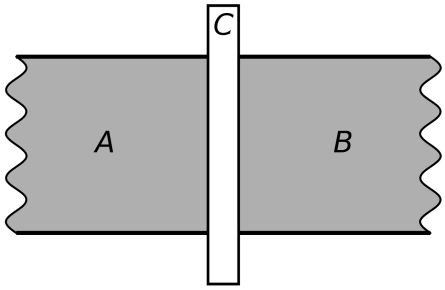

Fig. 1.6 Single Josephson junction with A, B superconductors and C a thin insulator.

In 1962, Brian Josephson predicted that the electric current can flow between two superconductors even when they are separated by a very thin insulator (i.e., Josephson junction as seen in Fig. 1.6) without any voltage applied [39]. This was verified two year later by P. W. Anderson and A. H. Dayem [40]. Josephson won a half of the Nobel Prize in Physics in 1972 "for his theoretical predictions of the properties of a supercurrent through a tunnel barrier, in particular those phenomena which are generally known as the Josephson effects". Josephson effects exhibit the importance of the phase difference between the GL complex order parameter of the two superconductors composing the junction, and has plenty of practical applications, e.g. the superconducting quantum interference device (SQUID) and superconducting qubits.

In 1986, Alex Müller and Georg Bednorz discovered the first *high-T_c superconductor* the layered copper oxide BaLaCuO with T_c about 35 K [41]. The next year, they were awarded the Nobel Prize in Physics "for their important break-through in the discovery of superconductivity in ceramic materials". High-T_c superconductors belong to the type II superconductors. Many other high-T_c superconductors have been found, subsequently. In 1987, YBCO was discovered to be superconducting with a T_c of 90 K and an estimated

H_{c2} between 80 and 180 T [42]. In 1988, $Bi_2Sr_2Ca_2Cu_3O_{10+x}$ (Bi-2223) and $Tl_2Ba_2Ca_2Cu_3O_{10}$ (Tl-2223) were discovered to have T_c equal to 105 K [43] and 120 K [44], respectively. In 1993, mercury barium calcium copper oxide $HgBa_2Ca_2Cu_3O_{8+x}$(Hg-1223) was found to be superconducting with T_c equal to 135 K [45]. One year later, it was found that under high pressure, its T_c can even reach 164 K [46], which is the highest T_c up to now. The complex physics of the high-T_c superconductors can not be explained by the BCS theory. Comparing with the BCS superconductors, the high-T_c superconductors have much higher T_c, and the anomalous normal states in the underdoped regim which strongly deviates from the Fermi liquid picture. It is generally believed that the superconductivity in high-T_c superconductors can emerge from electron-electron repulsive interaction [47]. Although there are intensive research and many achievements in characterization and theoretical model, the mechanism that causes the superconductivity in high-T_c superconductors is one of the major unsolved problems of the theoretical condensed matter physics.

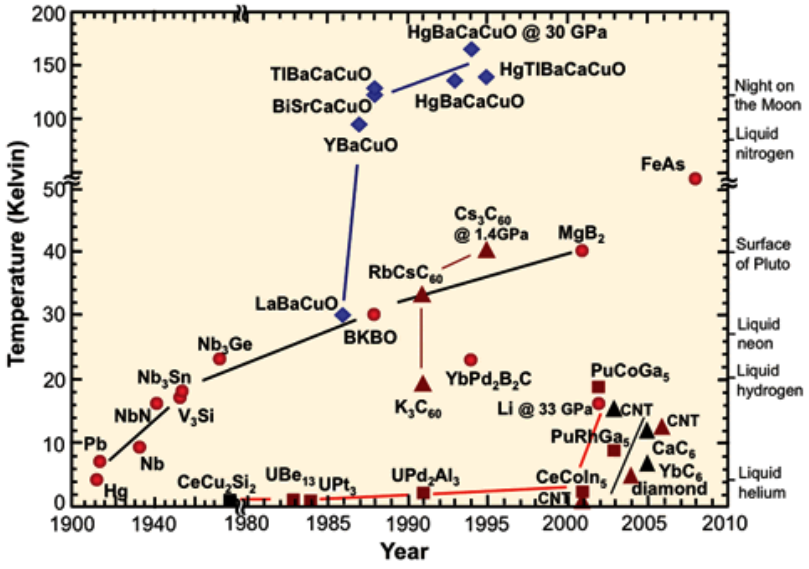

Fig. 1.7 The time line of the T_c of superconductors according to the data from the Department of Energy of the United States - Basic Energy Sciences (see http://www.ccas-web.org/superconductivity/).

Recently, many other kinds of superconductors have been discovered, such as superconducting 4 Å single-walled carbon nanotubes with $T_c = 20$ K [48], heavy fermion superconductors (e.g., PuCoGa5 with $T_c = 18.5$ K [49] and PuRhGa5 with $T_c = 8.7$ K [50]), two-band superconductor MgB_2 with highest $T_c = 39$ K [51] which is the highest T_c of the phonon-mediated supercon-

ductors, crystalline C_{60} fullerenes with $T_c = 40$ K [52], iron-based superconductors (e.g., LaFePO with $T_c = 4$ K [53] and LaFeAs(O,F) with $T_c = 43$ K under pressure [54]) which can be useful to form another family of non-BCS superconductors.

1.1.2 Applications of superconductivity

Superconductivity which shows a macroscopic quantum effect is one of the great scientific discoveries of the 20th Century. By utilizing its fascinating and unexpected properties, superconductivity has already led to many new commercial products that are of importance in human's daily life and in scientific research, such as magnetic resonance imaging (MRI), nuclear magnetic resonance (NMR), magnetic levitation (i.e., maglev), high intersity magnets for high-energy physics accelerators, plasma fusion reactors, superconducting wires, etc. Besides these, the ongoing development of new applications includes superconducting transformers, underground cables, more rapid and efficient magnetically levitated trains and railway traction transformers, more compact and less costly MRI systems, powerful magnets for the industry, etc. Compared with conventional products, the superconductor-base products are extremely environmentally friendly with no greenhouse gases, since they are cooled by non-flammable liquid nitrogen or helium. Here we briefly introduce the principles behind these applications.

The property of zero resistance of the electric current is exploited in applications, such as superconducting wires made of niobium-titanium or high-T_c superconductors (e.g., YBCO). Superconducting wires have higher maximum current densities and zero power dissipation in comparison with copper or aluminum. The ribbon-shaped YBCO wires made by the American Superconductor company with 100 meters long and just 4-mm wide can carry a current of up to 140 Amperes when cooled with liquid nitrogen (i.e., at temperature of about 77 K), which is about 150 times as much as a standard copper wire of the same dimension can carry. Additionally, such wires become superconducting magnets with high magnetic fields when made into coils and subject to a strong supercurrent. In 2007, the US National Research Council made a magnet with windings of YBCO which achieved a magnetic field of 26.8 T. The superconducting magnets are the basis of some other applications, e.g., magnetic levitation, MRI machine and high-energy Physics accelerators.

Based on superconducting loops with two Josephson junctions, the direct current superconducting quantum interference device (DC SQUID, as seen in Fig. 1.8) is the most sensitive magnetometer with an accuracy as high as 5×10^{-18} T. For comparison, the earth's magnetic field is of the order of 10^{-4} T, and some processes in animals produce magnetic fields between 10^{-9} T and 10^{-6} T. The extreme sensitivity of SQUIDs makes them play an important role in many different fields. Magnetoencephalography (MEG) in diagnostic medicine uses an array of SQUIDs to measure the weak magnetic field in brains or stomachs, and the MRI uses SQUIDs as detectors. Another

case is the scanning SQUID microscope, which also uses a SQUID as probe. This kind of detectors is applied in oil prospecting, mineral exploration, earthquake prediction and geothermal energy surveying, even in the detection of gravitational waves.

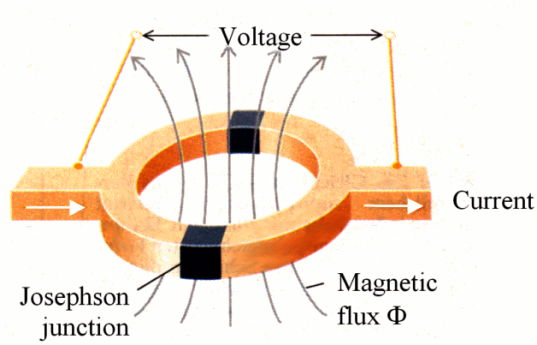

Fig. 1.8 Illustration of a superconducting quantum interference device (SQUID).

With the increase of the critical temperature of high-T_c superconductors, it is widely believed that more reliable and efficient superconducting products will emerge.

1.2 MICROSCOPIC THEORIES OF SUPERCONDUCTIVITY

1.2.1 BCS theory

As the first well accepted microscopic theory for superconductivity, the BCS theory has achieved huge success in explaining the superconductivity of type I and type II superconductors. Even in high-temperature superconductors, many experiments, e.g., AC Josephson effect, Little-Parks oscillations, Andreev reflection, etc., have shown that the effective charge of the supercurrent carriers is twice the electron charge, i.e., the superconducting electrons with opposite momenta and spins are bounded together as Cooper pairs, like in the case of BCS superconductors. To some extent, the concept of Cooper pairs and their quantum overlap is the core of the BCS theory to form a new coherent state. In general, there are many pairing mechanisms besides the so-called s-wave pairing (i.e., attractive interactions between electrons in momentum space is isotropic), but in this thesis only s-wave pairing is taken into account since we focus on the properties of nanostructures made of conventional metallic superconductors. In this subsection, first the BCS reduced Hamiltonian is obtained from the effective electron-phone interaction following the treatment of de Gennes [35]. Second, Cooper pairs are introduced based on the reduced Hamiltonian. At last, we deduce the ground state, the condensed energy and

the gap energy of the quasiparticle spectrum for a homogenous superconductor at zero temperature. The case of finite temperature will be discussed in Subsection 1.2.2.

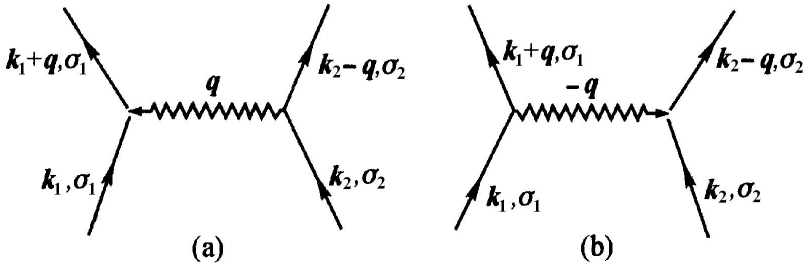

Fig. 1.9 Phonon mediated electron-electron interaction. (a) The electron ($\mathbf{k}_2$, σ_2) emits a phonon of wave vector $\mathbf{q}$, absorbed by the electron ($\mathbf{k}_1$, σ_1). (b) The electron ($\mathbf{k}_1$, σ_1) emits a phonon of wave vector $-\mathbf{q}$, absorbed by the electron ($\mathbf{k}_2$, σ_2).

1.2.1.1 BCS reduced Hamiltonian The electron-phonon interaction was first proposed by Frölich in 1950. The mechanism can be described as follows, a virtual phonon emitted by an electron traveling through a crystal is absorbed by another electron (see Fig. 1.9). In fact the virtual phonon is the deformation or polarization of the crystal caused by one electron. When another electron passes through this region, it feels an attractive or repulsive interaction from the environment. In this way, the behavior of emission and absorption of a virtual phonon results in a retarded interaction between these two electrons. The Hamiltonian of such interaction is as follows,

$$H_{eff} = \frac{1}{2} \sum_{\substack{\mathbf{q},\mathbf{k}_1,\mathbf{k}_2, \\ \sigma_1,\sigma_2}} V_{\mathbf{k}_1,\mathbf{q}} C^+_{\mathbf{k}_1+\mathbf{q},\sigma_1} C^+_{\mathbf{k}_2-\mathbf{q},\sigma_2} C_{\mathbf{k}_2,\sigma_2} C_{\mathbf{k}_1,\sigma_1}, \tag{1.1}$$

where $\mathbf{k}_1$ and $\mathbf{k}_2$ are the wave vectors of electrons, $\mathbf{q}$ is the wave vector of the virtual phonon, σ_1 and σ_2 are the spins of electrons. C^+ and C are the creation and destruction operators of electrons, the interaction potential is of the form

$$V_{\mathbf{k}_1,\mathbf{q}} = 2|D_{\mathbf{q}}|^2 \frac{\hbar\omega_{\mathbf{q}}}{(\xi_{\mathbf{k}_1+\mathbf{q}} - \xi_{\mathbf{k}_1})^2 - (\hbar\omega_{\mathbf{q}})^2} \tag{1.2}$$

with $D_{\mathbf{q}}$ proportional to the ion-electron interaction, ξ the energy of electrons and ω_q the frequency of phonons. From Eq. (1.2), it is found that this interaction is attractive ($V_{\mathbf{k}_1,\mathbf{q}} < 0$) in the region $|\xi_{\mathbf{k}_1+\mathbf{q}} - \xi_{\mathbf{k}_1}| < \hbar\omega_{\mathbf{q}} \approx \hbar\omega_D$, while beyond this range it turns to be repulsive. ω_D is the Debye frequency. Taking into accout the screening Coulomb effect, the total interaction matrix element is obtained as $\frac{4\pi e^2}{\mathbf{q}^2+\mathbf{k}_s^2}(1+\frac{\omega_{\mathbf{q}}{}^2}{\omega^2-\omega_{\mathbf{q}}^2})$ (with $\mathbf{k}_s^2$ proportional to the electron density) in the jellium model. The BCS theory considers the total interaction

as attractive inside the Debye window around the Fermi level and approximately as constant $(-V)$, while the repulsive interaction outside the shell is neglected:

$$\begin{cases} V > 0 & \text{if } |\xi_{\mathbf{k}_1+\mathbf{q}} - \xi_{\mathbf{k}_1}| < \hbar\omega_D, \\ V = 0 & \text{otherwise.} \end{cases} \tag{1.3}$$

So the Hamiltonian of the total interaction between electrons is

$$H' = -\frac{1}{2} \sum_{\substack{\mathbf{q},\mathbf{k}_1,\mathbf{k}_2, \\ \sigma_1,\sigma_2}} V C^+_{\mathbf{k}_1+\mathbf{q},\sigma_1} C^+_{\mathbf{k}_2-\mathbf{q},\sigma_2} C_{\mathbf{k}_2,\sigma_2} C_{\mathbf{k}_1,\sigma_1}. \tag{1.4}$$

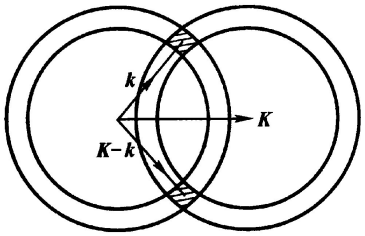

Fig. 1.10 The region (shadow) of the attractive electrons with wave vectors $\mathbf{K}$ and $\mathbf{K} - \mathbf{k}$.

Further, we transform the wave vectors $(\mathbf{k}_1, \mathbf{k}_2, \mathbf{q})$ to another three wave vectors $(\mathbf{K}, \mathbf{k}, \mathbf{k}')$ through the following relations,

$$\begin{aligned} \mathbf{K} &= \mathbf{k}_1 + \mathbf{k}_2, \\ \mathbf{k} &= \mathbf{k}_1, \\ \mathbf{k}' &= \mathbf{k}_1 - \mathbf{q}. \end{aligned} \tag{1.5}$$

As shown in Fig. 1.10, only the electrons occupying the $\mathbf{k}$ and $\mathbf{K} - \mathbf{k}$ states within the dashed region can be coupled by the attractive interaction. We take into account only the term with $\mathbf{K} = 0$ (i.e., $\mathbf{k}_1 = -\mathbf{k}_2$) because the dashed area reaches maximum and such term gives the most important contribution. On the other hand, the electron couple with opposite spins has lower energy than the one with the same spins due to the Pauli's exclusion principle. So, we take the spin indices in Eq. (1.4) as $\sigma' = -\sigma$. Thus, including the kinetic energy $(\xi_{\mathbf{k}})$ of electrons measured from the Fermi level E_F, the total Hamiltonian known as the BCS reduced Hamiltonian is written as

$$\hat{H} = \sum_{\mathbf{k},\sigma} \xi_{\mathbf{k}} C^+_{\mathbf{k}\sigma} C_{\mathbf{k}\sigma} - \sum_{\mathbf{k},\mathbf{k}'} V_{\mathbf{k}\mathbf{k}'} C^+_{\mathbf{k}'\uparrow} C^+_{-\mathbf{k}'\downarrow} C_{-\mathbf{k}\downarrow} C_{\mathbf{k}\uparrow}, \tag{1.6}$$

where the matrix element of the interaction $V_{\mathbf{k}\mathbf{k}'}$ can be approximated following the BCS theory

$$V_{\mathbf{k}\mathbf{k}'} = \begin{cases} V(>0) & \text{if } |\xi_{\mathbf{k}}| \text{ and } \xi_{\mathbf{k}'} < \hbar\omega_D, \\ 0 & \text{otherwise.} \end{cases} \tag{1.7}$$

The reason for the choice of the grand canonical Hamiltonian is that the number of electrons in the system is not conserved.

1.2.1.2 Cooper pair Now, we consider the scattering states of two coupled electrons with opposite momenta and spins above the Fermi level at $T = 0$ K. All the electrons under the Fermi level are considered as in the normal state and to be already occupied. The eigenstates $|\psi\rangle$ of the BCS reduced Hamiltonian are linear combination of all the possible scattering states, i.e.,

$$|\psi\rangle = \sum_{|\mathbf{k}|>k_F} a(\mathbf{k}) C^+_{\mathbf{k}\uparrow} C^+_{-\mathbf{k}\downarrow} |F\rangle, \tag{1.8}$$

with $|F\rangle$ the ground state (being $|F\rangle$ the Fermi sea filled by independent quasiparticles). The summation is taken over states with $0 < \xi_{\mathbf{k}} < \hbar\omega_D$, so following Eq. (1.7) we have $V_{\mathbf{k}\mathbf{k}'} = V$. The normalization condition on the eigenstates $|\psi\rangle$ determines a condition on $a(\mathbf{k})$, i.e., $\sum_{|\mathbf{k}|>k_F} |a(\mathbf{k})|^2 = 1$.

The energy of two coupled electrons (E) is obtained from the eigen-energies of the reduced Hamiltonian by removing the kinetic energy of the electrons under the Fermi level,

$$E = 2 \sum_{|\mathbf{k}|>k_F} \xi_{\mathbf{k}} |a(\mathbf{k})|^2 - V \sum_{|\mathbf{k}|,|\mathbf{k}'|>k_F} a^*(\mathbf{k}') a(\mathbf{k}). \tag{1.9}$$

By minimizing the quantity $E - \lambda(\sum_{|\mathbf{k}|>k_F} |a(\mathbf{k})|^2 - 1)$, being λ a Lagrangian multiplier, we obtain the following equation

$$(2\xi_{\mathbf{k}} - \lambda) a(\mathbf{k}) = V \sum_{|\mathbf{k}'|>k_F} a(\mathbf{k}'), \tag{1.10}$$

from which λ and E can be obtained. First, λ is found to be equal to E by multiplying $a^*(\mathbf{k})$ on both sides and summing over the wave vector $\mathbf{k}$. Second, by dividing $(2\xi_{\mathbf{k}} - \lambda)$ and summing over $\mathbf{k}$, we get

$$1 = V \sum_{|\mathbf{k}'|>k_F} \frac{1}{2\xi_{\mathbf{k}} - \lambda} = N(0) V \int_0^{\hbar\omega_D} \frac{\mathrm{d}\xi}{2\xi - E} \tag{1.11}$$

with $N(0)$ the density of states per volume and spin of electrons at the Fermi surface. In the weaking-coupling case $N(0)V \ll 1$, we have

$$E = -2\hbar\omega_D \, e^{-2/[N(0)V]}. \tag{1.12}$$

The negative total energy means that two electrons with opposite momenta and spins over the Fermi level form a bound state (called a Cooper pair) in the presence of a weak attractive interaction (even in the limit of vanishing V).

1.2.1.3 Ground state and energy gap According to the fact that the formation of Cooper pairs can lead to a lower energy in comparison with the case of two uncoupled electrons, Bardeen, Cooper and Schrieffer assumed that in the ground state of superconductivity all electrons are in the form of Cooper pairs. Although such assumption indicates an even number N of electrons in the system, it is still suitable for the discussion of an electron gas ($N \sim 10^{23}$) because if there is one uncoupled electron its effect on the physical properties can be neglected. The BCS trial wave function of the superconducting ground state is as follows,

$$|0\rangle = \prod_{\mathbf{k}} (u_{\mathbf{k}} + v_{\mathbf{k}} C^{+}_{\mathbf{k}\uparrow} C^{+}_{-\mathbf{k}\downarrow})|\text{Vac}\rangle, \tag{1.13}$$

where $|\text{Vac}\rangle$ is the vacuum state ($C_{\mathbf{k},\sigma}|\text{Vac}\rangle = 0$). Coefficients $u_{\mathbf{k}}$ and $v_{\mathbf{k}}$ taken to be real are the probability amplitudes of the unoccupied and occupied pairing state, respectively. The normalization condition for $u_{\mathbf{k}}$ and $v_{\mathbf{k}}$ is $u^2_{\mathbf{k}} + v^2_{\mathbf{k}} = 1$. In what follows, with the BCS reduced Hamiltonian Eq. (1.6) and the above trial wave function of the ground state, we minimize the total energy of the superconducting ground state $E_s = \langle 0|\hat{H}|0\rangle$ in order to obtain the total energy and coefficients $u_{\mathbf{k}}$ and $v_{\mathbf{k}}$.

By inserting Eqs. (1.6) and (1.13) into the expression of the energy of the ground state, we have

$$\begin{aligned} E_s &= \langle 0| \sum_{\mathbf{k},\sigma} \xi_{\mathbf{k}} C^{+}_{\mathbf{k}\sigma} C_{\mathbf{k}\sigma} - \sum_{\mathbf{k},\mathbf{k}'} V_{\mathbf{k}\mathbf{k}'} C^{+}_{\mathbf{k}'\uparrow} C^{+}_{-\mathbf{k}'\downarrow} C_{-\mathbf{k}\downarrow} C_{\mathbf{k}\uparrow} |0\rangle \\ &= 2\sum_{\mathbf{k}} \xi_{\mathbf{k}} v^2_{\mathbf{k}} + \sum_{\mathbf{k},\mathbf{k}'} V_{\mathbf{k}\mathbf{k}'} u_{\mathbf{k}} v_{\mathbf{k}} u_{\mathbf{k}'} v_{\mathbf{k}'}. \end{aligned} \tag{1.14}$$

Making use of the normalization condition for the real coefficients $u_{\mathbf{k}}$ and $v_{\mathbf{k}}$, we introduce the variable $\theta_{\mathbf{k}}$

$$u_{\mathbf{k}} = sin(\theta_{\mathbf{k}}) \text{ and } v_{\mathbf{k}} = cos(\theta_{\mathbf{k}}). \tag{1.15}$$

The minimization of the energy E in Eq. (1.14) with respect to $\theta_{\mathbf{k}}$ gives the relation

$$tan(2\theta_{\mathbf{k}}) = \sum_{\mathbf{k}'} V_{\mathbf{k}\mathbf{k}'} [sin(2\theta_{\mathbf{k}'})]/(2\xi_{\mathbf{k}}). \tag{1.16}$$

We define two new quantities

$$\Delta_{\mathbf{k}} = -\sum_{\mathbf{k}'} V_{\mathbf{k}\mathbf{k}'} u_{\mathbf{k}'} v_{\mathbf{k}'} = -\frac{1}{2} \sum_{\mathbf{k}'} V_{\mathbf{k}\mathbf{k}'} sin(2\theta_{\mathbf{k}'}), \tag{1.17}$$

$$\epsilon_{\mathbf{k}} = (\Delta^2_{\mathbf{k}} + \xi^2_{\mathbf{k}})^{1/2}, \tag{1.18}$$

where $\Delta_{\mathbf{k}}$ is the gap energy and $\epsilon_{\mathbf{k}}$ is the quasiparticle energy as we will see later. And, Eq. (1.16) is rewritten as

$$tan(2\theta_{\mathbf{k}}) = -\frac{\Delta_{\mathbf{k}}}{\xi_{\mathbf{k}}}, \tag{1.19}$$

and the coefficients $u_{\mathbf{k}}$ and $v_{\mathbf{k}}$ results as follows

$$u_{\mathbf{k}}^2 = \frac{1}{2}(1+\frac{\xi_{\mathbf{k}}}{\epsilon_{\mathbf{k}}}), \tag{1.20}$$

$$v_{\mathbf{k}}^2 = \frac{1}{2}(1-\frac{\xi_{\mathbf{k}}}{\epsilon_{\mathbf{k}}}). \tag{1.21}$$

We take the matrix element $V_{\mathbf{k}\mathbf{k}'}$ as in Eq. (1.7), so the quantity $\Delta_{\mathbf{k}}$ actually is independent of the wave vector $\mathbf{k}$. From Eqs. (1.14), (1.17) and (1.20), the total energy of the superconducting ground state is given by

$$E_s = \sum_{\mathbf{k}} \left(\xi_{\mathbf{k}} - \frac{\xi_{\mathbf{k}}^2}{\epsilon_{\mathbf{k}}}\right) - \frac{\Delta^2}{V}. \tag{1.22}$$

The energy difference between the superconducting ground state and the normal state is

$$\begin{aligned} E_s - E_n &= E_s - \sum_{|\mathbf{k}|<k_F} 2\xi_{\mathbf{k}} \\ &= 2\sum_{|\mathbf{k}|<k_F} \left(\xi_{\mathbf{k}} - \frac{\xi_{\mathbf{k}}^2}{\epsilon_{\mathbf{k}}}\right) - \frac{\Delta^2}{V} \\ &\approx -\frac{1}{2}N(0)\Delta^2. \end{aligned} \tag{1.23}$$

In the last step, the weak-coupling-limit (i.e. $N(0)V \ll 1$) is applied. It shows that the energy of the superconducting ground state is lower than the energy of the normal state.

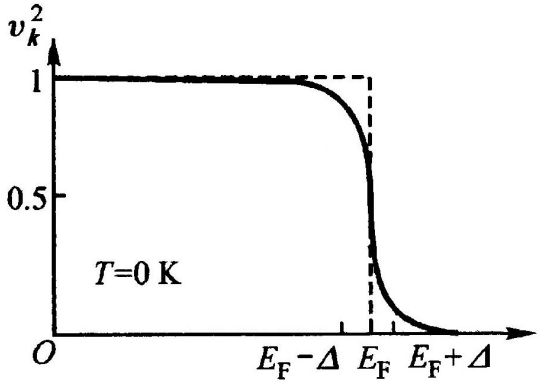

Fig. 1.11 Momentum distribution of the occupied single-particle states ($v_{\mathbf{k}}^2$) of the fermionic system at zero temperature.

The number of electrons of the ground state is

$$\begin{aligned} N &= \sum_{\mathbf{k}\sigma} \langle 0|C^{+}_{\mathbf{k}\sigma} C_{\mathbf{k}\sigma}|0\rangle \\ &= 2\sum_{\mathbf{k}} v^2_{\mathbf{k}}. \end{aligned} \tag{1.24}$$

In Fig. 1.11 we see that the Fermi surface is smeared out by the formation of the Cooper pairs. Further, the occupied probability of the Cooper pair ($\mathbf{k}\uparrow$, $-\mathbf{k}\downarrow$) is as follows,

$$\begin{aligned} \langle 0|C_{-\mathbf{k}\downarrow} C_{\mathbf{k}\uparrow}|0\rangle &= u_{\mathbf{k}} v_{\mathbf{k}} \\ &= \frac{1}{2}\frac{\Delta}{\sqrt{\xi^2_{\mathbf{k}} + \Delta}}. \end{aligned} \tag{1.25}$$

The formation of Cooper pairs in the case of the BCS approximation mainly occurs around the Fermi level ($\xi_{\mathbf{k}} = 0$).

The gap energy of a superconductor is the minimum energy required to add/remove one electron into/from the specimen. From Eq. (1.14), we can see that the contribution of the Cooper pair ($\mathbf{k}\uparrow$, $-\mathbf{k}\downarrow$) to the total energy of the superconductor is

$$\begin{aligned} w_{\mathbf{k}} &= 2\xi_{\mathbf{k}} v^2_{\mathbf{k}} - 2u_{\mathbf{k}} v_{\mathbf{k}} \sum_{\mathbf{k}'} V_{\mathbf{k}\mathbf{k}'} u_{\mathbf{k}'} v_{\mathbf{k}'} \\ &= \xi_{\mathbf{k}} - \epsilon_{\mathbf{k}}. \end{aligned} \tag{1.26}$$

When we add one electron into the state $\mathbf{q}$ at zero temperature, there must be no Cooper pair ($\mathbf{q}\uparrow$, $-\mathbf{q}\downarrow$). So, the energy of the new system is calculated as follows

$$\begin{aligned} W_{\mathbf{q}} &= W_{original} - w_{\mathbf{q}} + \xi_{\mathbf{q}} \\ &= W_{original} + \epsilon_{\mathbf{q}} \\ &= W_{original} + \sqrt{\xi^2_{\mathbf{q}} + \Delta^2}. \end{aligned} \tag{1.27}$$

From the above result, the gap energy of a superconductor at zero temperature is Δ.

1.2.2 Bogoliubov-de Gennes equations

As we have seen in the BCS theory, the probability amplitudes of the unoccupied and occupied pairing states $u_{\mathbf{k}}$ and $v_{\mathbf{k}}$ are position-independent, which leads to the difficulty of applying the BCS theory to inhomogeneous systems. The approach to superconductivity in inhomogeneous systems applied in this thesis is the BdG equations [35] which are a generalization of the Hartree-Fock equations for the case of superconductivity. From the BdG equations,

the quasiparticle energy spectrum and the spatially dependent gap energy at any temperature can be calculated in the presence or absence of a magnetic field. The BdG equations consists of two Schrödinger-like equations coupled by a pair potential (also called the order parameter). Together with the expressions (called the self-consistency conditions) of the Hartree-Fock potential and the order parameter, the BdG equations are solved self-consistently. In this subsection, we first obtain the BdG equations and the self-consistency conditions following de Gennes' method [35]. Second, the spin generalized BdG equations are introduced as well as the corresponding self-consistency conditions. Third, two numerical approaches to the BdG equations are given in detail for samples of different geometries (e.g., cylinders, hollow cylinders and films): solving the full BdG formalism and solving the BdG equations with Anderson's approximation.

1.2.2.1 Bogoliubov-de Gennes equations Here we start by rewriting the Hamiltonian of an interacting electron system in terms of field operators $\hat{\Psi}(\mathbf{r}\sigma)$,

$$\hat{H} = \hat{H}_0 + \hat{H}_1, \tag{1.28}$$

$$H_0 = \int \mathrm{d}\mathbf{r} \sum_{\alpha} \hat{\Psi}^{\dagger}(\mathbf{r}\alpha) H_e(\mathbf{r}) \hat{\Psi}(\mathbf{r}\alpha), \tag{1.29}$$

$$H_1 = -\frac{1}{2} V \int \mathrm{d}\mathbf{r} \sum_{\alpha\beta} \hat{\Psi}^{\dagger}(\mathbf{r}\alpha) \hat{\Psi}^{\dagger}(\mathbf{r}\beta) \hat{\Psi}(\mathbf{r}\beta) \hat{\Psi}(\mathbf{r}\alpha), \tag{1.30}$$

where

$$H_e(\mathbf{r}) = \frac{1}{2m_e} \big(-i\hbar\nabla - \frac{e\mathbf{A}}{c} \big)^2 + U_0(\mathbf{r}) - \mu_F, \tag{1.31}$$

with $\mathbf{A}$ the vector potential of the external magnetic field, and μ_F the chemical potential. There are several simplifications in the above expressions. In H_0, the effect of the magnetic field on the electron spins is neglected, and the external one-particle potential $U_0(\mathbf{r})$ is taken to be independent of the spin of the electron. The interaction ($V > 0$) between two electrons is also considered as spin-independent and of the form of a contact potential, i.e., in the delta function approximation. The field operators

$$\hat{\Psi}(\mathbf{r}\alpha) = \sum_{\mathbf{k}} w_{\mathbf{k}}(\mathbf{r}) C_{\mathbf{k}\alpha} \tag{1.32}$$

satisfy the anticommutation rules

$$[\hat{\Psi}(\mathbf{r}\alpha), \hat{\Psi}^{\dagger}(\mathbf{r}'\beta)]_+ = \delta_{\alpha\beta}\delta(\mathbf{r} - \mathbf{r}'), \tag{1.33}$$

$$[\hat{\Psi}(\mathbf{r}\alpha), \hat{\Psi}(\mathbf{r}'\beta)]_+ = 0, \tag{1.34}$$

with $\{w_{\mathbf{k}}(\mathbf{r})\}$ being a complete set of single-electron wave functions.

The interaction Hamiltonian H_1 in Eq. (1.30) comprises the product of four field operators is too complex in order to handle it directly. As a mean-field

approximation, we can replace $V\hat{\Psi}^\dagger\hat{\Psi}^\dagger\hat{\Psi}\hat{\Psi}$ by the sum of the terms including the product of two field operators and one average potential. As a result, we obtain an effective Hamiltonian given by

$$\begin{aligned}\hat{H}_{\rm eff} &= \int {\rm d}\mathbf{r}\Big\{\sum_\alpha \left[\hat{\Psi}^\dagger(\mathbf{r}\alpha)H_e(\mathbf{r})\hat{\Psi}(\mathbf{r}\alpha)+U(\mathbf{r})\hat{\Psi}^\dagger(\mathbf{r}\alpha)\hat{\Psi}(\mathbf{r}\alpha)\right] \\ &\quad +\Delta(\mathbf{r})\hat{\Psi}^\dagger(\mathbf{r}\uparrow)\hat{\Psi}^\dagger(\mathbf{r}\downarrow)+\Delta^*(\mathbf{r})\hat{\Psi}(\mathbf{r}\downarrow)\hat{\Psi}(\mathbf{r}\uparrow)\Big\}. \qquad (1.35)\end{aligned}$$

The physical meaning of the effective Hamiltonian is clear. Its first term stands for the kinetic energy of electrons, the second term with the Hartree-Fock potential $U(\mathbf{r})$ is the interaction energy, and the last two terms with the order parameter $\Delta(\mathbf{r})$ appear due to the formation of the Cooper pairs. The commutators $[\hat{H}_{\rm eff},\hat{\Psi}(\mathbf{r}\alpha)]$ are

$$[\hat{\Psi}(\mathbf{r}\uparrow),\hat{H}_{\rm eff}] = [H_e(\mathbf{r})+U(\mathbf{r})]\hat{\Psi}(\mathbf{r}\uparrow)+\Delta(\mathbf{r})\hat{\Psi}^+(\mathbf{r}\downarrow) \qquad (1.36)$$

$$[\hat{\Psi}(\mathbf{r}\downarrow),\hat{H}_{\rm eff}] = [H_e(\mathbf{r})+U(\mathbf{r})]\hat{\Psi}(\mathbf{r}\downarrow)-\Delta(\mathbf{r})\hat{\Psi}^+(\mathbf{r}\uparrow). \qquad (1.37)$$

Because the effective Hamiltonian has a quadratic form in the field operators, it can be diagonalized by performing the generalized Bogoliubov-Valatin transformation

$$\hat{\Psi}(\mathbf{r}\uparrow) = \sum_n \left[u_n(\mathbf{r})\gamma_{n\uparrow}-v_n^*(\mathbf{r})\gamma_{n\downarrow}^\dagger\right] \qquad (1.38)$$

$$\hat{\Psi}(\mathbf{r}\downarrow) = \sum_n \left[u_n(\mathbf{r})\gamma_{n\downarrow}+v_n^*(\mathbf{r})\gamma_{n\uparrow}^\dagger\right], \qquad (1.39)$$

where $u_n(\mathbf{r})$ and $v_n(\mathbf{r})$ (the coherence factors) are called the particle-like and hole-like wave functions, respectively. The new operators $\gamma_{n\sigma}$ and $\gamma_{n\sigma}^+$ still obey the anticommutation rules

$$[\gamma_{n\alpha},\gamma_{m\beta}^\dagger]_+ = \delta_{\alpha\beta}\delta_{nm}, \qquad (1.40)$$

$$[\gamma_{n\alpha},\gamma_{m\beta}]_+ = 0, \qquad (1.41)$$

The final effective Hamiltonian should have the diagonal form

$$\hat{H}_{\rm eff} = E_g+\sum_{n\alpha}\epsilon_n\gamma_{n\alpha}^\dagger\gamma_{n\alpha}, \qquad (1.42)$$

where E_g is the energy of the ground state, ϵ_n is the energy of quasiparticles, $\gamma_{n\alpha}^\dagger$ and $\gamma_{n\alpha}$ can be regarded as the creation and destruction operators of quasiparticles (bogolons), respectively. With the commutation relations Eqs. (1.41), we obtain the following commutators

$$[\hat{H}_{\rm eff},\gamma_{n\alpha}] = -\epsilon_n\gamma_{n\alpha}, \qquad (1.43)$$

$$[\hat{H}_{\rm eff},\gamma_{n\alpha}^\dagger] = \epsilon_n\gamma_{n\alpha}^\dagger. \qquad (1.44)$$

Now inserting the transformations of Eqs. (1.39) into Eqs. (1.37) and using the relations given in Eqs. (1.44), we compare the coefficients of operators $\gamma_{n\alpha}$ and $\gamma^{+}_{n\alpha}$, and obtain the BdG equations:

$$\begin{bmatrix} H_e(\mathbf{r}) + U(\mathbf{r}) & \Delta(\mathbf{r}) \\ \Delta^*(\mathbf{r}) & -H_e^*(\mathbf{r}) - U(\mathbf{r}) \end{bmatrix} \begin{bmatrix} u_n(\mathbf{r}) \\ v_n(\mathbf{r}) \end{bmatrix} = \epsilon_n \begin{bmatrix} u_n(\mathbf{r}) \\ v_n(\mathbf{r}) \end{bmatrix}. \tag{1.45}$$

From the BdG equations, it can be proved that the wave functions $u_n(\mathbf{r})$ and $v_n(\mathbf{r})$ obey the normalization condition

$$\int \mathrm{d}\mathbf{r}[u_n^*(\mathbf{r})u_m(\mathbf{r}) + v_n^*(\mathbf{r})v_m(\mathbf{r})] = \delta_{nm}. \tag{1.46}$$

1.2.2.2 Self-consistency conditions In order to solve the BdG equations (1.45), we determine the Hartree-Fock potential $U(\mathbf{r})$ and the order parameter $\Delta(\mathbf{r})$ by the requirement that the variation of the free energies calculated from the full Hamiltonian Eq. (1.28) and from the effective Hamiltonian Eq. (1.35) should be equal to zero [35, 55].

The free energy of the system is

$$F = \langle H_0 + H_1 \rangle - TS, \tag{1.47}$$

where the brackets $\langle\rangle$ stand for the ensemble average over the eigenvalues and eigenfunctions of the effective Hamiltonian at temperature T, and S is the entropy. According to the Wick theorem, the average $\langle\hat{\Psi}^\dagger\hat{\Psi}^\dagger\hat{\Psi}\hat{\Psi}\rangle$ in the above expression can be simplified

$$\langle\hat{\Psi}^\dagger(1)\hat{\Psi}^\dagger(2)\hat{\Psi}(3)\hat{\Psi}(4)\rangle = \langle\hat{\Psi}^\dagger(1)\hat{\Psi}^\dagger(2)\rangle\langle\hat{\Psi}(3)\hat{\Psi}(4)\rangle \tag{1.48}$$

$$- \langle\hat{\Psi}^\dagger(1)\hat{\Psi}(3)\rangle\langle\hat{\Psi}^\dagger(2)\hat{\Psi}(4)\rangle \tag{1.49}$$

$$+ \langle\hat{\Psi}^\dagger(1)\hat{\Psi}(4)\rangle\langle\hat{\Psi}^\dagger(2)\hat{\Psi}(3)\rangle. \tag{1.50}$$

The variation of the free energy can be written as

$$\delta F = \int \mathrm{d}\mathbf{r}\Big\{ \sum_\alpha \delta\langle\hat{\Psi}^\dagger(\mathbf{r}\alpha)H_e(\mathbf{r})\hat{\Psi}(\mathbf{r}\alpha)\rangle \tag{1.51}$$

$$- V\langle\hat{\Psi}^\dagger(\mathbf{r}\uparrow)\hat{\Psi}(\mathbf{r}\uparrow)\rangle\delta\langle\hat{\Psi}^\dagger(\mathbf{r}\downarrow)\hat{\Psi}(\mathbf{r}\downarrow)\rangle \tag{1.52}$$

$$- V\langle\hat{\Psi}^\dagger(\mathbf{r}\downarrow)\hat{\Psi}(\mathbf{r}\downarrow)\rangle\delta\langle\hat{\Psi}^\dagger(\mathbf{r}\uparrow)\hat{\Psi}(\mathbf{r}\uparrow)\rangle \tag{1.53}$$

$$- V\big[\langle\hat{\Psi}^\dagger(\mathbf{r}\uparrow)\hat{\Psi}^\dagger(\mathbf{r}\downarrow)\rangle\delta\langle\hat{\Psi}(\mathbf{r}\downarrow)\hat{\Psi}(\mathbf{r}\uparrow)\rangle \tag{1.54}$$

$$+ \langle\hat{\Psi}(\mathbf{r}\downarrow)\hat{\Psi}(\mathbf{r}\uparrow)\rangle\delta\langle\hat{\Psi}^\dagger(\mathbf{r}\uparrow)\hat{\Psi}^\dagger(\mathbf{r}\downarrow)\rangle\big]\Big\} - T\delta S = 0. \tag{1.55}$$

On the other hand, the variation of the free energy of the effective Hamiltonian is written as

$$\delta F_{\rm eff} = \int {\rm d}\mathbf{r}\Big\{ \sum_{\alpha} \delta\langle\hat{\Psi}^{\dagger}(\mathbf{r}\alpha)[H_e(\mathbf{r}) + U(\mathbf{r})]\hat{\Psi}(\mathbf{r}\alpha)\rangle + \left[\Delta(\mathbf{r})\delta\langle\hat{\Psi}^{\dagger}(\mathbf{r}\uparrow)\hat{\Psi}^{\dagger}(\mathbf{r}\downarrow)\rangle + \Delta^{*}(\mathbf{r})\delta\langle\hat{\Psi}(\mathbf{r}\downarrow)\hat{\Psi}(\mathbf{r}\uparrow)\rangle\right]\Big\} - T\delta S = 0. \tag{1.56}$$

By comparing Eqs. (1.55) and (1.56), we find that they are the same if the Hartree-Fock potential and the order parameter are taken as follows,

$$U(\mathbf{r}) = -V\langle\hat{\Psi}^{\dagger}(\mathbf{r}\uparrow)\hat{\Psi}(\mathbf{r}\uparrow)\rangle = -V\langle\hat{\Psi}^{\dagger}(\mathbf{r}\downarrow)\hat{\Psi}(\mathbf{r}\downarrow),\rangle \tag{1.57}$$

$$\Delta(\mathbf{r}) = -V\langle\hat{\Psi}(\mathbf{r}\downarrow)\hat{\Psi}(\mathbf{r}\uparrow)\rangle = V\langle\hat{\Psi}(\mathbf{r}\uparrow)\hat{\Psi}(\mathbf{r}\downarrow)\rangle. \tag{1.58}$$

Now we replace the field operators $\hat{\Psi}(\mathbf{r}\alpha)$ in the above expressions by the operators $\gamma_{n\alpha}$ and $\gamma^{*}_{n\alpha}$ of quasiparticles according to Eq. (1.39), and apply the following mean values rules

$$\begin{aligned} &\langle\gamma^{\dagger}_{n\alpha}\gamma_{m\beta}\rangle = \delta_{nm}\delta_{\alpha\beta}f_n, \\ &\langle\gamma_{n\alpha}\gamma_{m\beta}\rangle = 0, \end{aligned} \tag{1.59}$$

where f_n is the Fermi distribution function

$$f_n = \frac{1}{e^{\epsilon_n/(k_BT)}+1}. \tag{1.60}$$

The Hartree-Fock potential and the order parameter are rewritten as

$$U(\mathbf{r}) = -V\sum_{n}\Big[|u_n(\mathbf{r})|^2 f_n + |v_n(\mathbf{r})|^2(1-f_n)\Big] \tag{1.61}$$

$$\Delta(\mathbf{r}) = V\sum_{n} u_n(\mathbf{r})v^{*}_n(\mathbf{r})(1-2f_n). \tag{1.62}$$

It is of great importance to notice that the summations in Eqs. (1.61) and (1.62) are different. For the Hartree-Fock potential, all the electron states bellow or above the chemical potential (or, the Fermi level at zero temperature) should be taken into account because this potential stands for the contribution from all the electrons. But, for the order which indicates the contribution from the Cooper pairs (see Eq. (1.58)), the summation should be over only the states within the Debye window around the chemical potential, i.e., the energy of single electrons $|\xi_n| < \hbar\omega_D$ with

$$\xi_n = \int {\rm d}\mathbf{r}\Big\{[u^{*}_n(\mathbf{r})[H_e(\mathbf{r}) + U(\mathbf{r})]u_n(\mathbf{r}) + v^{*}_n(\mathbf{r})[H_e(\mathbf{r}) + U(\mathbf{r})]v_n(\mathbf{r})]\Big\}. \tag{1.63}$$

In the presence of a magnetic field, $H_e(\mathbf{r})|_{\mathbf{A}=0}$ is taken in the above expression.

Another quantity of great importance is the chemical potential μ_F, which is determined from the mean electron density n_e:

$$n_e = \frac{2}{\Omega_{\text{vol}}} \int \mathrm{d}\,\mathbf{r} \sum_n \left[|u_n(\mathbf{r})|^2 f_n + |v_n(\mathbf{r})|^2 (1 - f_n) \right] \tag{1.64}$$

with Ω_{vol} the volume of the specimen.

1.2.2.3 Gauge invariance The single-electron Hamiltonian H_e in the BdG equations contains the vector potential $\mathbf{A}$ which can be changed to $\mathbf{A}'$

$$\mathbf{A}' = \mathbf{A} + \nabla\chi(\mathbf{r}) \tag{1.65}$$

while the configuration of the external magnetic field $\mathbf{h}(\mathbf{r})$ keeps the same. It can be proven [35] that the eigenvalues ϵ_n of the BdG equations are gauge invariant, i.e., they are unchanged by the gauge transformation Eq. (1.65). Other quantities such as the wave functions $u_n(\mathbf{r})$ and $v_n(\mathbf{r})$, the order parameter $\Delta(\mathbf{r})$, are gauge covariant:

$$\begin{aligned} u_n(\mathbf{r})' &= u_n(\mathbf{r}) e^{\frac{ie}{\hbar c}\chi(\mathbf{r})}, \\ v_n(\mathbf{r})' &= v_n(\mathbf{r}) e^{-\frac{ie}{\hbar c}\chi(\mathbf{r})}, \end{aligned} \tag{1.66}$$

and

$$\Delta'(\mathbf{r}) = \Delta(\mathbf{r}) e^{\frac{i2e}{\hbar c}\chi(\mathbf{r})}. \tag{1.67}$$

There are two special choices of the gauge that give some convenient properties. One is called the London gauge. In this gauge one chooses the gauge function $\chi(\mathbf{r})$ as

$$\nabla^2\chi(\mathbf{r}) = -\nabla \cdot \mathbf{A} \qquad \text{in the sample} \tag{1.68}$$

$$\mathbf{n} \cdot \nabla\chi(\mathbf{r}) = 0 \qquad \text{at the surface,} \tag{1.69}$$

the new vector potential $\mathbf{A}'$ satisfy the following properties

$$\nabla \cdot \mathbf{A}' = 0 \qquad \text{in the sample} \tag{1.70}$$

$$\mathbf{n} \cdot \mathbf{A}' = 0 \qquad \text{at the surface,} \tag{1.71}$$

where $\mathbf{n}$ is a unit vector normal to the surface. In the other gauge, with vector potential $\mathbf{A}$ the order parameter is of the form

$$\Delta(\mathbf{r}) = |\Delta(\mathbf{r})| e^{i\varphi(\mathbf{r})}. \tag{1.72}$$

By choosing the gauge function

$$\chi(\mathbf{r}) = -\frac{\hbar c}{2e}\varphi(\mathbf{r}), \tag{1.73}$$

the new order parameter becomes

$$\Delta'(\mathbf{r}) = |\Delta(\mathbf{r})|. \tag{1.74}$$

1.2.2.4 Spin generalized BdG equations Now we consider the single-electron potential in the single-electron Hamiltonian H_e is spin dependent $U_0(\mathbf{r}, \alpha\beta)$. The full Hamiltonian is

$$\begin{aligned}\hat{H} = &\int \mathrm{d}\mathbf{r} \sum_{\alpha,\beta} \hat{\Psi}^\dagger(\mathbf{r}\alpha)\big\{[\frac{1}{2m}(-i\hbar\nabla - \frac{e}{c}\mathbf{A})^2 - E_F]\delta_{\alpha\beta} + U_0(\mathbf{r}, \alpha\beta)\big\}\hat{\Psi}(\mathbf{r}\beta) \\ &- \frac{1}{2}V \int \mathrm{d}\mathbf{r} \sum_{\alpha,\beta} \hat{\Psi}^\dagger(\mathbf{r}\alpha)\hat{\Psi}^\dagger(\mathbf{r}\beta)\hat{\Psi}(\mathbf{r}\beta)\hat{\Psi}(\mathbf{r}\alpha).\end{aligned} \tag{1.75}$$

On the other hand, the effective Hamiltonian is given as

$$\begin{aligned}\hat{H}_{\text{eff}} = &\int \mathrm{d}\mathbf{r} \sum_{\alpha\beta} \Big\{ \hat{\Psi}^\dagger(\mathbf{r}\alpha)\big[(\frac{1}{2m}(-i\hbar\nabla - \frac{e}{c}\mathbf{A})^2 - E_F)\delta_{\alpha\beta} + U_0(\mathbf{r}, \alpha\beta)\big]\hat{\Psi}(\mathbf{r}\beta)\big] \\ &+\Delta(\mathbf{r})\rho_{\alpha\beta}\hat{\Psi}^\dagger(\mathbf{r}\alpha)\hat{\Psi}^\dagger(\mathbf{r}\beta) + \Delta^*(\mathbf{r})\rho_{\alpha\beta}\hat{\Psi}(\mathbf{r}\alpha)\hat{\Psi}(\mathbf{r}\beta)\Big\},\end{aligned} \tag{1.76}$$

where

$$\rho = \begin{bmatrix} 0 & 1 \\ -1 & 0 \end{bmatrix}. \tag{1.77}$$

By introducing a generalized Bogoliubov transformation

$$\hat{\Psi}(\mathbf{r}\alpha) = \sum_N [u_{N\alpha}(\mathbf{r})\gamma_N + v^*_{N\alpha}(\mathbf{r})\gamma^\dagger_N] \tag{1.78}$$

with N indicating the translational and spin quantum numbers, we diagonalize the effective Hamiltonian. Similar with the deduction of the BdG equations, making use of the above transformation and the commutators ($[\hat{H}_{\text{eff}}, \gamma_N]$ and $[\hat{H}_{\text{eff}}, \hat{\Psi}(\mathbf{r}\alpha)]$), we obtain the spin generalized BdG equations

$$\begin{aligned}\epsilon u_{N\alpha}(\mathbf{r}) &= [\frac{1}{2m}(-i\hbar\nabla - \frac{e}{c}\mathbf{A})^2 - E_F]u_{N\alpha}(\mathbf{r}) + U_0(\mathbf{r}, \alpha\beta)u_{N\beta}(\mathbf{r}) \\ &\quad + \Delta(\mathbf{r})\rho_{\alpha\beta}v_{N\beta}(\mathbf{r}) \\ -\epsilon v_{N\alpha}(\mathbf{r}) &= [\frac{1}{2m}(i\hbar\nabla - \frac{e}{c}\mathbf{A})^2 - E_F]v_{N\alpha}(\mathbf{r}) + U^*_0(\mathbf{r}, \alpha\beta)v_{N\beta}(\mathbf{r}) \\ &\quad + \Delta^*(\mathbf{r})\rho_{\alpha\beta}u_{N\beta}(\mathbf{r}).\end{aligned} \tag{1.79}$$

The order parameter is given as

$$\begin{aligned}\Delta(\mathbf{r}) &= \frac{1}{2}V \sum_{\alpha\beta} \rho_{\alpha\beta}\langle\hat{\Psi}(\mathbf{r}\alpha)\hat{\Psi}(\mathbf{r}\beta)\rangle \\ &= V \sum_N [u_{N\downarrow}(\mathbf{r})v^*_{N\uparrow}(\mathbf{r})f_N + u_{N\uparrow}(\mathbf{r})v^*_{N\downarrow}(\mathbf{r})(1 - f_N)].\end{aligned} \tag{1.80}$$

The wave functions $u_{N\alpha}(\mathbf{r})$ and $v_{N\alpha}(\mathbf{r})$ satisfy the normalization condition:

$$\sum_{\alpha=1}^{2} \int \mathrm{d}\mathbf{r}[u^*_{M\alpha}u_{N\alpha} + v^*_{M\alpha}v_{N\alpha}] = \delta_{MN}. \tag{1.81}$$

1.2.3 Numerical approaches to BdG equations

There are several approaches to numerically solve the BdG equations, such as e.g., the finite-difference method or the finite-element method. The basic procedure of all these approaches splits into the following steps: (i) first, the BdG equations are converted into corresponding matrix equation; (ii) second, with an initial guess for the order parameter $\Delta(\mathbf{r})$ and an initial guess for the Hartree-Fock potential $U(\mathbf{r})$, the matrix equation is solved; (iii) third, the eigenenergies ϵ_n and eigenfunctions $u_n(\mathbf{r})$ and $v_n(\mathbf{r})$ are employed to calculate a new order parameter and a new Hartree-Fock field from the self-consistent conditions given by Eqs. (1.61) and (1.62); (iv) fourth, we continue to perform the previous three steps so that we reach the stable solutions iteratively for $\Delta(\mathbf{r})$, $U(\mathbf{r})$, quasiparticle wave functions $u_n(\mathbf{r})$ and $v_n(\mathbf{r})$, and quasiparticle energy spectrum ϵ_n.

In this subsection, we are focused on two numerical procedures to solve the BdG equations for nanofilms and nanowires (below we consider nanocylinders and hollow nanocylinders). We again convert the BdG equations (1.45) into a corresponding matrix equation. However, unlike the finite-difference and finite-element methods, we expand the BdG equations in terms of the single-electron wave functions $\phi_n(\mathbf{r})$ of nanofilms and nanocylinders, i.e., the eigenfunctions of the single-electron Hamiltonian $H_e(\mathbf{r})$ of the BdG equations:

$$H_e(\mathbf{r})\psi_n(\mathbf{r}) = \xi'_n\psi_n(\mathbf{r}). \tag{1.82}$$

We note that in the present thesis, we consider two kinds of materials, lead and aluminum, whose parameters used in the numerical calculations are listed in Table 1.1. Since we employ the BdG equations in the parabolic band approximation, an effective Fermi level has to be introduced to recover the correct period of the quantum-size oscillations in experiment as discussed in [26, 56].

Table 1.1 Material parameters used in the numerical calculations [26, 56].

Metal	$\hbar\omega_D$	$VN(0)$	Fermi level in bulk	Effective Fermi level
Al	32.31 meV	0.18	11.7 eV	0.90 eV
Pb	8.27 meV	0.39	9.47 eV	1.15 eV

1.2.3.1 Solving the full BdG equations To solve the BdG equations numerically, the particle-like and hole-like wave functions $u_n(\mathbf{r})$ and $v_n(\mathbf{r})$ are expanded in terms of the single-electron wave functions $\psi_n(\mathbf{r})$, because all the $\psi_n(\mathbf{r})$ form a complete basis of functions. The terms in the expansions of $u_n(\mathbf{r})$ and $v_n(\mathbf{r})$ include all single-electron wave functions with energies located in the Debye window around the chemical potential. With these expansions the BdG equations (1.45) are converted into a matrix equation for the expansion coefficients. The significant advantage of this method as compared to

the finite difference and finite-element schemes is a much smaller size of the numerical matrix. This is because the number of transverse (perpendicular) modes in nanowires and nanofilms is not large. Solving the matrix equation iteratively, often convergence is reached, and the original quantities (e.g., $u_n(\mathbf{r})$ and $v_n(\mathbf{r})$, $\Delta(\mathbf{r})$ and $U(\mathbf{r})$) are reconstructed.

At the beginning of the calculation, the bulk value of the order parameter is chosen as the initial guess for $\Delta(\mathbf{r})$. In the presence of a magnetic field, the initial input for the calculation can be the order parameter calculated from the previous value of the magnetic field. In this way, by increasing and decreasing the magnetic field, we can check the possible hysteretic behavior. The convergence of this algorithm is sensitive to temperature and the magnetic field. Far away from the superconductor-to-normal transition, the self-consistent calculation is well convergent and stable. But, in the vicinity of the superconductor-to-normal transition the convergence becomes rather capricious and depends strongly on the initial guess of the order parameter. Here it is of importance to correctly estimate the number of iterations needed to reach the desired accuracy.

1.2.3.2 Anderson's approximation Anderson's approximation [57] to the BdG equations is of great importance, because the physics behind the numerical results can be well understood from such a semi-analytical solution to the BdG equations. This approximation assumes that the particle-like $u_n(\mathbf{r})$ and hole-like $v_n(\mathbf{r})$ wave functions are proportional to the corresponding single-electron wave function, it takes only the time-reversal pairing into account. In the cases of nanofilms and nanowires, Anderson's approximation gives very accurate solutions, since the conduction band splits up into a series of subbands, and the distance between subbands significantly suppresses the non-time-reveral pairing. This is justified for ultrathin nanofilms and narrow nanowires. Indeed, for sufficiently small confined dimensions, the energy spacing between the neighboring subbands is large enough, and it supplies almost the exact result. Based on the Anderson approximation, the BdG equations are reduced to a BCS-like self-consistent equation for a set of the subband-dependent energy gaps. Solving this formalism is much less time consuming.

In the presence of the external magnetic field, the single-electron Hamiltonian $H_e \neq H_e^*$, i.e., the time-reversal symmetry is broken and use of Anderson's recipe becomes questionable. However, there are plausible exceptions like the set-up of a magnetic field parallel to the cylindrical nanowire. Here, when the term proportional to $\mathbf{A}^2$ in H_e is neglected (which is a very good approximation for nanowires), the eigenfunctions of H_e and H_e^* remain the same (although their eigenvalues are different). In this case, the Anderson approximation still yields very good results with corrections less than a few percents (see e.g., Ref. [23]).

1.3 NANOFILMS AND NANOWIRES

High-quality metallic nanostructures are available due to recent advances in nanofabrication technologies. In particular, Sn and Al nanowires (both made of strongly coupled grains [9–11] and single-crystalline [8, 16, 58]) with diameters down to $8 - 10$ nm and single-crystalline superconducting Pb and In nanofilms [2–6, 13, 19, 59–61] with thicknesses down to a few monolayers (ML) have been fabricated. Their superconducting properties have been studied experimentally through several techniques. In this section, we will describe two major nanofabrication technologies and some observation techniques used in experiments to explore superconductivity in nanostructures.

1.3.1 Nanofabrication technologies

In principle, nanofabrication technologies fall into two general classes: the bottom-up approaches and the top-down approaches. The bottom-up approaches, such as molecular beam epitaxy (MBE), metal-organic chemical vapor deposition, self-assembly and nanofabrication by scanning probe techniques, manipulate and combine the atoms or molecules to form larger nanoscale structures, while the top-down approaches, such as lift-off lithography, microimprint lithography, electron-beam lithography and X-ray lithography, are mostly based on microfabrication techniques. Here we briefly introduce two common methods used in producing high-quality nanofilms and nanowires: MBE and Lift-off lithography.

1.3.1.1 Molecular beam epitaxy Molecular beam epitaxy, invented by J. R. Arthur and Alfred Y. Cho [62] in 1960s, is often used to deposit single crystalline nanofilms [13, 17, 21, 63] and nanowires [64].

In molecular beam epitaxy, elements in extreme-pure form are heated in effusion cells (see Fig. 1.12) until they are converted from the solid state to vapor slowly. The gaseous atoms or molecules are sputtered out of the cells and condensed on the substrates in single crystalline form with a slow deposition rate (e.g., 0.2 ML/min in fabricating Pb nanofilms [21]). The slow deposition rate is the most important characteristic, which allows the nanofilms or nanowires to grow epitaxially. And due to the slow deposition rate, molecular beam epitaxy has to be placed in high vacuum or ultra-high vacuum (10^{-8} Pa) to reduce the level of impurity in the sample. In addition, the ultra-high vacuum condition can be maintained by a cooling system of cryopumps and cryopanels cooling with liquid nitrogen at temperature about 77 Kelvin.

During the process, the growth of the single-crystalline sample is often monitored by the reflection high energy electron diffraction (RHEED) which only gathers information of surface layers of the sample by analyzing the diffraction pattern generated by shooting high energy electron beam at the sample

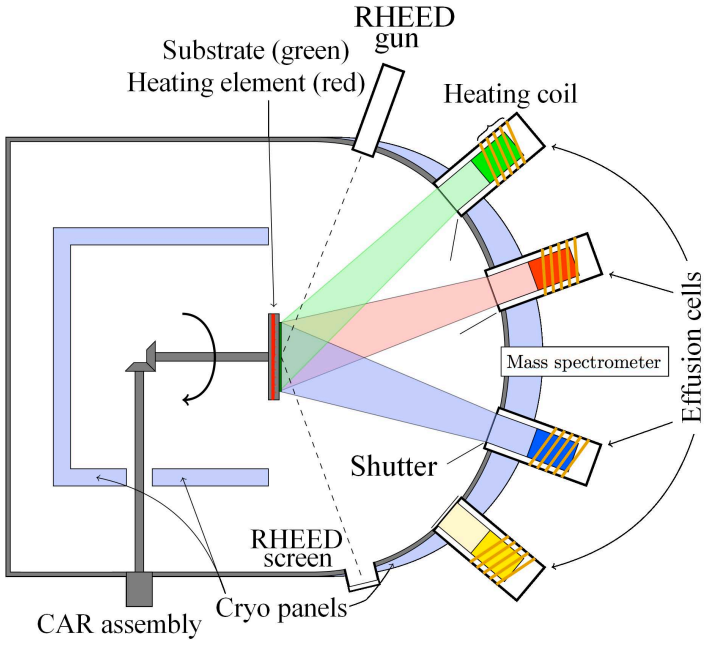

Fig. 1.12 Sketch of the molecular beam epitaxy system.

with a glancing angle. In most cases, the substrate needs to be heated to several hundred degrees Celsius and rotated at a certain speed to eliminate the possible imperfection in the sample. The thickness of the sample is controlled by a computer, which can adjust shutters in front of each effusion cell. Such high precise control has led to the fabrication of one-atomic-layer metal films [13].

1.3.1.2 Lift-off lithography The powerful lift-off lithography, combined with other technologies such as electron-beam lithography, is able to create structures with size from centimeter scale to nanoscale, including high-quality nanofilms and nanowires.

The process of lift-off lithography is shown in Fig. 1.13. The pattern of the target specimen is first etched in a sacrificial stencil layer deposited on a well prepared substrate. After that the target material is deposited over the whole sacrificial stencil layer and the substrate. So, both the etched region on the substrate and the surface of the sacrificial stencil layer are covered by the target material. Then, the sacrificial layer is washed away and the redundant target material covering it is lifted-off. In the end, the target structure is left on the surface of the substrate.

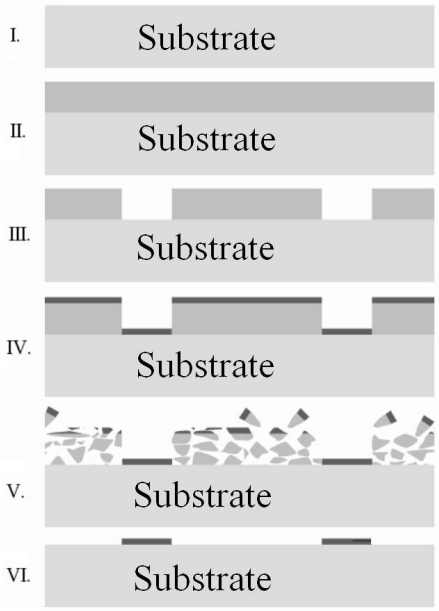

Fig. 1.13 Sketch of the lift-off lithography: I. preparation of the substrate, II. deposition of the sacrificial stencil layer, III. patterning the sacrificial layer, creating an inverse pattern, IV. deposition of the target sample, V. remove the sacrificial layer, VI. final sample.

After the fabrication of nanostructures, the condition of the surface can be examined by RHEED, scanning tunneling microscope (see Subsection 1.3.2.1), or transmission electron microscope (TEM) in the bright field imaging mode (in such mode, the contrast formation is formed by the absorption of electrons in the sample, as well as the interference of electron waves that penetrating through the sample and the incoming electron waves). The information of the specimen structure can be extracted from diffraction images taken by the TEM. Fig. 1.14 from Ref. [16] shows high-resolution TEM images of a metallic Sn nanowire covered completely by a well graphitized carbon layer. Typically around 10-12 carbon walls surround the tin nanowire.

1.3.2 Experimental characterization of nanoscale superconductivity

Resistivity measurement and scanning tunneling spectroscopy are commonly used to determine the critical temperature and the critical magnetic field of superconducting nanowires and nanofilms. In a resistivity measurement, the temperature-dependent or magnetic-field-dependent resistance is measured, while in scanning tunneling spectroscopy (STS) a scanning tunneling micro-

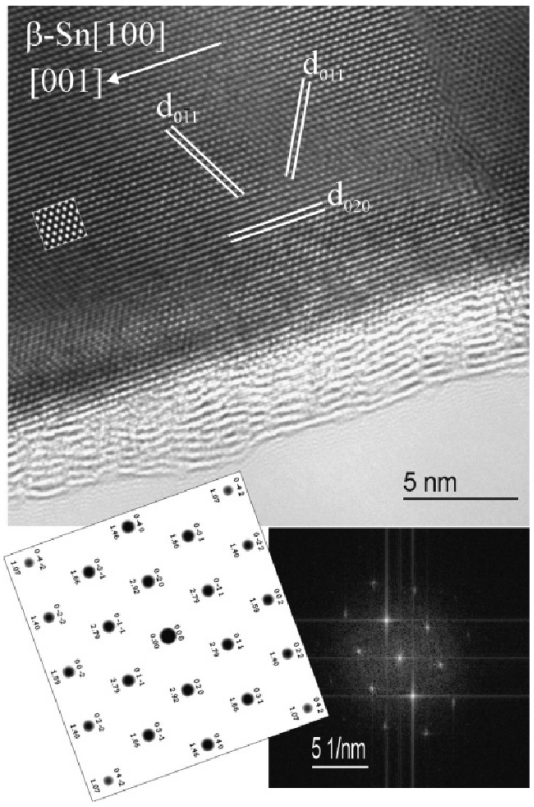

Fig. 1.14 High-resolution TEM image showing the high degree of crystallinity of both the multi-walled carbon nanotubes and the metallic Sn nanowires. The preferential direction of growth is the ⟨001⟩ direction pointing more or less along the nanowire axis. The insets are the corresponding selected-area electron diffraction patterns, experimental (right) and simulated (left) (an inset of the plane (001) of β-Sn is presented). [16]

scope (STM) is used to measure the density of states (DOS) in the sample. In this subsection, a short introduction to STM and STS is given.

1.3.2.1 Scanning tunneling microscope and spectroscopy Scanning tunneling microscope, invented by Gerd Binnig and Heinrich Rohrer in 1981, is widely used to obtain atomic-scale images of metal surfaces and the local density of states (LDOS) of electrons (for superconductors, the LDOS of quasiparticles is measured). The physical foundation of the STM is the quantum tunneling of electrons between the tip and the sample.

An illustration of the STM setup is shown in Fig. 1.15. A tip positioned above the sample can scan horizontally in x and y directions. When a negative voltage is applied on the sample and the distance between the tip and sample is short enough, electrons from occupied states at the surface of the sample tunnel into the unoccupied states of the tip. The strength of the tunneling current I_T strongly depends on the distance between the tip and the sample, as well as on the applied bias U_T and the LDOS of the sample and the tip.

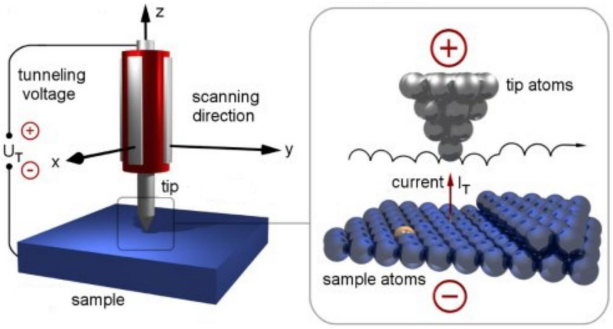

Fig. 1.15 A schematic STM system: with applying a negative voltage on the sample electrons tunnel from occupied states at the surface of the sample into unoccupied states of the tip. The topography of the sample is measured by keeping the tunneling current constant while scanning the tip over the surface. During the operation, the height of the tip which follows a contour of constant local density of states represents the topography of the specimen.

The STM can work in two modes, called constant current mode and constant height mode. In the first mode, the topography of the sample is mapped into image by recording the motion of the height of the tip when scanning the sample with constant tunneling current and applied bias. In such case the tip follows a contour of constant LDOS of the sample. Fig. 1.16 from Ref. [19] shows the topography of a 2 ML Pb nanofilm on Si substrate with an accuracy higher than 1 nm. The yellow color indicates the Pb atoms with the maximum height, while the black shows the surface of the Si substrate.

In the constant height mode, the scanning tunneling spectrum, which is the relation between the DOS and the energy of tunneling electrons (set by the bias voltage U_T), is obtained. The electron tunneling current is measured as a function of the bias voltage with fixing the height of the scanning tip. The relation among the tunneling current, the bias voltage and the LDOS of the sample is described by the following equation [6]:

$$\frac{dI}{dV} = -G_{nn} \int_{-\infty}^{\infty} \frac{\rho_s(E)}{N(0)} f'(E - eU_T) dE, \tag{1.83}$$

where G_{nn} is the Ohmic conductance between the tip and the sample, $f'(E)$ is the derivative of the Fermi function, and the ratio between the supercon-

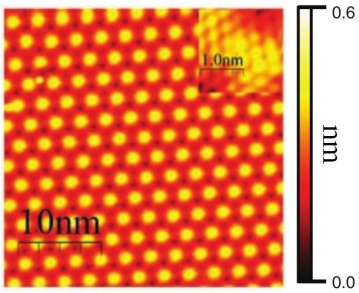

Fig. 1.16 A STM image of a 2 ML Pb nanofilm on Si substrate. The thickness of one monolayer for Pb nanofilms is 0.286 nm. [19]

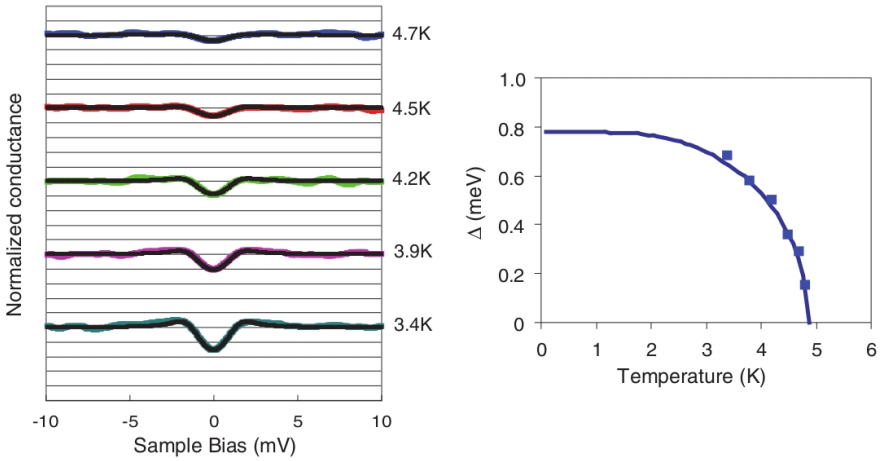

Fig. 1.17 (Left panel) Normalized conductance spectra (nonblack colors) taken by STM were fitted using the BCS-like formula for the tunneling conductance (black). (Right panel) The energy gaps (Δ) at several temperatures were obtained from the left panel and plotted as blue squares. The blue curve is a fitting of these energy gap data using a BCS-like gap equation to obtain a Tc of about 4.9 K for 2 ML Pb naofilm in Fig. 1.16. [19]

ducting and the normal DOS of a homogeneous bulk sample is given by

$$\frac{\rho_s(E)}{N(0)} = \theta(E-\Delta)\frac{|E|}{\sqrt{E^2-\Delta^2}} \tag{1.84}$$

with $\theta(x)$ the unit step function and Δ the energy gap. To be more realistic, the broadening introduced by the voltage modulation is taken into account. From Eq. (1.83), it is found that the dI/dV corresponds to the electron

density of states at the local position of the tip. For example, in the left panel of Fig. 1.17, normalized conductance spectra, at various temperatures for Pb nanofilms shown in Fig. 1.16, are fitted with the BCS-like DOS in Eq. (1.84) to obtain a temperature-dependent energy gap $\Delta(T)$. The right panel shows the energy gap calculated with BCS theory (the blue curve) and the fitted results (the blue squares).

2

Effect of spatial Hartree-Fock potential of the BdG equations

2.1 INTRODUCTION

Quantum confinement breaks the translational symmetry and the superconducting order parameter becomes position dependent. The well-known BCS ansatz for the ground state wave function is not applicable in this case, and the BdG equations are a relevant tool to investigate equilibrium superconducting properties. Recent numerical studies of the BdG equations for nanofilms [26] and nanowires [24, 25, 65, 66] show that the transverse quantum confinement has a substantial impact on the superconducting properties. However, the BdG equations investigated in [24–26, 65, 66], were solved without the Hartree-Fock (HF) potential. The reason is that in bulk, the superconducting properties are not sensitive to the HF term in the BdG equations [67] and, so, the common expectation is that a similar conclusion holds for the broken translational symmetry. However, there is no detailed investigations on this subject and, so, such a study is needed.

In the bulk BdG equations, the HF potential is not spatially dependent producing the same contribution to all single-electron energies, with no dependence on the relevant quantum numbers. Hence, the Fermi level (the chemical potential) acquires the same contribution, as well, and the single-electron energies measured from the Fermi level are not changed. The BdG equations are derived within the grand canonical formalism and, the electron energies appearing in the basic expressions absorb the chemical potential. As a result, the superconducting properties are insensitive to the HF potential. The situation is different in the presence of quantum confinement. The translational symmetry is now broken, the HF mean field is position dependent, and, its contribution to the single-electron energies depends on the

relevant quantum numbers. Furthermore, the single-electron wave functions themselves are influenced by the presence of the HF field, i.e., an additional spatially-dependent potential. Therefore, one can expect that the HF term in the BdG equations can change the superconducting properties in the presence of quantum confinement. It is of importance to clarify to what extent this will be true. In particular, this concerns the thickness-dependent oscillations (i.e., quantum-size oscillations) of the superconducting properties typical of high-quality nanofilms and nanowires [2–4, 7, 24–26].

By numerically solving the BdG equations for a superconducting clean nanocylinder, we investigate in this chapter how the HF term influences the superconducting solution in the presence of quantum confinement. The chapter is organized as follows. In Sec. 2.2 we outline the formalism of the BdG equations for a nanocylinder. In addition, Anderson's approximate semi-analytical solution to these equations is constructed here under the assumption that the single-electron wave functions do not change in the presence of the HF interaction. This makes it possible to check the effect of the HF field on the relevant wave functions. In Sec. 2.3 we investigate and discuss numerical results of the BdG equations with and without the HF term and compare them with Anderson's approximation.

2.2 THEORETICAL FORMALISM

In nanocylinders, it is convenient to use cylindrical coordinates ρ, φ and z. In this case the order parameter and HF potential in the BdG Eqs. (1.45) and the self-consistent conditions depend only on the transverse coordinate, i.e., $\Delta(\rho)$ and $\Phi_{HF}(\rho)$, and quasiparticle wave functions $u_\nu(\mathbf{r})$ and $v_\nu(\mathbf{r})$ are represented in the form ($\nu = \{j, m, k\}$)

$$\begin{pmatrix} u_\nu(\mathbf{r}) \\ v_\nu(\mathbf{r}) \end{pmatrix} = \frac{e^{\imath m\varphi}}{\sqrt{2\pi}} \frac{e^{\imath kz}}{\sqrt{L}} \begin{pmatrix} u_{jmk}(\rho) \\ v_{jmk}(\rho) \end{pmatrix}, \tag{2.1}$$

with j controlling the number of nodes in the transverse direction, m the azimuthal quantum number, and k the wave vector of the quasi-free electron motion along the nanocylinder. Inserting Eq. (2.1) into Eqs. (1.45), we recast the BdG equations as

$$\left[E_{jmk} - \mathcal{L}_\rho - \Phi_{HF}(\rho)\right] u_{jmk}(\rho) = \Delta(\rho) v_{jmk}(\rho), \tag{2.2}$$

$$\left[E_{jmk} + \mathcal{L}_\rho + \Phi_{HF}(\rho)\right] v_{jmk}(\rho) = \Delta(\rho) u_{jmk}(\rho), \tag{2.3}$$

where $\Delta(\rho)$ is real, and

$$\mathcal{L}_\rho = -\frac{\hbar^2}{2m_e}\Big(\frac{\partial^2}{\partial\rho^2} + \frac{1}{\rho}\frac{\partial}{\partial\rho} - \frac{m^2}{\rho^2} - k^2\Big) - E_F. \tag{2.4}$$

The self-consistency relations Eqs. (1.61) and (1.62) can be rewritten as,

$$\Delta(\rho) = \tfrac{g}{2\pi L}\textstyle\sum_{jmk\in C} u_{jmk}(\rho)v_{jmk}(\rho)\big[1-2f_{jmk}\big], \tag{2.5}$$

$$\Phi_{HF}(\rho) = -\tfrac{g}{2\pi L}\textstyle\sum_{jmk}\Big[u^2_{jmk}(\rho)f_{jmk} + v^2_{jmk}(\rho)\big(1-f_{jmk}\big)\Big], \tag{2.6}$$

with $u_{jmk}(\rho)$ and $v_{jmk}(\rho)$ real. To numerically solve Eqs. (2.2) and (2.3), we expand the transverse particle-like and hole-like wave functions as

$$\left(\begin{array}{c} u_{jmk}(\rho) \\ v_{jmk}(\rho) \end{array}\right) = \sum_J \left(\begin{array}{c} u_{jmk,J} \\ v_{jmk,J} \end{array}\right) \vartheta_{Jm}(\rho), \tag{2.7}$$

with

$$\vartheta_{Jm}(\rho) = \frac{\sqrt{2}}{R\mathcal{J}_{m+1}(\alpha_{Jm})}\mathcal{J}_m(\alpha_{Jm}\frac{\rho}{R}), \tag{2.8}$$

where $\mathcal{J}_m(x)$ is the Bessel function of the first kind of the m-order, and α_{Jm} is the Jth zero of this function. This allows one to convert Eqs. (2.2) and (2.3) into a matrix form. Then, a numerical solution can be obtained by diagonalizing the corresponding matrix, and self-consistency is reached by iterating Eqs. (2.5) and (2.6). One should keep in mind the normalizition of the quasiparticle wave functions Eq. (1.46), so,

$$\int_0^R \mathrm{d}\rho\,\rho[u^2_{jmk}(\rho) + v^2_{jmk}(\rho)] = 1. \tag{2.9}$$

As seen, the vector $(u_{jmk,J}; v_{jmk,J})^{\mathrm{T}}$ $(J = 0, 1, \ldots)$ is normalized.

In addition to the above procedure, below we use the Anderson approximate solution. Within this approximation, instead of the expansion given by Eq. (2.7), it is assumed that

$$u_{jmk}(\rho) = \mathcal{U}_{jmk}\,\vartheta_{jm}(\rho),\ v_{jmk}(\rho) = \mathcal{V}_{jmk}\,\vartheta_{jm}(\rho). \tag{2.10}$$

Equation (2.10) means that we seek a minimum of the BdG thermodynamic functional in the subspace of $u_{jmk}(\rho)$ and $v_{jmk}(\rho)$ proportional to the eigenfunctions of $\mathcal{L}_\rho$. Notice that it is possible to deal with Anderson's recipe, invoking the eigenfunctions of $\mathcal{L}_\rho + \Phi_{HF}(\rho)$. However, below we are interested in Eq. (2.10) because it helps to clarify how a change in the single-electron wave functions due to the HF potential, can contribute to the problem of interest. To be accurate, the Anderson approximation should be based on the true single-electron wave functions. We recently found that in this case the error in Anderson's solution for $D \lesssim 2-3\,\mathrm{nm}$ is less than one-two percents [68]. Hence, comparing the results of numerically solving Eqs. (2.2) and (2.3) with the data based on Eq. (2.10), we can reach unambiguous conclusions about the role of the changes in the single-electron wave functions due to the HF

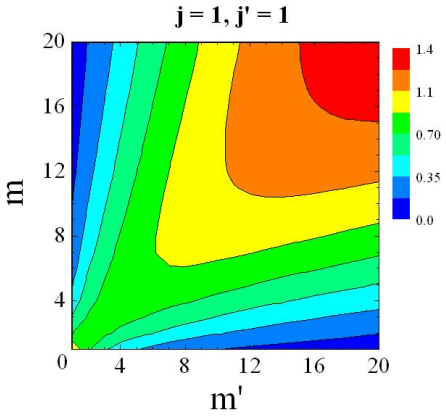

Fig. 2.1 Contour plot of the interaction-matrix elements $g_{j'm',jm}$ in units of $-\frac{g}{2\pi L}$ for the case with radius $R = 2\,\mathrm{nm}$ and $j = j' = 1$.

interaction. As follows from Eq. (2.10) [see, for instance, [68]], the Anderson approximation results in the BCS-like self-consistent equation

$$\Delta_{j'm'} = -\frac{1}{2}\sum_{jmk\in C}\frac{g_{j'm',jm}\ \Delta_{jm}}{\sqrt{\xi_{jmk}^2+\Delta_{jm}^2}}\big[1-2f_{jmk}\big], \tag{2.11}$$

with

$$\Delta_{jm} = \int_0^R \mathrm{d}\rho\,\rho\,\vartheta_{jm}^2(\rho)\ \Delta(\rho) \tag{2.12}$$

and the interaction-matrix element given by

$$g_{j'm',jm} = -\frac{g}{2\pi L}\int_0^R \mathrm{d}\rho\,\rho\ \vartheta_{j'm'}^2(\rho)\ \vartheta_{jm}^2(\rho). \tag{2.13}$$

The contour plot Fig. 2.1 shows $g_{j'm',jm}$ in units of $-\frac{g}{2\pi L}$ for the case with radius $R = 2\mathrm{nm}$ and $j = j' = 1$ as a function of m and m'. We can see that the elements with the same m' and m have the maximum absolute value, which means the every Josephson coupling from other subbands gives less contribution than the inner coupling of a subband.

For the single-electron energy appearing in Eq. (2.11) we have

$$\xi_{jmk} = \frac{\hbar^2}{2m_e}\Big[\frac{\alpha_{jm}^2}{R^2}+k^2\Big] + \Phi_{jm} - E_F, \tag{2.14}$$

where

$$\Phi_{jm} = \int_0^R \mathrm{d}\rho\, \rho\, \vartheta_{jm}^2(\rho)\, \Phi_{HF}(\rho). \tag{2.15}$$

Inserting the self-consistant condition of the HF potential Eq. (1.61) into Eq. (2.15), one obtains

$$\Phi_{j'm'} = \frac{1}{2} \sum_{jmk} g_{j'm',jm} \Big[1 - \frac{\xi_{jmk}(1-2f_{jmk})}{\sqrt{\xi_{jmk}^2 + \Delta_{jm}^2}}\Big]. \tag{2.16}$$

We should not forget about E_F appearing in the single-electron energy given by Eq. (2.14). It is fixed through the mean electron density:

$$\begin{aligned} n_e &= \frac{2}{\pi R^2 L} \sum_{\nu} [|u_\nu(\mathbf{r})|^2 f(E_\nu) + |v_\nu(\mathbf{r})|^2 (1 - f(E_\nu))] \\ &= \frac{1}{\pi R^2 L} \sum_{jmk} \Big[1 - \frac{\xi_{jmk}(1-2f_{jmk})}{\sqrt{\xi_{jmk}^2 + \Delta_{jm}^2}}\Big], \end{aligned} \tag{2.17}$$

where $f(E)$ is the Fermi distribution function.

Thus, in the Anderson approximation introduced by Eq. (2.10), one needs to solve Eqs. (2.11) and (2.16), keeping Eq. (2.17). As already mentioned above, comparing a numerical solution of Eqs. (2.2) and (2.3) with the solution based on Anderson's recipe, we can check the effect of the HF interaction on the single-electron wave functions.

2.3 NUMERICAL RESULTS

In this section we investigate and discuss numerical self-consistent solutions of Eqs. (2.2) and (2.3) with the HF potential (the full version) and without it (the truncated version, by setting $\Phi_{HF}(\rho) = 0$ in the relevant expressions). Results are also compared with a solution of Eqs. (2.11) and (2.16). All the calculations are performed with the parameters typical for aluminum [35, 67]: $\hbar\omega_D = 32.31$ meV; $gN(0) = 0.18$, with $N(0) = m_e k_F/(2\pi^2\hbar^2)$ the bulk density of single-electron states at the Fermi level and k_F the bulk Fermi wavevector. For these parameters the bulk BCS coherence length $\xi_0 = 1.6\ \mu$m is significantly larger than the nanocylinder diameter. However, contrary to the ordinary Ginzburg-Landau picture, the superconducting order parameter now exhibits significant spatial variations in the transverse direction due to the broken translational symmetry. The length of the nanocylinder is taken as $L = 1\ \mu\mathrm{m} \gg \lambda_F = 2\pi/k_F$. This is an optimal choice, upholding, on one side, the use of periodic boundary conditions in the z direction and, on the other side, it results in a reasonable calculational time. As opposed to the truncated BdG equations, their full version requires much more time for

convergence of the numerical procedure, and this time increases proportionally with L^2. Numerically solving the Anderson equations (2.11) and (2.16) is less time-consuming and, so, we take $L = 5\,\mu$m in this case.

In Fig. 2.2(a) the spatially averaged order parameter

$$\bar{\Delta} = \frac{2}{R^2} \int_0^R \mathrm{d}\rho\, \rho \Delta(\rho),$$

calculated from Eqs. (2.2) and (2.3) where $\Delta(\rho)$ is the total order parameter given in Eq. (2.5), is plotted in units of the bulk order parameter ($\Delta_{\mathrm{bulk}} = 0.25\,\mathrm{meV}$) versus the nanocylinder diameter with and without the HF mean field. In Fig. 2.2(b) the corresponding critical temperature T_c (in units of the bulk one) is given. As seen, both data-sets exhibit pronounced size-dependent oscillations, typical of high-quality superconducting nanofilms and nanowires with uniform thickness [2–4, 7, 24–26]. Such oscillations result from single-electron subbands forming due to the transverse quantization of the electron motion. With an increase in the nanowire diameter, the subbands shift down in energy. Each time when a new subband comes into the Debye window around the Fermi level, the number of single-electron states contributing to the superconducting order parameter increases, and a size-dependent superconducting resonance develops. As follows from Fig. 2.2, the quantum-size oscillations corresponding to the full version of the BdG equations are somewhat shifted up. The mean distance between neighboring superconducting resonances is controlled by the bulk Fermi wavelength λ_F and, so, the shift magnitude is roughly proportional to λ_F. For typical metallic parameters this magnitude is about the unit-cell dimensions. However, for low-carrier-density materials, e.g., superconducting semiconductors (see, for instance, [69–72] and recent papers on boron-doped diamond [73, 74] and boron-doped silicon [75]), such a shift can approach the scale of few nanometers. The difference between the two sets of data in Fig. 2.2 is most significant for those diameters, where a size-dependent superconducting resonance in the case without the HF interaction is already present while in the full version such a resonance only starts to develop. The difference is not so significant but still survive when the resonance comes into its decay stage. When the resonance is fully decayed (the off-resonant regime), the HF corrections are practically negligible, and we arrive at the situation similar to bulk. Notice that small differences between the numerical results of the full and truncated BdG equations in the off-resonant regime (due to beating patterns of the corresponding curves), are because of the chosen nanowire length. Indeed, as follows from calculations for several selected off-resonant diameters, such beating patterns disappear when L increases up to $20 - 30\,\mu$m, and the results with and without the HF interaction approach each other.

Notice that maxima of $T_c/T_{c,\mathrm{bulk}}$ in Fig. 2.2(b) are generally higher than those of $\bar{\Delta}/\bar{\Delta}_{\mathrm{bulk}}$ in Fig. 2.2(a). This is due to formation of new Andreev-type states induced by the transverse quantum confinement. The quasiparticles

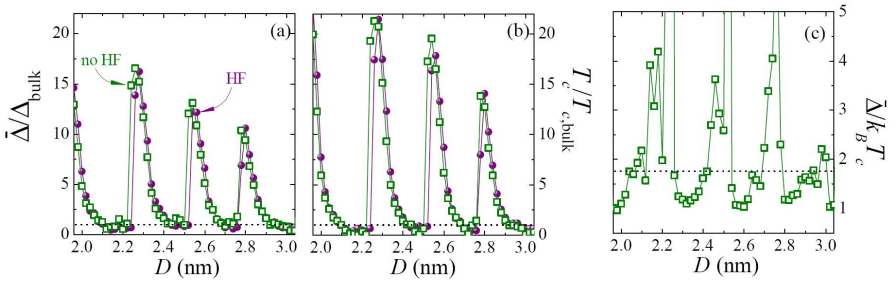

Fig. 2.2 (a) The spatially averaged superconducting order parameter $\bar{\Delta}/\Delta_{\rm bulk}$, (b) critical temperature $T_c/T_{c,\rm bulk}$ and (c) $\bar{\Delta}/(k_BT_c)$ versus the nanowires diameter D as calculated from the BdG equations (2.2) and (2.3) at zero temperature. In panel (c) only the results without the HF potential are shown. The dotted horizontal lines in panels (a) and (b) correspond to one, while in panel (c) it stands for the bulk value 1.763 of the ratio $\bar{\Delta}/(k_BT_c)$.

in such states avoid local maximum regions of the spatial order parameter, i.e., in some sense the order parameter seems to be the potential barrier for quasiparticles, so the corresponding subband energy gap drops significatly especially at the resonant points of the order parameter (see details in [22]). Thus, a decrease of $\bar{\Delta}/(k_BT_c)$ below the bulk value 1.763 at the resonant points occurs (see Fig. 2.2(c) at about $D = 2.3\,\text{nm}$). As seen from Fig. 2.2, inclusion of the HF interaction can slightly reduce the resonant enhancements, with practically no effect on the ratio $\bar{\Delta}/(k_BT_c)$.

In Fig. 2.3 we present different quantities calculated with the full and truncated versions of Eqs. (2.2) and (2.3) for two diameters: the upper panel, for $D = 2.24\,\text{nm}$; and the lower panel, for $D = 2.6\,\text{nm}$. The upper panel represents the situation when a superconducting resonance is developed for the truncated version but is not yet present for the full version of the BdG equations. In Fig. 2.3(a) the superconducting order parameter $\Delta(\rho)$ calculated with (HF) and without the HF interaction (no HF, the inset), is plotted versus the transverse coordinate ρ/R for $T = 0$. The spatial distribution of the pair condensate is very different for these two cases: the data without the HF interaction are larger by an order of magnitude, and even the profile of $\Delta(\rho)$ is different. In Fig. (2.3)(b) the local electron density, i.e.,

$$n_e(\rho) = \frac{1}{\pi L}\sum_{jmk}\Big[u^2_{jmk}(\rho)f_{jmk} + v^2_{jmk}(\rho)\big(1 - f_{jmk}\big)\Big], \tag{2.18}$$

is shown for the same diameter. As can be expected, now the difference between the two data-sets is not so significant (we keep to the same value of the mean electron density n_e). Due to the attractive character of the effective electron-electron interaction, the HF potential forces electrons to go closer to the nanocylinder center. However, the confining interaction has the major

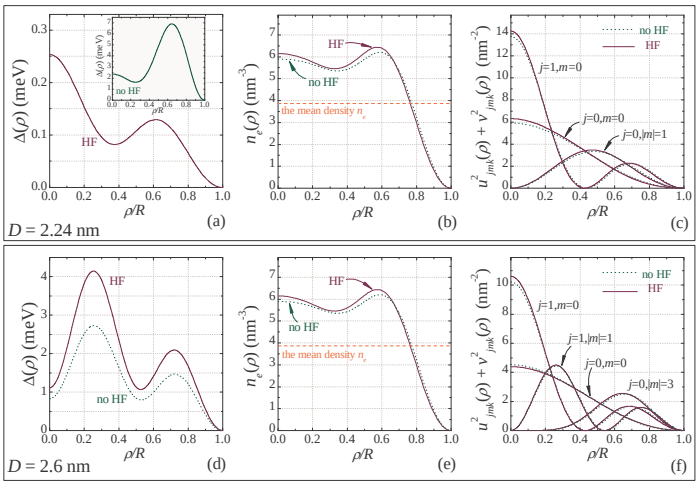

Fig. 2.3 Upper panel: (a) the superconducting order parameter $\Delta(\rho)$, (b) the local density $n_e(\rho)$ and (c) the distribution $u^2_{jmk}(\rho)+v^2_{jmk}(\rho)$ versus ρ/R for $D = 2.24\,\mathrm{nm}$. The lower panel: the same but for $D = 2.6\,\mathrm{nm}$. The results for the truncated (no HF) and full (HF) BdG equations are plotted.

effect on $n_e(\rho)$ as compared to the HF potential producing only some small corrections. From the results for the local electron density, it is possible to expect that the single-electron wave functions are also not very sensitive to the HF interaction. For nanowires, $|u_\nu(\mathbf{r})|$ and $|v_\nu(\mathbf{r})|$ is nearly proportional to the corresponding single-electron wave function [see discussion above, after Eq. (2.10)]. Hence, due to Eq. (2.9), the quantity $u^2_{jmk}(\rho) + v^2_{jmk}(\rho)$ can provide us with the information about the single-electron distribution. In Fig. 2.3(c) $u^2_{jmk}(\rho)+v^2_{jmk}(\rho)$ is plotted versus ρ/R for the quantum numbers most sensitive to including the HF interaction. We can indeed see that the effect of the HF potential on the wave functions is minor. Similar conclusions can be obtained from the lower panel of Fig. 2.3. The only exception is that the superconducting order parameter in Fig. 2.3(d) [$D = 2.6\,\mathrm{nm}$] does not change so much when including the HF potential. Notice that $n_e(\rho)$ given in Fig. 2.3(e) is practically the same as in Fig. 2.3(b). However, this is not true for $u^2_{jmk}(\rho) + v^2_{jmk}(\rho)$ [compare panel (c) with panel (f)]. The point is that the integral $\int_0^R \mathrm{d}\rho\,\rho\, n_e(\rho) = n_e R^2/2$ changes with the radius but for the single-electron distribution $u^2_{jmk}(\rho) + v^2_{jmk}(\rho)$ we have Eq. (2.9)].

From the results presented in Fig. 2.3, one expects minor effects on the single-electron wave functions due to the incorporation of the HF interaction . This expectation can be put on a more solid ground by using the Anderson approximation based on Eqs. (2.11) and (2.15). We remind that the Anderson approximation is quite good for superconducting nanowires provided that it

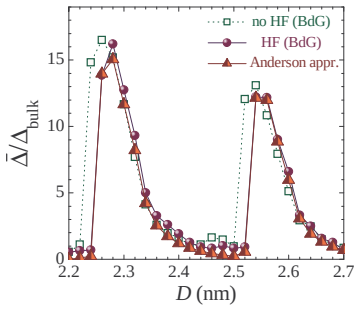

Fig. 2.4 $\bar{\Delta}/\Delta_{\rm bulk}$ versus the nanowire diameter ($T = 0$): triangles correspond to the Anderson approximation [the HF field is included]; stars and squares are the numerical results of the full and truncated BdG equations, respectively.

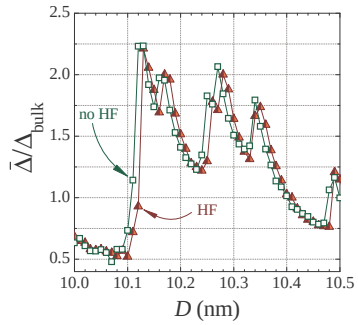

Fig. 2.5 HF versus no HF: $\bar{\Delta}/\Delta_{\rm bulk}$ as a function of the nanowire diameter D at zero temperature [squares are the results of the truncated BdG equations (no HF interaction); triangles are the results of the Anderson approximation, see Eqs. (2.11) and (2.15).

involves the true single-electron wave functions. Equations (2.11) and (2.15) follow from Eq. (2.10) and, hence, as assumed, the single-electron wave functions are not altered by our position-dependent HF interaction. If this is a reasonable assumption, results of the Anderson approximation constructed in this way, should be close to the results of the full BdG equations. As seen from Fig. 2.4, this is indeed the case. We can conclude that the thickness-dependent shift of the superconducting resonances in the presence of the HF interaction has nothing to do with the single-electron wave functions. Its mechanism is due to the fact that the position-dependent HF potential results in a change of the single-electron energies measured from the Fermi level.

So far we considered extremely narrow nanowires, for the sake of simplicity. However, a similar shift ($\approx 0.01-0.02$ nm) of the quantum-size oscillations due

to the HF term survives until the total decay of the quantum-size oscillations (up to diameters of about $50 - 70\,\mathrm{nm}$). In particular, such a shift is clearly seen in Fig. 2.5, where numerical results of the truncated BdG equations for $D = 10 - 10.5\,\mathrm{nm}$ are compared with a solution of Eqs. (2.11) and(2.15) including the HF potential. Thus, we arrive at the following picture. In the vicinity of a superconducting resonance, the bottom of some single-electron subband is situated close to the Fermi level. Therefore, a repositioning of this subband with respect to the Fermi level can result in a significant change of the number of single-electron states in the Debye window and, so, in a remarkable increase/decrease of superconducting characteristics. However, when bottoms of all single-electron subbands are quite apart from the Fermi level, i.e., in the off-resonant regime, a move of these subbands in energy produces much less important effect on the number of single-electron states located in the Debye window. This is why the decay of a superconducting resonance is accompanied by a depletion of the influence of the HF potential.

2.4 CONCLUSIONS

Quantum confinement breaks the translational symmetry in nanostructured superconductors. In this case, despite the delta-function approximation for the electron-electron interaction, the HF potential becomes position dependent, and its contribution to the single-electron energy (measured from the Fermi level) is a function of the relevant quantum numbers (contrary to bulk!). By numerically solving the BdG equations for a clean metallic nanocylinder, we have shown that such a feature results in a shift of the curve representing the thickness-dependent oscillations of the critical temperature (the energy gap, the order parameter etc.) to larger diameters. For metallic parameters it is of about the typical unit-cell dimensions. Notice that this is quite enough to completely change the pattern of thickness dependent oscillations of T_c between the Pb nanofilms with even and odd numbers of monolayers (see [3, 5, 19]). For low-carrier-density materials, e.g., superconducting semiconductors, such a shift increases significantly (proportionally to the relevant Fermi wavelength) and can reach the scale of few nanometers or even larger.

Publications. The results presented in this chapter were published as:

- **Yajiang Chen**, M. D. Croitoru, A. A. Shanenko, and F. M. Peeters, *Superconducting nanowires: quantum confinement and spatially dependent Hartree-Fock potential*, J. Phys.: Condens. Matter **21**, 435701 (2009).

3

Multisubband superconductivity in hollow nanocylinders

3.1 INTRODUCTION

Superconductivity in the presence of multiple bands can in general lead to a wealth of unusual superconducting phenomena, such as, e.g., Leggett's collective mode [76], Tanaka's soliton [77–79] and fractional flux [80, 81]. The reason is that the pair condensate can have different phases in different bands, which brings new degrees of freedom. The multi-subband structure induced by quantum confinement results in additional important possibilities. Formed due to the transverse quantization, subbands move in energy when changing the nanowire/nanofilm thickness. In particular, this leads to quantum-size oscillations accompanied by significant enhancements each time when the bottom of a new single-electron subband passes through the Fermi surface, i.e., the quantum-size superconducting resonance [20]. Recently, quantum-size oscillations of the critical superconducting temperature T_c and critical magnetic field H_{c2} have been observed in Pb nanofilms [3, 5, 19]. Furthermore, the results of a numerical self-consistent investigation of the BdG equations in Ref. [24] shows that the superconducting resonances are responsible for a systematic shift-up of T_c observed in aluminum and tin nanowires with a decrease in the cross-section [8–11, 16]. Other interesting effects can be expected in high-quality nanofilms and nanowires due to the formation of the multi-subband structure, e.g., Andreev-types states induced by quantum confinement [22] and a cascade character of the superconductor-to-normal transition driven by a magnetic field/supercurrent [23, 65]. All this makes it possible to expect that the multi-subband structure realized due to quantum confinement can open new prospects of tailoring superconducting properties by changing the main geometrical parameters of nanoscale superconductors.

Despite recent progress, many details of the superconducting state in the presence of the restricted dimensionality and multiple subbands remain unexplored. In particular, this concerns superconducting systems with an annular confining geometry, e.g., a hollow nanocylinder or nanoring, representing a promising choice for future superconducting nanodevices (see, e.g., recent papers on nanorings [82–85]). In the present Chapter we show that the superconducting condensate, energy gap and critical temperature of a hollow metallic nanocylinder (with inner radius R, and thickness d) can be strongly modified by changing R and d. The formation of multiple subbands results in quantum-size superconducting oscillations and in a multi-gap structure driven by the interplay of quantum confinement with Andreev mechanism. Quantum-size oscillations of the basic superconducting quantities as function of d exhibit a qualitative change from an irregular regime at small inner radii to almost regular oscillations for large R. At this crossover the multi-gap structure becomes degenerate. The ratio of the critical temperature to the energy gap increases and approaches its bulk value, while being reduced by 20%-30% due to Andreev-type states in the irregular regime. Our investigation is based on a numerical self-consistent solution of the BdG equations in the clean limit.

The Chapter is organized as follows. In Sec. 3.2, we outline the formalism of the BdG equations and discuss how to construct Anderson's approximate solution to the BdG equations for a hollow metallic nanocylinder. In Sec. 3.3 we demonstrate that results of a numerical solution of the BdG equations are in very good agreement with those of Anderson's approximation. This allows us to abandon time-consuming numerical study of the BdG equations in favor of solving the BCS-like equation. Then, the basic superconducting properties, i.e., the order parameter, energy gap and critical temperature, are investigated as function of the main geometrical parameters R and d.

3.2 FORMALISM

3.2.1 Bogoliubov-de Gennes equations for hollow nanocylinder

For the chosen geometry, the superconducting order parameter depends only on ρ (ρ, φ, z are the cylindrical coordinates), i.e., $\Delta(\mathbf{r}) = \Delta(\rho)$. It implies that we restrict ourselves to the case of zero net angular momentum of the condensate (no vortex) and zero net momentum along the z axis (no longitudinal supercurrent). States with a finite net angular momentum have a much higher kinetic energy in the case of interest. The particle-like and hole-like quasiparticle wave functions in the BdG equations Eqs. (1.45) can be represented as

$$u_n(\mathbf{r}) = u_n(\rho)\frac{e^{\imath m\varphi}}{\sqrt{2\pi}}\frac{e^{\imath kz}}{\sqrt{L}},\ v_n(\mathbf{r}) = v_n(\rho)\frac{e^{im\varphi}}{\sqrt{2\pi}}\frac{e^{ikz}}{\sqrt{L}}, \tag{3.1}$$

where $n = \{j, m, k\}$, j is the radial quantum number controlling the number of zeros of $u_n(\rho)$ and $v_n(\rho)$ for $R < \rho < R + d$, m is the azimuthal quantum

number, and k is the wave vector of the quasi-free electron motion parallel to the nanocylinder. Due to transverse quantum confinement

$$u_n(\mathbf{r})\Big|_{\rho=R} = u_n(\mathbf{r})\Big|_{\rho=R+d} = 0, \tag{3.2a}$$

$$v_n(\mathbf{r})\Big|_{\rho=R} = v_n(\mathbf{r})\Big|_{\rho=R+d} = 0, \tag{3.2b}$$

while periodic boundary conditions are used in the longitudinal and azimuthal directions.

For a numerical solution of the BdG equations, we expand the particle-like and hole-like radial wave functions $u_{jmk}(\rho)$ and $v_{jmk}(\rho)$ in terms of the single-electron radial wave functions $\psi_{jm}(\rho)$, i.e.,

$$u_{jmk}(\rho) = \sum_{j'} U_{jmk,j'}\psi_{j'm}(\rho), \tag{3.3a}$$

$$v_{jmk}(\rho) = \sum_{j'} V_{jmk,j'}\psi_{j'm}(\rho). \tag{3.3b}$$

We chose $u_{jmk}(\rho)$ and $v_{jmk}(\rho)$ real and, so, the expansion coefficients $U_{jmk,j'}$ and $V_{jmk,j'}$ are real, as well. Then, inserting Eq. (3.3) into BdG Eqs. (1.45), the expansion coefficients $U_{jmk,j'}$ and $V_{jmk,j'}$ can be calculated together with E_{jmk} by means of diagonalizing the relevant matrix. Iterations are invoked to realize a self-consistent solution. The wave-function $\psi_{jm}(\rho)$ is given by the equation

$$\Big[-\frac{1}{\rho}\frac{\partial}{\partial\rho}\rho\frac{\partial}{\partial\rho} + \frac{m^2}{\rho^2}\Big]\psi_{jm}(\rho) = \chi_{jm}^2\psi_{jm}(\rho), \tag{3.4}$$

where $\hbar^2\chi_{jm}^2/(2m_e)$ stands for the contribution of the radial and azimuthal motion to the single-electron energy. Due to the quantum-confinement boundary conditions given by Eq. (3.2), one should set

$$\psi_{jm}(\rho)\Big|_{\rho=R} = \psi_{jm}(\rho)\Big|_{\rho=R+d} = 0. \tag{3.5}$$

From Eqs. (3.4) and (3.5) it follows that $\psi_{jm}(\rho)$ can be written as

$$\psi_{jm}(\rho) = \frac{1}{\sqrt{\mathcal{M}}}\Big[Y_m(\chi_{jm}R)J_m(\chi_{jm}\rho) - J_m(\chi_{jm}R)Y_m(\chi_{jm}\rho)\Big], \tag{3.6}$$

where $J_m(x)$ and $Y_m(x)$ are the Bessel functions of the first and second kind of mth-order and the normalization constant M is given by

$$\mathcal{M} = \frac{\rho}{2}\Big[Y_m(\chi_{jm}R)J_{m+1}(\chi_{jm}\rho) - J_m(\chi_{jm}R)Y_{m+1}(\chi_{jm}\rho)\Big]\Big|_{\rho=R}^{\rho=R+d}. \tag{3.7}$$

The transverse single-electron energy $\chi_{jm} = \chi_{jm}(R,d)$ is a solution of

$$\begin{vmatrix} J_m(\chi_{jm}R) & Y_m(\chi_{jm}R) \\ J_m(\chi_{jm}(R+d)) & Y_m(\chi_{jm}(R+d)) \end{vmatrix} = 0, \tag{3.8}$$

which follows from Eq. (3.5). Notice that generally, χ_{jm} has a complicated dependence on the geometrical parameters R and d. However, in most cases χ_{jm} is controlled by d: for $R \to 0$ we get $\chi_{jm} \propto 1/d$, and a similar dependence is found for $R \to \infty$ or $d \to 0$. This can also be seen from the Heisenberg uncertainty principle because χ_{jm} can be interpreted as an average modulus of the transverse electron momentum.

Below we consider material parameters typical of aluminum: $\hbar\omega_D = 32.31$ meV; $gN(0) = 0.18$, with $N(0)$ the bulk density of states at the Fermi level. Notice that we apply the parabolic band approximation. This implies working with an effective Fermi level (for more details, see Ref. [25]). For aluminum $E_F = 0.9\,\text{eV}$, which was obtained through a good agreement with the experimental data in Ref. [24]. With decreasing thickness, as assumed that the electron density are constant, E_F systematically shifts up from 0.9 eV due to quantum-size effects. Such a shift can be appreciable (about 20%) for $d \sim$ 1-2 nm (E_F is almost insensitive to R). In addition, each time when a new single-electron subband passes through the Fermi surface, E_F exhibits a kink similar to the dependence of E_F on the radius of a cylindrical nanowire. [25] For the chosen parameters the bulk BCS coherence length and energy gap are $\xi_0 = 1.5\,\mu\text{m} \gg R, d$ and $\Delta_{\text{bulk}} = 0.25\,\text{meV}$, respectively. The particular choice of Al does not influence our conclusions. For instance, quantum-size oscillations in a Sn hollow nanocylinder will also be present but with an amplitude that is a factor of 2 smaller. In addition, by the same reason, we do not address any issue concerning a thickness-dependent change in the electron-phonon coupling. Its increase due to the surface softening of the phonon spectrum [86] or a possible substrate-induced decrease [3, 6] can result in quantitative effects but do not alter the qualitative picture.

3.2.2 Anderson's solution

Anderson's solution means that $u_{jmk}(\rho)$ and $v_{jmk}(\rho)$ are taken to be proportional to $\psi_{jm}(\rho)$ given by Eq. (3.6), i.e., the coefficients of the expansion in Eq. (3.3) are assumed to be of the form (see Sec. 1.2.3.2)

$$U_{jmk,j'} = \mathcal{U}_{jmk}\,\delta_{jj'},\; V_{jmk} = \mathcal{V}_{jmk}\,\delta_{jj'}, \tag{3.9}$$

with $\delta_{jj'}$ the discrete delta-function. In this case the single-electron energy reads

$$\xi_{jmk} = \frac{\hbar^2}{2m_e}(\chi_{jm}^2 + k^2) - E_F. \tag{3.10}$$

Inserting Eq. (3.9) into the BdG equations and, then, multiplying the resulting expressions by $\psi_{jm}(\rho)$, one can make a straightforward integration, which yields

$$E_{jmk} = \sqrt{\xi_{jmk}^2 + \Delta_{jm}^2}, \tag{3.11}$$

and

$$U_{jmk}V_{jmk} = \frac{\Delta_{jm}}{2\sqrt{\xi_{jmk}^2 + \Delta_{jm}^2}}, \tag{3.12}$$

with Δ_{jm} given by

$$\Delta_{jm} = \int_R^{R+d} \mathrm{d}\rho\, \rho\, \psi_{jm}(\rho)\Delta(\rho)\psi_{jm}(\rho). \tag{3.13}$$

Making use of the self-consistent condition of the order parameter together with Eqs. (3.9) and (3.12), one obtains the following BCS-like self-consistent equation:

$$\Delta_{j'm'} = -\sum_{jmk} J_{j'm',jm}\, \frac{\Delta_{jm}}{2E_{jmk}}\, [1 - 2f(E_{jmk})], \tag{3.14}$$

with the interaction matrix of the form

$$J_{j'm',jm} = -\frac{g}{2\pi L} \int_R^{R+d} \mathrm{d}\rho\, \rho\, \psi_{j'm'}^2(\rho)\psi_{jm}^2(\rho). \tag{3.15}$$

As mentioned above, Eq. (3.9) is a good approximation when there is no significant pairing between electrons from different subbands (i.e., non-time reversal pairing). It is more accuracy when the inter-subband energy spacing δ_{sub} is compatible with or larger than the Debye energy $\hbar\omega_D$: in such a case we have a negligible probability to pick up two non-time reversal single-electron states in the Debye window, i.e., $|\xi_{jmk}| < \hbar\omega_D$. The above energy spacing can be taken as $\delta_{\mathrm{sub}} \sim \frac{\hbar^2}{2m_e}(\chi_{j+1,m}^2 - \chi_{jm}^2)$. According to the remark about the dependence of χ_{jm} on R and d after Eq. (3.8), one can approximate δ_{sub} as $\delta_{\mathrm{sub}} \sim \frac{\hbar^2}{2m_e}\frac{\pi^2}{d^2}$, which is the inter-subband energy spacing for nanofilms. Using such a simplification, one obtains that Anderson's approximation given by Eq. (3.9) is good enough when

$$d \lesssim \pi\sqrt{\frac{\hbar}{2m_e\omega_D}}. \tag{3.16}$$

With typical metallic values $\hbar\omega_D \approx$ 10-30 meV, it follows from Eq. (3.16) that $d \lesssim$ 4-6 nm. In Sec. 3.3 we check this expectation through a numerical analysis. Note that Eq. (3.16) is a necessary but not a sufficient condition for the accuracy of Anderson's approximation (3.9). It can be poor when time-reversal symmetry is broken, e.g., in the presence of a magnetic field. In this case the orientation of a magnetic field is of importance. For instance, if it is parallel to the nanocylinder, one can still obtain quite accurate results with Eq. (3.9). This is because the single-electron wave functions are not very sensitive to such a magnetic field (they are the same in linear order in the vector potential $\mathbf{A}$, see Ref. [23]).

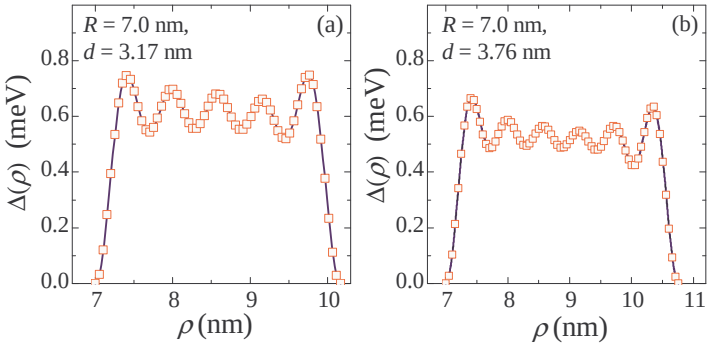

Fig. 3.1 (Color online) The order parameter $\Delta(\rho)$ [at $T = 0$] as calculated from the full BdG equations (solid curve) and from Anderson's approximation (open squares): (a) $R = 7\,\mathrm{nm}$, $d = 3.17\,\mathrm{nm}$; and (b) $R = 7\,\mathrm{nm}$, $d = 3.76\,\mathrm{nm}$.

3.3 RESULTS AND DISCUSSION

3.3.1 Accuracy of Anderson's solution

In Fig. 3.1 the zero-temperature order parameter is plotted versus ρ as calculated from a numerical procedure based on Eq. (3.3) (solid curve) and Anderson's approximation (open squares). Two particular sets of R and d are chosen: for $R = 7\,\mathrm{nm}$ we subsequently consider $d = 3.17\,\mathrm{nm}$ (a) and, $d = 3.76\,\mathrm{nm}$ (b). Each set represents a superconducting resonance and so $\Delta(\rho)$ is enhanced as compared to the bulk zero-temperature gap $\Delta_{\mathrm{bulk}} = 0.25\,\mathrm{meV}$. As seen, both solutions give practically the same results (differences are found to be less than 0.1%). For $R = 7\,\mathrm{nm}$ the centrifugal term in Eq. (3.4) almost does not change with m on the energy scale controlled by $\hbar\omega_D$, i.e., $\frac{\hbar^2}{2m_e}\frac{1}{\rho^2} \lesssim \frac{\hbar^2}{2m_e}\frac{1}{R^2} \approx 1\,\mathrm{meV} \ll \hbar\omega_D$. So, the single-electron states with different azimuthal quantum numbers are nearly degenerate. In particular, for $R = 7\,\mathrm{nm}$ and $d = 3.17\,\mathrm{nm}$ the lower edges of the single-electron subbands with $j = 4$ and $|m| = 0$-13 are located in the Debye window. This bundle of subbands makes major contribution to $\Delta(\rho)$ and other basic superconducting characteristics at this resonant point due to an enhanced density of states. At $d = 3.76\,\mathrm{nm}$ the bottoms of the subbands with $j = 5$ and $|m| = 0$-14 are positioned in the vicinity of E_F, which results in the resonance illustrated by Fig. 3.1(b). The number of local maxima of $\Delta(\rho)$ is equal to $j + 1$ and, so, increases by one when passing from panel (a) to panel (b). The contribution of a single-electron subband to the order parameter is given by $\sum_k u_{jmk}(\rho)v^*_{jmk}(\rho)(1 - 2f_{jmk}) \approx \psi^2_{jm}(\rho)\sum_k U_{jmk}V^*_{jmk}(1 - 2f_{jmk})$, which is an oscillating function of ρ with $j+1$ local maxima. Note that j is the number of nodes of $\psi_{jm}(\rho)$ between $\rho = R$ and $\rho = R + d$ so that $\psi^2_{jm}(\rho)$ has $j + 1$

local maxima. Therefore, when a superconducting resonance is governed by a bundle of nearly degenerate subbands with the same radial quantum number j, their input results in almost regular oscillations of $\Delta(\rho)$ as illustrated in Fig. 3.1. We remark that there are also superconducting resonances controlled by the subbands with different radial quantum numbers. In addition, when $R \to 0$ there are many examples of superconducting resonances controlled by simply one or two subbands. In such cases the order-parameter profile does not show regular oscillations. Its spatial distribution is very nonuniform and close to that of the pair condensate in a cylindrical nanowire (see, e.g., Ref. [25]). Any changes in the profile of the order parameter and its spatially averaged value do not have any effect on the accuracy of Anderson's solution: our numerical investigations for $R = 0$-$15\,\mathrm{nm}$ and $d = 0$-$10\,\mathrm{nm}$ shows negligible deviations (within 0.1-0.3 %) of the results of Eq. (3.9) from the full BdG as data as based on the procedure of Eq. (3.3).

Thus, to abandon time-consuming numerical investigations that are based on the expansion given by Eq. (3.3), we will use Anderson's recipe of an approximate semi-analytical solution to the BdG equations. As discussed above, corrections to this approximation are insignificant for $R = 0$-$15\,\mathrm{nm}$ and $d = 0$-$10\,\mathrm{nm}$. For larger values of d one can expect more pronounced deviations of Anderson's solution [87].

3.3.2 Quantum-size oscillations

Quantization of the transverse electron motion results in superconducting quantum-size oscillations, i.e., oscillations of the basic superconducting quantities when changing in the geometrical parameters of the sample. Fig. 3.2 shows how the spatially averaged superconducting order parameter $\bar{\Delta}$, i.e.,

$$\bar{\Delta} = \frac{2}{d(2R+d)} \int_{R}^{R+d} \mathrm{d}\rho\, \rho\, \Delta(\rho), \tag{3.17}$$

for different values of R at $T = 0$ (open squares). The same result for a superconducting nanofilm is shown by the solid curve. Panel (a) illustrates such thickness-dependent variations for $R = 1.0\,\mathrm{nm}$. As seen, the two sets of numerical results differ significantly from one another. It is known [20, 56] that the thickness-dependent resonant enhancements in superconducting nanofilms appear almost regularly, with period $\Delta d = \lambda_F/2$. For small d this period systematically decreases by about a few percent due to the shift-up of E_F when decreasing d. The reason for such a regular appearance is that the single-electron spectrum is proportional to ν^2/d^2, with ν the relevant quantum number controlling the transverse electron motion in nanofilms. This picture is different for nanowires. Here the quantum-size oscillations of superconducting properties are irregular [24]. The difference in width between two neighboring resonant enhancements strongly fluctuates along with their magnitudes. Note

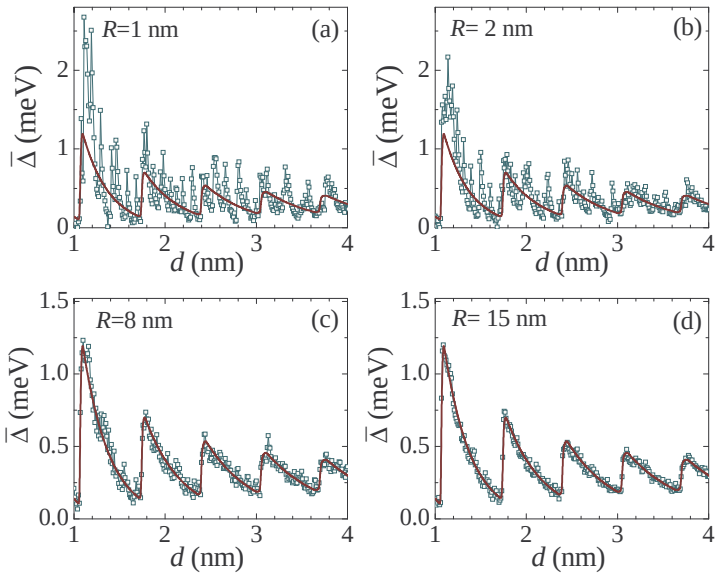

Fig. 3.2 (Color online) Crossover from an irregular to regular pattern of quantum-size oscillations: spatially averaged order parameter $\bar{\Delta}$ as function of d for inner radii $R = 1$, 2, 8 and 15 nm.

that the hollow superconducting nanocylinder for $R = 1.0\,\mathrm{nm}$ and $d = 1\text{-}4\,\mathrm{nm}$ exhibits rather nanowire-like irregular oscillations of $\bar{\Delta}$ that are super-imposed on top of the oscillations of $\bar{\Delta}$ in a corresponding nanofilm. From Fig. 3.2 we notice that with increasing R, the quantum-size oscillations in $\bar{\Delta}$ of a hollow nanocylinder approach more closely those of the corresponding nanofilm. However, the resonant enhancements over the bulk zero-temperature energy gap $\Delta_{\mathrm{bulk}} = 0.25\,\mathrm{nm}$ are still by a factor of two larger for the hollow nanocylinder. The centrifugal term $\frac{\hbar^2}{2m_e}\frac{m^2}{\rho^2}$ in Eq. (3.4) is still of importance here: for $\rho = R$ we have $\frac{\hbar^2}{2m_e}\frac{1}{R^2} \sim 9.52\,\mathrm{meV}$, which is not negligible as compared to the Debye energy $\hbar\omega_D = 32.31\,\mathrm{meV}$. Therefore, the single-electron subbands with different $|m|$ produce well distinguished resonant enhancements of $\bar{\Delta}$, and this is the reason for the irregular variations of $\bar{\Delta}$ shown for the hollow nanocylinder in Figs. 3.2(a,b). For $R \gtrsim 7\text{-}9\,\mathrm{nm}$ the centrifugal term in Eq. (3.4) plays a decreasing role, and the single-electron subbands with different $|m|$ become almost degenerate. This results in the formation of bundles of subbands with the same radial quantum number j and different $|m|$. When a bottom of such a bundle comes into the Debye window a superconducting resonance appears. While increasing R, the sequence of these resonances exhibits a more regular pattern and, finally, we arrive at the nanofilm regime of the quantum-size oscillations. As seen from Fig. 3.2(c) and (d), this regime is already well approached at $R = 8$ and $10\,\mathrm{nm}$. However, the deviations are still about 20% in panel (c) and are reduced to about 10% in (d). Thus, changing the geometrical parameters R and d results in a qualitatively different design of the single-electron subbands. The irregular distribution of the transverse electron levels at small R leads to irregular quantum-size oscillations of $\bar{\Delta}$ (and other basic superconducting quantities) with d [irregular regime]. For sufficiently large R the formation of bundles of the subbands with the same radial quantum number j but different m makes the quantum-size oscillations regular, yielding almost equidistant superconducting enhancements [regular regime] at $d_j = 1.09$, 1.79, 2.42, 3.1, and $3.75\,\mathrm{nm}$ for $j = 1\text{-}5$, respectively. The reason for the observed crossover from the irregular pattern to the regular regime is the interplay of quantum confinement and sample geometry.

Figure 3.3 adds more information to the discussion of the previous paragraph. Here the radial profiles of the order parameter $\Delta(\rho)$ are plotted for a series of the superconducting resonances. Inner radii are taken the same as in Fig. 3.2. Thicknesses are chosen so that to take the most profound resonant enhancement in the vicinity of $d = d_j$ for $j = 1\text{-}5$. (the concrete values of d are given in Fig. 3.3). When comparing these profiles with the spatial distribution of the pair condensate in aluminum nanofilms at $d = d_j$, [56] one can find pronounced differences for the irregular regime illustrated in panels (a) and (b). First of all, enhancements of $\Delta(\rho)$ for the nanocylinder are more significant, which can also be seen from Figs. 3.2(a,b). Second, nanofilms are specified by the symmetric order-parameter distribution, i.e., $\Delta(\rho)|_{\rho=R+x} = \Delta(\rho)|_{\rho=R+d-x}$. Such a symmetry does not generally hold for

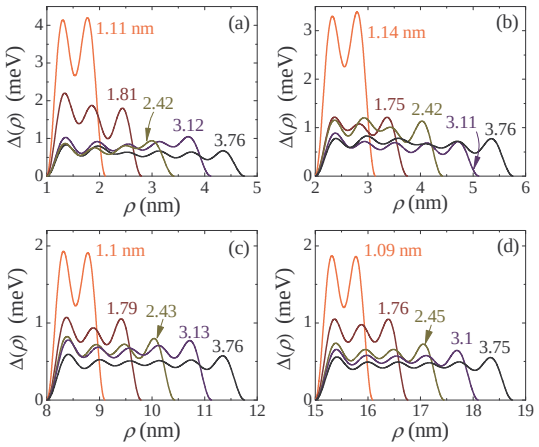

Fig. 3.3 (Color online) The radial distribution of the pair condensate in the hollow nanocylinder: (a) $R = 1$ nm and $d = 1.11$, 1.81, 2.42, 3.12, 3.76 nm; $R = 2$ nm and $d = 1.14$, 1.75, 2.42, 3.11, 3.76 nm; $R = 8$ nm and $d = 1.1$, 1.79, 2.43, 3.13, 3.76 nm; and $R = 15$ nm and $d = 1.09$, 1.76, 2.45, 3.1, 3.75 nm.

the hollow nanocylinder. This is clearly seen in panels (a) and (b). As for Figs. 3.3(c,d), we arrive at the regular regime and there are no significant deviations from the film-like spatial distribution of the superconducting condensate. As already mentioned in Sec. 3.3.1, here the number of local maxima of $\Delta(\rho)$ is equal to $j + 1$, where j is the radial quantum number related to the bundle of the subbands governing the corresponding superconducting resonance in the regular regime. The distance between two neighboring maxima is close to $\lambda_F/2$, with $\lambda_F = 2\pi\hbar/(2m_eE_F)^{1/2}$ the $3D$ Fermi wavelength for our effective Fermi level. Note that a superconducting resonance appears exactly at the point where the relevant bundle of single-electron subbands touches the Fermi surface. As the number of the local maxima in $\Delta(\rho)$ increases by one from a resonant to the next one, we can expect that the difference in d for two neighboring resonances is also $\lambda_F/2$. Recall that for $d = 1$-3 nm E_F is systematically shifted up from 0.9 eV with a decrease of d (see the discussion in the last paragraph of Sec. 3.2.1). Dependence of E_F on R is almost negligible.

Notice that, as seen from Eq. (3.14), the resonant enhancements of superconducting properties depend on the interaction matrix elements $J_{j'm',jm}$. So, a minor disorder, e.g., due to disordered interface between the sample and substrate or due to surface roughness, is expected to smoothen the quantum-size oscillations through the above matrix elements [88]. Another point is that such a disorder can also influence the mean density of single-electron states in the Debye window through a broadening of the transverse electron levels. In particular, this can somewhat shift superconducting resonances,

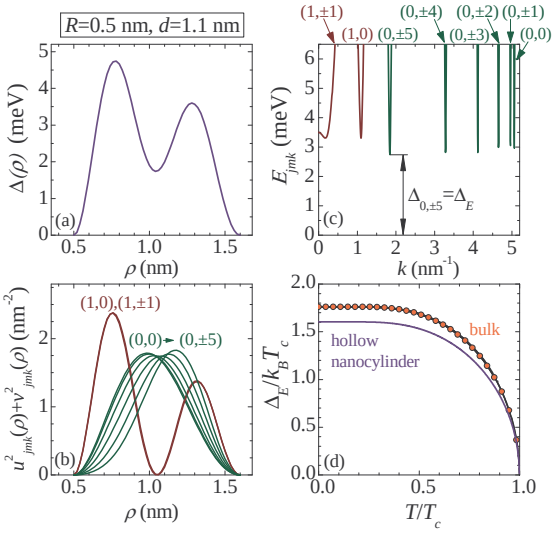

Fig. 3.4 (Color online) The hollow nanocylinder for $R = 0.5\,\mathrm{nm}$ and $d = 1.1\,\mathrm{nm}$): (a) the radial distribution of the pair condensate; (b) the quasiparticle energy E_{jmk} versus $k > 0$ for relevant single-electron subbands $(j, m) = (0, 0)$-$(0, \pm 5)$ and $(1, 0), (1, \pm 1)$; (c) the radial distributions of the corresponding quasiparticles; and (d) the ratio $\frac{\Delta_E}{k_B T_c}$ as function of T for the hollow cylinder (solid curve) and bulk (circles).

violating the regular pattern at large R. The broadening should exceed the inter-subband spacing δ_{sub} in order to completely destroy the formation of distinguished single-electron subbands. Note that tunneling experiments with single-crystalline Pb nanofilms demonstrate clear signatures of the formation of well distinguished transverse electron levels [5, 19, 60].

3.3.3 Andreev-type states induced by radial quantum confinement

As seen from Figs. 3.1, 3.2 and 3.3, the formation of multiple single-electron subbands results in significant modifications of the spatial distribution of the superconducting condensate and in quantum-size oscillations (both regular and strongly irregular) of basic superconducting properties. Another interesting consequence of the appearance of multiple subbands is the multi-gap structure of the quasiparticle excitations. As follows from Eq. (3.11), each single-electron subband is specified by Δ_{jm}, the energy gap of excitations in a given subband. Based on Eqs. (3.1), (3.9) and (3.11), this quantity can be represented as

$$\Delta_{jm} = \int \mathrm{d}^3 r [u^*_{jmk}(\mathbf{r})\Delta(\mathbf{r})u_{jmk}(\mathbf{r}) + v^*_{jmk}(\mathbf{r})\Delta(\mathbf{r})v_{jmk}(\mathbf{r})], \qquad (3.18)$$

i.e., Δ_{jm} is the average value of the order parameter as "seen" by quasiparticles in the corresponding single-electron subband. If the order parameter is uniform (e.g., in bulk), Δ_{jm} does not depend on the relevant quantum numbers because of the normalization condition [35], i.e., $\int \mathrm{d}^3 r[|u_{jmk}(\mathbf{r})|^2 + |v_{jmk}(\mathbf{r})|^2] = 1$. In the presence of quantum confinement the superconducting order parameter is always position dependent due to a broken translational symmetry and, so, we obtain energy gaps sensitive to the quantum numbers, i.e., the multi-gap case. From Eq. (3.18) it follows that when quasiparticles are successive in avoiding local enhancements in $\Delta(\mathbf{r})$, they are specified by smaller Δ_{jm}'s and, so, by generally lower energies: to some extent a spatial variation of the superconducting order parameter appears to be analogous to a potential well for quasiparticles. This is the basis of the well-known Andreev reflection (see, e.g., Refs. [89] and [22]) which we refer to as Andreev mechanism. Its interplay with quantum confinement is illustrated by Fig. 3.4 for $R = 0.5\,\mathrm{nm}$ and $d = 1.1\,\mathrm{nm}$ (the point of a superconducting resonance). Here panels (a) and (b) show the order parameter and the radial distribution of quasiparticles $u^2_{jmk}(\rho) + v^2_{jmk}(\rho) = \psi^2_{jm}(\rho)$ (the latter does not depend on k in Anderson's approximation). There are eight relevant subbands making a contribution to the superconducting characteristics at the chosen geometrical parameters: $(j,m) = (0,0)$-$(0,\pm5)$ and $(1,0)$-$(1,\pm1)$. The bottom of the single-electron subband with $(j,m) = (1,\pm1)$ is situated in the vicinity of the Fermi surface and, so, it makes a major contribution to $\Delta(\rho)$ due to an enhanced density of states. This is the subband that controls the resonant enhancement at $R = 0.5\,\mathrm{nm}$ and $d = 1.1\,\mathrm{nm}$ (resonant subband) and determines the corresponding radial profile of the order parameter with the two local maxima [compare with the radial distribution of quasiparticles $(1,\pm1)$ in panel (b)]. Other subbands play a less important role at this superconducting resonance. The most significant contribution among them is due to the states with $(j,m) = (1,0)$. As these states have practically the same radial distribution as those with $(j,m) = (1,\pm1)$ [the curves for $(1,\pm1)$ and $(1,0)$ in Fig. 3.4(b) are almost indistinguishable), then, based on Eq. (3.18), one can expect that $\Delta_{1,0}$ should be nearly the same as $\Delta_{1,\pm1}$. This expectation agrees with our numerical results given in Fig. 3.4(c). Here the quasiparticle energy E_{jmk} is plotted versus the positive values of k and, as seen, each single-electron subband is specified by its own quasiparticle branch whose minimum energy gives the subband superconducting gap.

By virtue of the definition of j (the number of nodes in the radial direction), the spatial distribution of quasiparticles with $j = 0$ is characterized by one maximum [see panel (b)] located next to the point of a local minimum of $\Delta(\rho)$ at $\rho \approx 1.05\,\mathrm{nm}$. Therefore, Δ_{jm} is generally lower for $j = 0$ [see Fig. 3.4(c)] and, so, quasiparticles with $(j,m) = (0,0)$-$(0,\pm5)$ can be interpreted as Andreev-type states induced by the radial quantum confinement. The total energy gap in the quasiparticle spectrum Δ_E is determined by the lowest subband-dependent gap, i.e., $\Delta_E = \Delta_{0,\pm5}$, see panel (c). Due to a relatively small density of states, such Andreev-type quasiparticles produce only

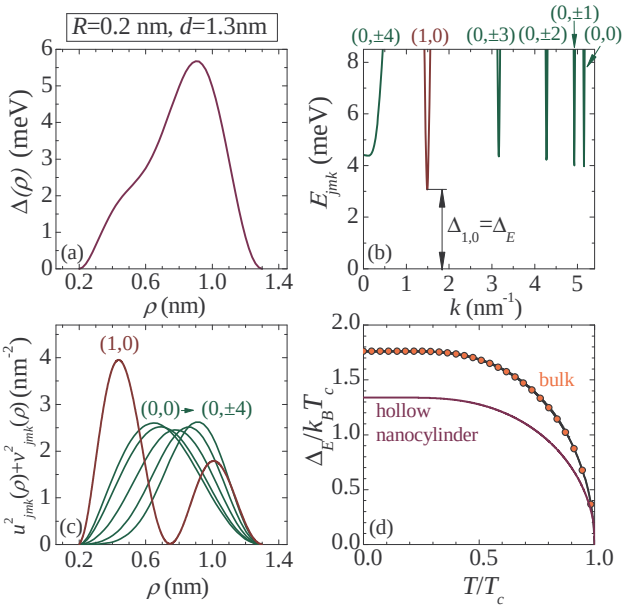

Fig. 3.5 (Color online) The same as in the previous figure but for $R = 0.2\,\text{nm}$, $d = 1.2\,\text{nm}$).

a minor contribution to the basic superconducting characteristics, e.g., the critical temperature. However, they control the low-lying energy excitations in a superconductor. This is illustrated by Fig. 3.4(d), where the ratio of Δ_E to T_c is shown as function of temperature. Subband $(0, \pm 5)$ has the lowest energy gap and determines Δ_E but does not make a significant contribution to T_c. The latter is controlled by the resonant subband $(1, \pm 1)$ with the higher energy gap. This is why the ratio Δ_E/k_BT_c is decreased as compared to bulk. As seen from panel (d), such a decrease is about 10%. This is by a factor of 2 smaller than the reduction of Δ_E/k_BT_c due to similar Andreev-type states in a cylindrical nanowire with radii 1-2 nm. [22] The point is that the superconducting condensate in a hollow nanocylinder exhibits generally more uniform spatial patterns, which results in a less profound difference between subband-dependent gaps. The centrifugal energy appears to be a significant contributor to a nonuniform distribution of the pair condensate, and the role of this term is reduced due to the annulus in a hollow nanocylinder. This is the reason why the Andreev-type states play a more important role with decreasing R. This is seen from Fig. 3.5 that shows the same data as in Fig. 3.4 but for $R = 0.2\,\text{nm}$ and $d = 1.1\,\text{nm}$, i.e., for nearly the same thickness as previously but for a significantly smaller inner radius.

The superconducting resonance illustrated by Fig. 3.5 is governed by the single-electron subband with $(j, m) = (0, \pm 4)$ and, as seen, the maximum of $\Delta(\rho)$ is located at the same point as the maximum of the radial quasiparticle distribution for $(j, m) = (0, \pm 4)$. In addition to states $(0, \pm 4)$, there are five more single-electron subbands making a minor contribution to the superconducting characteristics. Four of them are specified by $j = 0$ and, so, spatial distributions of the corresponding quasiparticles are close to that of the resonant subband. So, there is a minor difference between Δ_{jm}'s with $j = 0$. However, it is clearly seen that Δ_{jm} (with $j = 0$) is slightly diminished when decreasing $|m|$. The reason is that the maximum of the quasiparticle distribution for the states with $j = 0$ is shifted to smaller ρ with decreasing $|m|$. It means that the value of the corresponding integral in Eq. (3.18) is reduced. One more relevant single-electron subband is $(j, m) = (1, 0)$. The radial distribution of the quasiparticles in this subband has two local maxima and the most significant of them is located far to the left from the maximum of $\Delta(\rho)$. As a result, we obtain a significant drop of $\Delta_{1,0}$ as compared to the energy gap of the resonant subband, i.e., $\Delta_{0,\pm 4}$. Such a drop leads to a significant decrease (now it is about 20%) in the ratio Δ_E/k_BT_c, where $\Delta_E = \Delta_{1,0}$ and T_c is controlled by the states with $(j, m) = (0, \pm 4)$ (notice the reasonable estimate $k_BT_c \approx 1.76\Delta_{0,\pm 4}$).

For non-resonant sets of R and d, when the bottoms of all relevant subbands are far below the Fermi level, the order parameter (and T_c) is not enhanced as compared to bulk and exhibits, as a rule, a more uniform spatial distribution. In this case the Andreev mechanism plays a less important role and the ratio Δ_E/k_BT_c is close to its bulk value. However, deviations from bulk can still be significant, see Ref. [22] and, so, this effect of Andreev-type states induced by quantum confinement can be observed even in the presence of fluctuations of the transverse dimensions R and d when all the results should be averaged over relevant intervals of their variations.

Interplay of the Andreev mechanism and quantum confinement in nanoscale superconductors can be probed experimentally by means of simultaneous measurements of T_c and Δ_E. So, it is interesting to have an idea about how the quasiparticle density of states measured in tunneling experiments, is modified by quantum confinement. The dependence of this density of states on the quasiparticle energy E (in units of $\Delta_{\rm bulk}$) is illustrated for a hollow nanocylinder by Fig. 3.6 for: (a) $R = 0.5\,$nm and $d = 1.1\,$nm; (b) $R = 2.0\,$nm and $d = 1.1\,$nm; and (c) $R = 1.0\,$nm and $d = 1.77\,$nm [all sets are resonant points]. In addition, panel (d) shows the quasiparticle energy E_{jmk} versus $k > 0$ for the latter set of R and d. Multiple peaks (more precisely, multiple square-root type of divergences) in the quasiparticle density of states [in units of $N(0)$, the bulk normal density of states] reflects the formation of the multi-gap structure. In particular, in panel (a) we can see a significant peak at $E \approx 13.2\,\Delta_{\rm bulk}$ and two less important peaks at $E/\Delta_{\rm bulk} = 11$ and 11.5. The major peak is due to the contribution of quasiparticles from the resonant single-electron subband with $(j, m) = (1, \pm 1)$ [see Fig. 3.4(c)]. Two

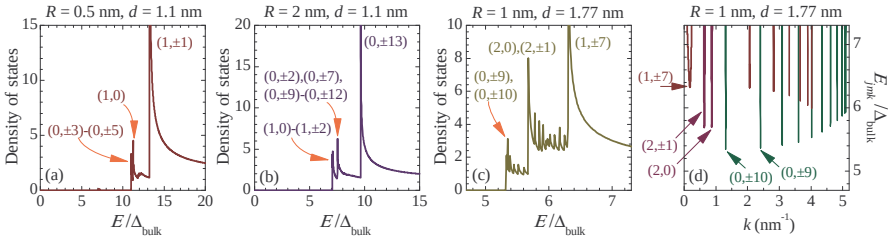

Fig. 3.6 (Color online) The quasiparticle density of states in the irregular regime: (a) for $R = 0.5\,\text{nm}$, $d = 1.1\,\text{nm}$; (b) for $R = 2.0\,\text{nm}$, $d = 1.1\,\text{nm}$; (c) for $R = 1.0\,\text{nm}$, $d = 1.77\,\text{nm}$. Panel (d) shows E_{jmk} as dependent on k for the same parameters as in (c).

small peaks shifted towards smaller energies are due to Andreev-type states induced by the radial quantum confinement, i.e., $E = 11.5\,\Delta_{\text{bulk}}$ comes from $(j, m) = (1, 0)$ and $E = 11\,\Delta_{\text{bulk}}$ is from $(j, m) = (0, \pm 3)$-$(0, \pm 5)$. There are additional divergences in the quasiparticle density of states at $E = 12$-$13\,\text{meV}$. They are associated with the single-electron subbands $(0, 0)$-$(0, \pm 2)$. The corresponding peaks in panel (a) are thin and practically invisible.

A similar picture occurs for $R = 2.0\,\text{nm}$ and $d = 1.1\,\text{nm}$. As seen from Fig. 3.6(b), we again obtain one major peak due to the resonant subband labeled now by $(j, m) = (0, \pm 13)$ (at $E/\Delta_{\text{bulk}} = 9.6$). In addition, there are two less pronounced peaks: at $E/\Delta_{\text{bulk}} = 7$ due to the subbands $(1, 0)$-$(1, \pm 2)$ and at $E/\Delta_{\text{bulk}} = 7.6$ from subbands $(0, \pm 2), (0, \pm 7)$ and $(0, \pm 9)$-$(0, \pm 12)$. Peaks from other subbands almost disappear.

For more specific information, Fig. 3.6(c) shows all peaks in the quasiparticle density of states, both significant and secondary in importance, at a more detailed energy scale for $R = 1.0\,\text{nm}$ and $d = 1.77\,\text{nm}$. For convenience, panel (d) demonstrates E_{jmk} as function of k for the same parameters. These parameters correspond to a superconducting resonance induced by the single-electron subband with $(j, m) = (1, \pm 7)$ that makes a major contribution to the basic superconducting quantities and is specified by the subband gap $\Delta_{1,\pm 7} = 6.35\,\Delta_{\text{bulk}}$ [see panel (d)]. As a result, we have a profound major peak at $E/\Delta_{\text{bulk}} = 6.3$ in Fig. 3.6(c). It is seen from Fig. 3.6(d) that there is also a subband with $(j, m) = (1, \pm 6)$ which is characterized by nearly the same superconducting gap, i.e., $\Delta_{1,\pm 6} \approx \Delta_{1,\pm 7}$. However, its contribution to the density of states is much less significant. The second important peak is situated at $E/\Delta_{\text{bulk}} = 5.7$, which is the energy gap for subbands $(2, 0)$ and $(2, \pm 1)$: $\Delta_{2,0} = \Delta_{2,\pm 1} = 5.7\,\Delta_{\text{bulk}}$. The third pronounced peak in Fig. 3.6(c) forms due to two divergences in the density of states due to the subbands $(0, \pm 9)$ and $(0, \pm 10)$. Here $\Delta_{0,\pm 9} \approx \Delta_{0,\pm 10} = 5.3\,\Delta_{\text{bulk}}$, see Fig. 3.6(d). In addition, one can see clear signatures of less important divergences in Fig. 3.6(c). In particular, between the two significant peaks located at $E/\Delta_{\text{bulk}} = 5.7$ and $E/\Delta_{\text{bulk}} = 6.3$, there are a series of peaks coming from the subbands with

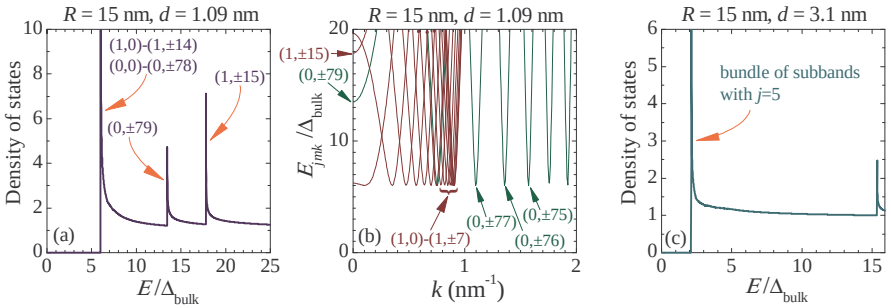

Fig. 3.7 (Color online) Hollow nanocylinder in the regular regime: (a) the quasiparticle density of states versus the energy E at $R = 15\,\mathrm{nm}$ and $d = 1.09\,\mathrm{nm}$; (b) E_{jmk} as function of k [in the interval $k = 0\text{-}2\,\mathrm{nm}^{-1}$] for the relevant single-electron subbands with $(j, m) = (0, 0)\text{-}(0, \pm 79)$ and $(1, 0)\text{-}(1, \pm 15)$; and (c) the density of states versus the quasiparticle energy E for $R = 15\,\mathrm{nm}$ and $d = 3.1\,\mathrm{nm}$.

$(j, m) = (1, 0)\text{-}(1, \pm 6)$ (the larger the absolute value of the azimuthal quantum number the smaller the corresponding subband energy gap). In turn, the subbands $(0, 0)\text{-}(0, \pm 8)$ are responsible for a series of peaks in the energy domain $E/\Delta_{\mathrm{bulk}} = 5.3\text{-}5.7$.

As mentioned above, the formation of Andreev-type states induced by quantum confinement is related to a spatially nonuniform distribution of the pair condensate. In the regime of irregular quantum-size oscillations (see Sec. 3.3.2), i.e., for sufficiently small R, the order parameter exhibits pronounced spatial variations, which results in a significant role of the Andreev mechanism. When increasing R, we pass to the regime of regular quantum-size oscillations because single-electron subbands with different absolute values of the azimuthal quantum number are almost degenerate for large enough R and form bundles. In this case the spatial variations of $\Delta(\rho)$ become less and less pronounced and, as a result, the multi-gap structure disappears. In particular, Figs. 3.7(a, b) show the quasiparticle density of states and the quasiparticle energy as function of k for $R = 15\,\mathrm{nm}$ and $d = 1.09\,\mathrm{nm}$. This is the point of a superconducting resonance induced by a bundle of single-electron subbands with $j = 1$. The states with $(j, m) = (1, 0)\text{-}(1, \pm 14)$ makes a contribution to the superconducting characteristics of about 60% here. The rest is due to the subbands $(0, 0)\text{-}(0, \pm 79)$. As seen from Fig. 3.7(b), the quasiparticle branches with $(j, m) = (0, \pm 7)$ are almost degenerate. However, branches with $j = 1, |m| > 7$ are still well distinguished. Andreev mechanism is of no importance any more and, so, the subband energy gaps do practically not depend on the quantum numbers: $\Delta_{jm} = 6\Delta_{\mathrm{bulk}}$ for $(j, m) = (1, 0)\text{-}(1, \pm 14)$ and $(0, 0)\text{-}(0, \pm 78)$. Therefore, we can see a profound peak in the quasiparticle density of states at $E/\Delta_{\mathrm{bulk}} = 6$. There are two additional subbands $(0, \pm 79)$ and $(1, \pm 15)$ that contribute to the superconducting quantities. As follows from

Fig. 3.7(b), the spectroscopic gaps for these states are $13.5\,\Delta_{\rm bulk}$ and $18\,\Delta_{\rm bulk}$ with the corresponding peaks in Fig. 3.7(a). These spectroscopic gaps are not directly related to $\Delta_{0,\pm 79}$ and $\Delta_{1,\pm 15}$ because the bottoms of both subbands are located above the Fermi level (but in the Debye window). It means that ξ_{jmk} is different from zero at the point of the minimum of the corresponding quasiparticle energy E_{jmk} taken as function of k [see Eq. (3.11)]. Hence, the above spectroscopic gaps are shifted up by a nonzero single-electron energy. It is interesting that $\Delta_{0,\pm 79}$ and $\Delta_{1,\pm 15}$ are smaller than $6\Delta_{\rm bulk}$. However, this does not have any effect on the ratio of Δ_E to $k_B T_c$: these subbands produce a negligible contribution to the superconducting characteristics due to the large corresponding spectroscopic gaps. In Fig. 3.7(c) one can see another example of the energy dependence of the quasiparticle density of states. Thus, as seen, the multi-gap structure is almost degenerate in the regular regime and Andreev-type states do not play such essential role as for smaller inner radii, i.e., in the case of irregular quantum-size oscillations.

Concluding this section, we note that the radial profile of the superconducting order parameter is mainly determined by single-electron subbands with the bottoms close to the Fermi surface. These subbands are characterized by slow motion of electrons in the direction parallel to the nanocylinder (here the major part of the corresponding single-electron energy comes from the radial and azimuthal degrees of freedom). In particular, typical longitudinal wavelengths for electrons in a resonant subband are about $20\,{\rm nm} \gg \lambda_F$. Propagation of such long waves is not sensitive to the surface imperfections with the characteristic size of the order of the metallic unit-cell dimensions. Thus, the profile of the order parameter and, so, the formation of Andreev states induced by quantum confinement will be stable against surface roughness.

3.4 CONCLUSIONS AND DISCUSSIONS

By numerically solving the BdG equations, we have investigated how quantum confinement modifies superconductivity in a hollow metallic nanocylinder. The radial quantization of the electron motion results in a splitting of the conduction band into a series of subbands whose lower edges move in energy when changing the inner radius R and thickness d. Such a multi-subband structure leads to pronounced quantum-size superconducting oscillations, e.g., the superconducting properties varies with d at a fixed R. We have found that the character of these variations changes qualitatively with an increase in R: the irregular pattern is replaced by almost equidistant superconducting resonant enhancements. The reason for such a crossover is the change of the role of the centrifugal energy. When R increases, this energy is diminished so that single-electron subbands with different absolute values of the azimuthal quantum number m (but with the same radial quantum number j) are nearly degenerate in energy. As a result, they form bundles of subbands responsible for equidistant resonant enhancements in the basic superconducting quantities

as functions of d. We have shown that the formation of subbands can result in multiple superconducting gaps due to the interplay between quantum confinement and the Andreev mechanism. The difference between the subband-dependent superconducting gaps is significant in the irregular regime but they are almost equal when coming to the regular side of the crossover. Here the ratio of the critical temperature to the energy gap approaches its bulk value while it is reduced by 20%-30% due to Andreev-type states in the irregular regime. The role of Andreev-type states induced by quantum confinement is significant for small inner radii but becomes minor in the regular domain.

We would like to remark that fluctuations are known to play a more serious role for lower dimensionality. So, one can expect deviations from the mean-field results for nanoscale superconducting systems. However, a recent experimental study of Pb superconducting single-crystalline nanofilms showed a good agreement with the mean-field results even for film thicknesses down to 2-5 monolayers (0.5-1.0 nm) [19]. For superconducting nanowires it is believed [90] that quantum-phase fluctuations suppress the superconducting state for diameters below 5-8 nm. This expectation is in agreement with the experimental results of Ref. [9], where a crossover from the superconducting to normal state was reported for an aluminum nanowire with a diameter of about 8 nm. However, results of another group [10] demonstrate no signature of such a crossover in aluminum nanowires with diameters 5-6 nm. Thus, based on the above experimental data, we may expect that the mean-field approach is reasonable for hollow nanocylinder when $d \gtrsim 1\,\text{nm}$ and $R + d \gtrsim$ 2-3 nm, with $R + d$ the total radius of the hollow cylinder. In addition, we remark that the existing treatment of superconducting fluctuations is questionable in the presence of multiple single-electron subbands in nanowires/nanofilms. Due to scattering of electrons between different subbands, this has nothing to do with the 1D/2D limit and, so, the superconducting fluctuations, both quantum and thermal, will be different. Thus, one can expect that when the number of the relevant single-electron subbands is significantly larger than one, the 3D case is being approached and the mean-field approximation is justified. However, even when only a small number of subbands is occupied, the mean-field approximation can still yield reasonable results like in Pb and In single-crystalline one-atomic-layer thick films [13] with only one relevant single-electron subband.

We also note that some smearing of the spatial profile of the order parameter can be expected when including the nonlocal-gap operator in the BdG equations. More specifically, using a nonlocal-gap representation of the BdG equations, one simply avoids the delta-function approximation of the pair interaction in favor of a more detailed potential. Then, when solving Anderson's BCS-like equation [see Eq. (3.14)], the only difference is that new interaction-matrix elements $J_{j'm',jm}$ will appear in the problem. While resonant enhancements can be sensitive to the interaction-matrix elements, this is not the case for the radial profile of the order parameter that is governed by quantum confinement. Indeed, the main contribution to the order parameter at a res-

onant point comes from the single-electron subband whose bottom is in the vicinity of the Fermi surface. It means that, by virtue of Eq. (3.9), the radial profile of the order parameter is determined by the radial single-electron wave function associated with the above subband. Hence, the spatial profile of the order parameter will change only if the relevant single-electron wave functions will be different. However, such a difference will not be pronounced because the electron-electron interaction itself has almost no effect on the wave functions in superconducting nanowires/nanofilms. From the numerical results of Ref. [91], this effect is estimated to be within a few percent. In other words, the order parameter is directly related to the Cooper-pair wave function, and a wave function of two particles in a quantum-confining geometry is much more sensitive to tight confinement than to details of the interparticle interaction. Generally, the strength of quantum confinement in nanowires/nanofilms can be specified by the dimensionless parameter $\delta_{\rm sub}/\Delta_{\rm bulk}$: when it is larger than one, quantum-confinement effects predominate. For nanowires $\delta_{\rm sub} \sim \frac{\hbar^2}{2m_e}\frac{\pi^2}{\mathbb{R}^2}$, with $\mathbb{R}$ the nanowire radius (we note that for a hollow nanocylinder $\mathbb{R}$ is a complicated function of R and d). Typical values for the energy gap in bulk metallic superconductors are $\Delta_{\rm bulk} = 0.1\text{-}1.5\,{\rm meV}$ (see, e.g., Ref. [90]). This allows one to find that $\delta_{\rm sub}/\Delta_{\rm bulk} > 1$ when $\mathbb{R} < 20 - 80\,{\rm nm}$. In particular, for aluminum this leads to $\mathbb{R} < 40\,{\rm nm}$.

It is also of interest to discuss the possible effect of surface imperfections on the superconducting resonances in quantum nanowires. Surface roughness can influence both the longitudinal and transverse motion of electrons. As discussed above, the basic characteristics of the system at the point of a superconducting resonance are controlled by the corresponding resonant single-electron subband whose bottom is situated in the vicinity of the Fermi level. In such a subband the main contribution to the single-electron energy comes from the transverse motion and, so, the longitudinal motion of electrons is slow. In particular, from Figs. 3.4 we learn that the resonant subband at $R = 0.5\,{\rm nm}$ and $d = 1.1\,{\rm nm}$ is specified by $(j, m) = (1, \pm 1)$, and the corresponding subband-dependent longitudinal Fermi wavenumber is about $0.2 - 0.3\,{\rm nm}^{-1}$. Similar values for the the longitudinal Fermi wavenumber in the resonant subband with $(j, m) = (0, \pm 4)$ can be found from Fig. 3.5 for $R = 0.2\,{\rm nm}$ and $d = 1.3\,{\rm nm}$. In general, the characteristic longitudinal wavelengths of electrons in a resonant subband are larger than 15-30 nm. Propagation of such long waves will not be sensitive to surface imperfections with characteristic sizes of about the dimensions of the metallic unit cell. Another possible effect of surface roughness is a broadening of the transverse electron levels and, consequently, a smearing of the lower edge of a single-electron subband. This will lead to an uncertainty in the inter-subband energy spacing and, so, one can expect that when this uncertainty is close to or larger than the Debye energy $\hbar\omega_D$, an effect of such a smearing on quantum-size oscillations of basic superconducting properties can be pronounced. The uncertainty in the inter-subband energy spacing for nanowires is estimated as

$\Delta\delta_{\rm sub} = \frac{\pi^2\hbar^2}{m_e\mathbb{R}^3}\Delta\mathbb{R}$, with $\Delta\mathbb{R}$ the characteristic length of the radius fluctuations. Taking $\Delta\mathbb{R} = 0.3\,$nm we can obtain that $\Delta\delta_{\rm sub} = 30\,$meV for $\mathbb{R} = 2\,$nm whereas $\Delta\delta_{\rm sub} = 8\,$meV for $\mathbb{R} = 3\,$nm. The Debye energy for aluminum is about $32\,$meV, see discussion in the last paragraph of Sec. 3.2.1. Hence, smearing for quantum-size oscillations of the basic superconducting quantities due to surface roughness can be expected for aluminum nanowires with radii less than $2\,$nm. Thus, in a hollow nanocylinder such a smearing can be of relevance for $R + d < 2\,$nm.

Publications. The results presented in this chapter were published as:

- **Yajiang Chen**, A. A. Shanenko, and F. M. Peeters, *Hollow nanocylinder: Multisubband superconductivity induced by quantum confinement*, Phys. Rev. B **81**, 134523 (2010).

4

Quantum cascades in superconducting hollow nanocylinders

4.1 INTRODUCTION

For metallic nanofilms and nanowires in the clean limit, quantum confinement of the perpendicular motion of electrons splits the conduction band into a series of subbands. This leads naturally to *multiband superconductivity* similar to, e.g., the two-band superconductivity as found in novel superconductors such as MgB_2 (see, e.g., [92]) and the iron-pnictides (see, e.g., [93]). The formation of multiple subbands has a significant effect on the superconducting properties when the intersubband energy spacing $\delta_{\rm sub} \approx \frac{\hbar^2}{2m_e}\frac{\pi^2}{a^2}$ (with a the nanowire/nanofilm thickness) becomes of the order of the bulk energy gap $\Delta_{\rm bulk}$. For conventional superconductors, say, aluminum or tin, $\Delta_{\rm bulk} = 0.3 - 0.7\,{\rm meV}$ (see, e.g., textbooks [35, 67]) and, so, $\delta_{\rm sub}$ exceeds $\Delta_{\rm bulk}$ when $a \lesssim 30 - 40\,{\rm nm}$. Thus, before being eventually suppressed in lower dimensions, superconductivity in high-quality nanofilms/nanowires exhibits an almost unexplored regime governed by quantum confinement, i.e., the regime of nanoscale superconductivity.

The presence of multiple subbands causes many effects which may not be observed in bulk superconductors, e.g., quantum-size superconducting resonances and related quantum-size oscillations of the basic superconducting properties [20, 24–26, 56, 94, 95], the formation of Andreev states induced by quantum confinement [22, 68], giant size-dependent drops of the BCS coherence length [27] etc. In the present Chapter we focus on another interesting effect due to multiple subbands in nanoscale superconductors, i.e., quantum cascades induced by a magnetic field. It was recently shown [23] that the superconducting-to-normal transition in quantum nanowires driven by a parallel magnetic field occurs as a cascade of jumps in the order parameter as

a function of the magnetic field. The magnetic field does not "kill" superconductivity simultaneously in all relevant single-electron subbands and the field-induced decay of superconducting correlations occurs step by step, i.e., first in one subband, then in another and so on. This results in a cascade of transitions. At zero temperature the cascade structure was predicted [23] to be pronounced in nanowires with diameters $\lesssim 15\,\mathrm{nm}$, which is an experimentally reachable domain. Here we extend Ref. [23] and consider the impact of the confining geometry and thermal effects on these quantum cascades. Additionally, we take into account the spin-magnetic-field interaction and study quantum-size oscillations of the paramagnetic limiting field [96]. Our work is based on a numerical solution of the BdG equations for a hollow metallic nanocylinder. Varying its inner radius R and its wall thickness d, we can switch from nanowire-like ($R/d \ll 1$) to nanofilm-like ($R/d \gg 1$) scenario and back [97]. We also investigate how the cascades are influenced by surface roughness that is the main issue of disorder in high-quality nanoscale superconductors. The Ginzburg-Levanyuk parameter Gi (Gi $\sim \delta T/T_c$, with T_c the critical temperature and δT the temperature range where thermal fluctuations are of importance) is not extremely large in high-quality superconducting nanowires, i.e., Gi $\approx$ 0.1-0.2 for diameters 5-10 nm (see discussion in Sec. 4.4). For wires with widths $\lesssim 8\,\mathrm{nm}$ quantum-phase fluctuations are expected to be of crucial importance. However, the phase-slip rates and the related long tail in the resistance below T_c depend on the mean-field order parameter (see, e.g., [9, 10]). Thus, the quantum cascades can be observed in the magnetic-field dependence of such low-temperature resistance tails even for extremely narrow wires.

This Chapter is organized as follows. In Sec. 4.2 we outline the formalism of the BdG equations for a hollow metallic nanocylinder in the presence of a parallel magnetic field (with only the interaction of the orbital magnetic moments with the external magnetic field). Further in this section we discuss how the scenario of the superconductor-to-normal transition, i.e., quantum-size cascades of jumps in the order parameter as function of the magnetic field, depends on the confining geometry and on the multiple-subband structure induced by quantum confinement. Then we investigate thermally-activated smoothing of the cascades. In Sec. 4.3 the spin-magnetic-field interaction is included and we briefly discuss the spin-generalized BdG equations for a hollow nanocylinder. Based on this generalization, we investigate how including the spin-magnetic-field interaction influences our results discussed in previous section. By switching-off the potential energy associated with the orbital-magnetic moments, we further consider the paramagnetic breakdown of superconductivity in the presence of quantization of the perpendicular electron motion. Effects of quantum confinement on the paramagnetic limiting field, including its quantum-size oscillations, are discussed here. Our conclusions and important discussions on impacts of surface roughness and fluctuations are given in Sec. 4.5.

4.2 ORBITAL-MAGNETIC MOMENTS AND QUANTUM-SIZE CASCADES

4.2.1 Formalism

Previously, we showed that the effect of a parallel magnetic field on the electron orbital motion in cylindrical superconducting nanowires results in an intriguing scenario of a superconductor-to-normal transition at zero temperature, i.e., quantum cascades [23]. Here we generalize our previous study to the case of a metallic hollow nanocylinder in a parallel magnetic field, and we investigate how the confining geometry (by changing the cylinder radius R and its wall thickness d) influences these quantum-size cascades. Effects of quantum confinement are pronounced at low temperatures and, therefore, we expect thermal smoothing of the cascades which will also be studied in the present section. For the moment we neglect spin-magnetic-field interaction and related paramagnetic effects. Their contribution will be investigated in the next section.

4.2.1.1 Bogoliubov-de Gennes equations In the clean limit, the single-electron Hamiltonian in the BdG Eqs. (1.45) reads $H_e = \frac{1}{2m_e}(-i\hbar\nabla - \frac{e}{c}\mathbf{A})^2 - \mu$, with m_e the electron band mass (which we put equal to the free electron mass) and μ the chemical potential. On the other hand, the summation in the self-consistent condition Eq. (1.62) is over the states with $|\xi_\nu| < \hbar\omega_D$, where ω_D is the Debye frequency and ξ_ν is the single-electron energy given by

$$\xi_\nu = \int \mathrm{d}^3 r \left[u_\nu^*(\mathbf{r}) H_e^{(0)} u_\nu(\mathbf{r}) + v_\nu^*(\mathbf{r}) H_e^{(0)} v_\nu(\mathbf{r})\right], \tag{4.1}$$

where $H_e^{(0)} = H_e|_{\mathbf{A}=0}$. Use of H_e instead of $H_e^{(0)}$ in Eq. (4.1) will produce practically the same results but it is much less convenient for analytical calculations. It is also of importance to note that the usual choice of only positive quasiparticle energies is not relevant in the presence of depairing due to a magnetic field (or due to an imposed supercurrent). It is well-known that in the absence of a magnetic field or a superfluid motion, the system contains only the quasiparticles with positive energies. To take account of the depairing reconstruction in the system, one should limit the states to those with positive quasiparticle energy in the limit $\mathbf{A} \to 0$, i.e., this implies that the physical solution satisfies

$$E_\nu\big|_{\mathbf{A}\to 0} > 0. \tag{4.2}$$

In the absence of a magnetic field this criterion recovers the ordinary choice of the positive quasiparticle energies.

Due to the grand-canonical formulation of the BdG equations, it is convenient to measure all the relevant energies in the problem with respect to μ. Given the mean electron density n_e, the chemical potential μ is calculated

from

$$n_e = \frac{2}{V}\sum_{\nu}\int \mathrm{d}^3 r\,\left[f_\nu |u_\nu(\mathbf{r})|^2 + (1-f_\nu)|v_\nu(\mathbf{r})|^2\right], \tag{4.3}$$

with V the system volume. For elemental superconductors, like, e.g., aluminum, the pairing energy is typically much smaller than the Fermi energy E_F. Hence, changes in the chemical potential due to the superconducting order/temperature are not important when solving Eq. (4.3) and, therefore, we set temperature to zero and neglect the superconducting order in Eq. (4.3). This gives $\mu = E_F$ in a numerical solution of the BdG equations. It is necessary to note that to obtain the correct period for the quantum-size superconducting oscillations in nanoscale systems with a simplified parabolic-band approximation (based on the band mass m_e), one should use an effective Fermi level rather than the real one (see the discussion in the second paper of [24, 25]). In general, the effective Fermi level depends on the complicated interplay between the crystalline and confinement directions, and its possible values for elemental superconductors (when ignoring the shift-up in E_F for extremely small d) can be found in [98]. For aluminum $E_F = 0.9$ eV is justified from a good agreement with experimental data on aluminum superconducting nanowires. [26]

4.2.1.2 Anderson's approximation Even for a broken time-reversal symmetry it was shown [23] that Anderson's approximation provides still very good results for a cylindrical superconducting nanowire in a parallel magnetic field, because the single-electron wave functions are the same in linear order in the vector potential $\mathbf{A}$. The same holds for a hollow nanocylinder and, so, below we use Anderson's approach. When working with the BdG equations, Anderson's approximation means that we seek for a solution of the BdG equations when the particle-like $u_n(\mathbf{r})$ and hole-like $v_n(\mathbf{r})$ amplitudes are proportional to the corresponding single-electron wave function, i.e., (ρ, φ, z are the cylindrical coordinates)

$$\begin{aligned} u_\nu(\mathbf{r}) &= \mathcal{U}_{jmk}\,\psi_{jm}(\rho)\tfrac{e^{im\varphi}}{\sqrt{2\pi}}\tfrac{e^{ikz}}{\sqrt{L}}, \\ v_\nu(\mathbf{r}) &= \mathcal{V}_{jmk}\,\psi_{jm}(\rho)\tfrac{e^{im\varphi}}{\sqrt{2\pi}}\tfrac{e^{ikz}}{\sqrt{L}}, \end{aligned} \tag{4.4}$$

with $\nu = \{j, m, k\}$, with $j = 0, 1, 2, \ldots$ the radial quantum number, $m = 0, \pm1, \pm2, \ldots$ the azimuthal quantum number, and k the wave vector of the quasi-free electron motion in the z-direction (periodic boundary conditions are applied in this direction with a unit cell of length $L = 50\,\mu$m). Diamagnetic contributions to $\mathbf{A}$ can be entirely ignored in the case of interest, which makes it possible to consider the system in a uniform external magnetic field. In our case of a parallel magnetic field $\mathbf{H} = (0, 0, H_{||})$ it is convenient to adopt the Coulomb gauge, i.e., $\mathbf{A} = \frac{H_{||}\rho}{2}\mathbf{e}_\varphi$, with $\mathbf{e}_\varphi$ the unit vector in the azimuthal direction. This allows us to choose $u_\nu(\mathbf{r})$ and $v_\nu(\mathbf{r})$ in the factorized form of Eq. (4.4).

The problem can be further simplified due to a negligible role of the term $\propto \mathbf{A}^2$ in the single-electron Hamiltonian that reads $\frac{1}{8}m_e\Omega^2\rho^2$, with $\Omega = |e|H_{||}/m_e c$. In particular, for a nanowire with a diameter of about 10 nm the critical (depairing) magnetic field $H_{c,||}$ is about $1-3$ T, see [23]. For this case $\frac{1}{8}m_e\Omega^2\rho^2 \lesssim 10^{-4}\,\text{meV} \ll \Delta_{\text{bulk}} = 0.25\,\text{meV}$. We also note that the corresponding magnetic length is $a_H = \sqrt{\hbar/m_e\Omega} \approx 25\,\text{nm}$, which is significantly larger than the radius of 5 nm. Then, when keeping only terms linear in $\mathbf{A}$, $\psi_{jm}(\rho)$ remains the same as in the absence of a magnetic field. This is why considering only pairing of time-reversed states is still a very good approximation. Hence, ψ_{jm} is obtained from the solution of the second-order differential equation

$$\xi_{jmk}\psi_{jm}(\rho) = \frac{\hbar^2}{2m_e}\big[-\frac{1}{\rho}\frac{\partial}{\partial\rho}\rho\frac{\partial}{\partial\rho} + \frac{m^2}{\rho^2} + k^2 - \mu\big]\psi_{jm}(\rho). \tag{4.5}$$

The radial part of the single-electron wave function $\psi_{jm}(\rho)$ can be expressed (see, e.g., [97]) in terms of the Bessel functions of the first and second kind with two coefficients for each set of quantum numbers $(j,\, m)$. These two coefficients together with the relevant single-electron energy ξ_{jmk} can be obtained by inserting the expression of $\psi_{jm}(\rho)$ into the following quantum-confinement boundary conditions

$$\psi_{jm}(R) = \psi_{jm}(R+d) = 0. \tag{4.6}$$

Using these energies and based on Eqs. (4.4) and (4.5), from the BdG equations we can obtain ($\mathcal{U}_{jmk}, \mathcal{V}_{jmk}$ and Δ_{jm} are real)

$$E_{jmk}\mathcal{U}_{jmk} = \xi^{+}_{jmk}\mathcal{U}_{jmk} + \Delta_{jm}\mathcal{V}_{jmk}, \tag{4.7}$$

$$E_{jmk}\mathcal{V}_{jmk} = \Delta_{jm}\mathcal{U}_{jmk} - \xi^{-}_{jmk}\mathcal{V}_{jmk}, \tag{4.8}$$

where (μ_B is the Bohr magneton)

$$\xi^{\pm}_{jmk} = \xi_{jmk} \pm m\mu_B H_{||}, \tag{4.9}$$

and the subband-dependent pairing potential $\Delta_{jm} = \Delta_{j,-m}$ is of the form

$$\Delta_{jm} = \int_R^{R+d} \mathrm{d}\rho\, \rho\, \Delta(\rho)\psi^2_{jm}(\rho), \tag{4.10}$$

with $\Delta(\rho) = \Delta^*(\rho)$. The nontrivial physical solution of the above equations is given by

$$E_{jmk} = \sqrt{\xi^2_{jmk} + \Delta^2_{jm}} + m\mu_B H_{||}, \tag{4.11}$$

where the "+" sign in front of the square root is taken by virtue of Eq. (4.2). Use of Eqs. (4.8) and (4.11) together with the usual constraint [35] $\mathcal{U}^2_{jmk} +$

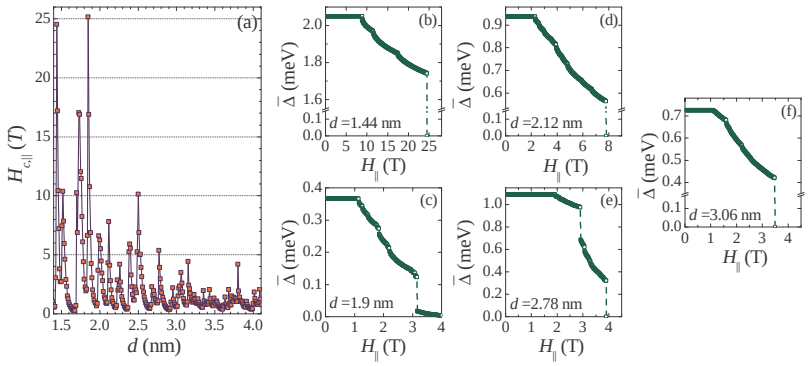

Fig. 4.1 (Color online) Hollow aluminum nanocylinder in a parallel magnetic field for $R = 0.1$ nm at zero temperature (neglecting the spin-magnetic-field interaction): (a) the critical magnetic field $H_{c,||}$ as function of the nanocylinder wall thickness d; (b)-(f) quantum-size cascades in the spatially averaged order parameter $\bar{\Delta}$ as function of $H_{||}$ for $d = 1.7$, 2.12, 2.78, 3.06 and 3.81 nm, respectively.

$\mathcal{V}_{jmk}^2 = 1$, makes it possible to express $\mathcal{U}_{jmk}$ and $\mathcal{V}_{jmk}$ in terms of ξ_{jmk} and Δ_{jm} and, then, to rewrite the expression of the order parameter Eq. (1.62) in the form of the BCS-like self-consistent equation

$$\Delta_{j'm'} = -\sum_{jmk} J_{j'm',jm} \frac{\Delta_{jm}}{2\sqrt{\xi_{jmk}^2 + \Delta_{jm}^2}} \big(1 - 2f_{jmk}\big), \tag{4.12}$$

with the pair-interaction matrix element given by

$$J_{j'm',jm} = -\frac{g}{2\pi L} \int_R^{R+d} \mathrm{d}\rho\, \rho\, \psi_{j'm'}^2(\rho)\psi_{jm}^2(\rho). \tag{4.13}$$

Here it is worth noting that, due to Eq. (4.1), we should make the summation in Eq. (4.12) over the states with $|\xi_{jmk}| < \hbar\omega_D$. This is similar to the well-known regularization procedure for ultraviolet divergence in the bulk gap equation (see, for instance, [67]). Based on a numerical solution of Eq. (4.12), one can simply calculate the position-dependent order parameter from

$$\Delta(\rho) = \frac{g}{4\pi L} \sum_{jmk} \psi_{jm}^2(\rho) \frac{\Delta_{jm}}{\sqrt{\xi_{jmk}^2 + \Delta_{jm}^2}} \big(1 - 2f_{jmk}\big), \tag{4.14}$$

which follows from the self-consistent condition and (4.4).

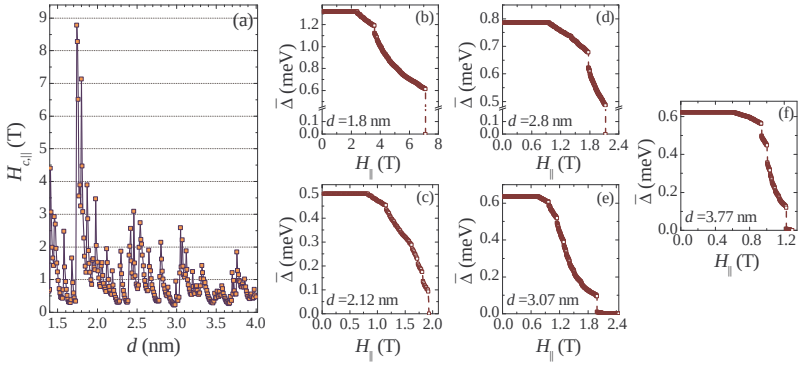

Fig. 4.2 (Color online) The same as Fig. 4.1 but for $R = 1\,\mathrm{nm}$. Panels (b)-(f) show results for $d = 1.8$, 2.12, 2.8, 3.07 and 3.77 nm, respectively.

4.2.2 Effect of the confining geometry

In our calculation, we consider aluminum as the material of the hollow nanocylinder: $\hbar\omega_D/k_B = 375\,\mathrm{K}$ with k_B the Boltzmann constant, $gN(0) = 0.18$ with $N(0)$ the bulk DOS at the effective Fermi level chosen as $E_F = 0.9\,\mathrm{eV}$ [see discussion after Eq. (4.3)].

We start our discussion by considering the impact of the confining geometry on the scenario of the superconductor-to-normal transition at zero temperature. The critical field $H_{c,||}$ is set in our numerical study as the magnetic field at which the spatially averaged order parameter, i.e.

$$\bar{\Delta} = \frac{2}{d(2R+d)} \int_R^{R+d} \mathrm{d}\rho\, \rho\Delta(\rho), \tag{4.15}$$

drops below $0.01\Delta_{\mathrm{bulk}}$, where $\Delta_{\mathrm{bulk}} = 0.25\,\mathrm{meV}$ for the parameters in use. Our previous investigation [23] of the critical magnetic field in cylindrical nanowires demonstrated that the superconductor-to-normal transition in high-quality metallic nanowires with diameters less than $10 - 15\,\mathrm{nm}$ occurs as a cascade of jumps in the order parameter as a function of the parallel magnetic field. Another finding of [23] is that the scenario of the superconductor-to-normal transition in sufficiently narrow nanowires is very different from both the first-order transition in bulk for type-I superconductors (we ignore the formation of vortices in nanowires) and the smooth crossover in superconducting wires with diameters [8, 16, 65] $20 - 200\,\mathrm{nm}$ (such a crossover is typical of mesoscopic samples, see [35] and [99]). As follows from results of [23], $H_{c,||}$ is significantly enhanced as compared to the bulk value $H_{c,\mathrm{bulk}} = 0.01\,\mathrm{T}$ (see the textbook [35]) and exhibits pronounced quantum-size oscillations.

Based on a numerical solution of the BdG equations for a hollow nanocylinder in the presence of a parallel magnetic field, we find an even more complex scenario for the superconductor-to-normal transition due to new details depending on the ratio R/d. In Fig. 4.1(a) the critical (depairing) magnetic field $H_{c,||}$ is shown as function of d for $R = 0.1\,\mathrm{nm}$ and $d = 1.4 - 4.0\,\mathrm{nm}$ (this choice represents the nanowire-like regime with $R/d \ll 1$). The results of Fig. 4.1(a) can be compared with those of Fig. 4.2(a) ($H_{c,||}$ as function of d for $R = 1.0\,\mathrm{nm}$ and $d = 1.4 - 4.0\,\mathrm{nm}$) and Fig. 4.3(a) ($H_{c,||}$ versus d for $R = 8.0\,\mathrm{nm}$ and $d = 1.4 - 4.0\,\mathrm{nm}$, the nanofilm-like regime with $R/d \gg 1$). To show details about quantum-size cascades we plot the magnetic-field dependence of the spatially averaged order parameter $\bar{\Delta}$ for different values of R and d in panels (b)-(f) of Figs. 4.1, 4.2 and 4.3. Note that the choice of $R = 0.1\,\mathrm{nm}$ for the nanowire-like regime can hardly be realized in practice. This choice is not crucial and is only an illustration for the nanowire-like regime: our results practically do not change with R for $R < 0.1 - 0.3\,\mathrm{nm}$ and, so, we are at the limit $R \to 0$.

4.2.2.1 Quantum-size oscillations of the critical parallel magnetic field From Fig. 4.1(a), we can see that the critical magnetic field can reach values as high as $20 - 25\,\mathrm{T}$ for resonant points located around $d = 1.5\,\mathrm{nm}$. This is by three orders of magnitude larger than $H_{c,\mathrm{bulk}} = 0.01\,\mathrm{T}$ and an order of magnitude higher than the estimate $H_{c,||}^{(GL)} = 4\lambda H_{c,\mathrm{bulk}}/(R+d)$ based on the result of the Ginzburg-Landau theory for a cylinder with diameter $2(R+d)$ (see [100], with $\lambda \approx 50\,\mathrm{nm}$ for aluminum in the clean limit). Beyond the superconducting resonances, $H_{c,||}$ falls down to $0.5 - 2\,\mathrm{T}$, which is close to $H_{c,||}^{(GL)}$ (the same was found in our previous paper for cylindrical superconducting nanowires [23]).

What is the reason for such pronounced oscillations of $H_{c,||}$? This is due to a systematic shift-down of the single-electron energies with increasing R and d. Due to this shift the bottoms of the single-electron subbands cross one by one the Fermi surface, which results in quantum-size superconducting oscillations with pronounced resonant enhancements each time when the bottom of a new subband approaches the Fermi surface. Since the seminal paper by Blatt and Thompson [20] (see, also, [24–26, 56, 94]) it is known that when the bottom of a single-electron subband forming due to quantization of the perpendicular electron motion is situated in the vicinity of the Fermi level, the superconducting quantities are enhanced due to an increase in the relevant DOS. Hence, the pair-condensation energy increases at resonant points and so does the critical magnetic field. In particular, as seen from Fig. 4.1(b) $\bar{\Delta}$ is about $2.05\,\mathrm{meV}$ (at $H_{||} = 0$) at the resonant point $d = 1.44\,\mathrm{nm}$, where $H_{c,||} \approx 24.5\,\mathrm{T}$. Beyond this resonance, say, at $d = 1.4\,\mathrm{nm}$, the spatially averaged order parameter falls down to $\approx \Delta_{\mathrm{bulk}}$, i.e., by an order of magnitude, and the corresponding critical field is also down by a factor of 30, i.e., to $0.7\,\mathrm{T}$. We stress that there is no simple relation like $H_{c,||}/H_{c,\mathrm{bulk}} \propto \bar{\Delta}|_{H_{||}=0}/\Delta_{\mathrm{bulk}}$, as can be seen from Figs. 4.1(b)-(f). The reason is that $H_{c,||}$ is not simply determined by the value

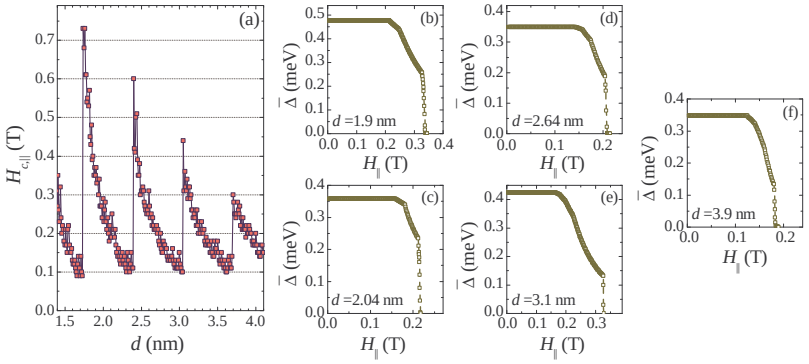

Fig. 4.3 (Color online) The same as in Figs. 4.1 and 4.2 but for $R = 8\,\mathrm{nm}$. Panels (b)-(f) represent $d = 1.9$, 2.04, 2.64, 3.1 and 3.9 nm, respectively.

of $\bar{\Delta}$ at $H_{||} = 0$. It also depends on the orbital-magnetic moments of those states that make major contributions to the superconducting characteristics. The smaller the absolute value of the relevant azimuthal quantum numbers, the larger the critical magnetic field. In Fig. 4.2(a) ($R = 1\,\mathrm{nm}$) the maximal critical magnetic field is about 9 T at $d = 1.75\,\mathrm{nm}$, while for $R = 8\,\mathrm{nm}$ [see Fig. 4.3(a)] the maximum of $H_{c,||}$ is about 0.75 T at $d = 1.75\,\mathrm{nm}$. As seen, $H_{c,||}$ exhibits an overall decrease with increasing R and d. The reason for this is two-fold. First, the resonant enhancements of $\bar{\Delta}$ are significantly reduced for larger R and d (the superconducting resonances are eventually washed out for large enough R and d, see, for more details, [26] and [98]). Second, a contribution of subbands with large azimuthal quantum numbers ($|m| \gg 1$) increases with R and d. Such a contribution is less stable with increasing $H_{||}$ due to the term $m\mu_B H_{||}$ next to the square root in the quasiparticle energy.

Comparing Figs. 4.1(a), 4.2(a) and 4.3(a), one finds a qualitative change in the character of the quantum-size oscillations in $H_{c,||}$. From our study of a hollow nanocylinder in the absence of a magnetic field, we learned that there are two distinctive regimes of the quantum-size oscillations in $\bar{\Delta}$ as function of d: (i) an almost chaotic sequence of peaks for $R/d \ll 1$, i.e., the nanowire-like behavior, and (ii) regular oscillations with an overall decrease (when increasing d) of the magnitude of resonant enhancement for $R/d \gg 1$, i.e., the nanofilm-like regime. We observe a similar picture for the critical magnetic field: irregular oscillations in Figs. 4.1(a) that change into an almost regular sequence of enhancements of $H_{c,||}$ with period $\Delta d = \lambda_F/2 \approx 0.7\,\mathrm{nm}$ (λ_F is the Fermi wavelength) when $R/d \gg 1$. Switching between these two regimes is governed by the centrifugal energy $\frac{\hbar^2}{2m_e}\frac{m^2}{\rho^2}$, see Eq. (4.5). The role of the centrifugal energy is more important for small R. In this case the difference in energy between the bottoms of two neighboring single-electron subbands strongly oscillates with changing the relevant quantum numbers. This leads

to an irregular coming-in of superconducting resonances and, as a result, to irregular oscillations of $H_{c,||}$ (and $\bar{\Delta}$) with d, as seen in Fig. 4.1(a). Unlike $R \to 0$, the centrifugal energy becomes infinitesimally small for $R \to \infty$. So, for sufficiently large R (and d) the single-electron spectrum is almost reduced to $\frac{\hbar^2}{2m_e}\frac{\pi^2(j+1)}{d^2}$ (i.e., it is nearly degenerate with respect to m) and one can recover the regular nanofilm-like appearance of the superconducting resonances with the above mentioned period $\Delta d = \lambda_F/2$. It is worth noting that the nanowire-like and nanofilm-like regimes coexist at $R = 1\,\mathrm{nm}$ as seen from Fig. 4.2(a). In particular, for $d = 1.5 - 2.0\,\mathrm{nm}$ ($R/d \sim 1$) the overall behavior of $H_{c,||}$ in Fig. 4.2(a) resembles that of Fig. 4.3(a). This is also seen from the fact that the maximum of $H_{c,||}$ in both figures is at $d = 1.75\,\mathrm{nm}$. However, the pattern of the oscillations in Fig. 4.2(a) is still more complex as compared to Fig. 4.3(a) due to many smaller resonant enhancements that are nearly washed out at $R = 8\,\mathrm{nm}$. It is interesting that a similarity between Figs. 4.2(a) and 4.3(a) are still visible even for $d = 3.5 - 4.0\,\mathrm{nm}$ (i.e., at $R/d = 0.2 - 0.3$ at $R = 1.0\,\mathrm{nm}$).

4.2.2.2 Quantum-size cascades in the order parameter Due to the quantization of the perpendicular motion of electrons, the conduction band in nanowires splits up into a series of subbands. The formation of multiple subbands results in the appearance of different quasiparticle branches. Any quasiparticle branch corresponds to the single-electron states with the same orbital-magnetic moment. Orbital-magnetic moments acquire a potential energy in the presence of a magnetic field, which results in a magnetic-field-dependent shift of the quasiparticle energy. A jump in the order parameter as function of the magnetic field can arise when one of the relevant quasiparticle branches touches zero. From this point on, such a branch supplies the system with the states with a negative quasiparticle energy. For these quasiparticles $f_{jmk} = 1$ at $T = 0$ and, as seen from Eq. (1.62), they survive even at zero temperature. It means that we face a reconstruction of the ground state which is nothing more then a signature of depairing in the corresponding subband. In order that a jump (accompanied by the hysteretic behavior) appears, such a subband should make a significant contribution to the order parameter (as seen in the following paragraph, more than $\approx 10\%$ at $H_{||} = 0$). For a smaller contribution, a smooth decrease accompanied by a kink arises in $\bar{\Delta}$ as function of $H_{||}$. Due to the multiple-subband structure, depairing induced by a magnetic field does not occur at the same time in all single-electron subbands. It first takes place in subbands that are most sensitive to a magnetic field, i.e, the subbands with large orbital magnetic moment (large modulus of the azimuthal quantum number). This results in a cascade of jumps (and kinks). However, the number of relevant single-electron subbands increases with the diameter and a relative contribution of any single-electron subband into the superconducting quantities becomes smaller and smaller. This is why the

cascade structure in superconducting nanowires is washed out for diameters $> 15 - 20\,\mathrm{nm}$.

Now let us discuss results given in panels (b)-(g) of Fig. 4.1, where $\bar{\Delta}$ is shown versus $H_{||}$ for $R = 0.1\,\mathrm{nm}$ and different values of d. Similarly to the case of a cylindrical nanowire, we observe clear signatures of the formation of a cascade of jumps in $\bar{\Delta}$ as function of $H_{||}$ for the hollow nanocylinder. In particular, as seen from Fig. 4.1(b), for $R = 0.1\,\mathrm{nm}$ and $d = 1.44\,\mathrm{nm}$ we obtain a cascade of four jumps in the dependence of $\bar{\Delta}$ on $H_{||}$. The first, second and third jumps are rather small (they appear like kinks in the figure). However, the fourth jump is pronounced: $\bar{\Delta}$ drops from $\approx 1.7\,\mathrm{meV}$ down to zero. The first jump is related to the onset of depairing in the subband $(j, m) = (0, -4)$. It is small because the contribution of this subband to $\bar{\Delta}$ (at $H_{||} = 0$) is only about 4.5%. We note that before depairing starts in subband $(j, m) = (0, -4)$, $\bar{\Delta}$ does not exhibit any change with $H_{||}$: all quasiparticle energies are positive, $f_{jmk} = 0$ for all relevant quantum numbers and, as a result, the order parameter does not depend on $H_{||}$. The second and third small jumps in panel (b) mark the onsets of depairing in subbands $(j, m) = (0, -3)$ (contribution of about 6% at $H_{||} = 0$) and $(j, m) = (0, -2)$ (contribution $\approx 5\%$ at $H_{||} = 0$), respectively. The eventual drop to zero measures $H_{c,||} \approx 24\,\mathrm{T}$ and occurs when the bottom of the quasiparticle branch associated with subband $(j, m) = (1, -2)$ touches zero. This is one of the resonant subbands [together with $(j, m) = (1, 2)$] and its contribution to $\bar{\Delta}$ is about 30% at $H_{||} = 0$ and approaches 40% in the vicinity of $H_{c,||}$ [the growth is due to the depairing in subbands $(j, m) = (0, -2)$ and $(j, m) = (0, -3)$]. The question can arise why the third and fourth jumps in $\bar{\Delta}$ at $d = 1.44\,\mathrm{nm}$ [see Fig. 4.1(a)] are situated at different magnetic fields in spite of the fact that there are the same azimuthal quantum numbers for the associated quasiparticle branches $(j, m) = (0, -2)$ and $(1, -2)$. The point is that the subband-dependent order parameters Δ_{jm}'s are generally different due to the Andreev mechanism in nanoscale superconductors (for more detail, see [22, 68, 97]) and in the case of interest we have $\Delta_{0,-2} < \Delta_{1,-2}$. Our previous study of magnetically induced quantum cascades in superconducting cylindrical nanowires [23] and our present investigation of a hollow nanocylinder for $R \to 0\,(R = 0.1\,\mathrm{nm})$ show that it is almost a typical situation when the onset of depairing in a resonant subband "kills" the superconducting solution and, hence, marks the critical field $H_{c,||}$ [see panels (b), (d), and (f) of Fig. 4.1 for the resonant points $d = 1.44$, 2.12 and 3.06 nm, respectively]. Note that the cascade pattern is changed in the presence of many resonant subbands, as can be seen from Fig. 4.1(e), $d = 2.78\,\mathrm{nm}$. For this resonant thickness there are four resonant subbands with $(j, |m|) = (1, 5)$ (a contribution of about 23% in $\bar{\Delta}$ at $H_{||} = 0$) and $(0, 5)$ (16%). Two of them, with $(j, m) = (1, -5)$ and $(0, -5)$, are responsible for two jumps of about $0.2 - 0.25\,\mathrm{meV}$ in $\bar{\Delta}$.

We also remark that unlike the resonant points, the scenario of the magnetically induced breakdown of superconductivity outside superconducting resonances exhibits, as a rule, a pronounced jump down with a subsequent

tail of $\bar{\Delta}$ slowly approaching zero with increasing $H_{||}$, see, e.g., Fig. 4.1(c). Why is there a pronounced jump in $\bar{\Delta}$ as function of $H_{||}$ which is still visible for non-resonant conditions in spite of the fact that there are no resonant subbands? Let us consider what happens during the decay of a superconducting resonance with increasing d. The bottom of a resonant subband moves down in energy and leaves the Debye window $|\xi_{jmk}| < \hbar\omega_D$. As a result, DOS at the Fermi level is reduced and a resonant enhancement disappears. However, the contribution of the former resonant subband(s) into $\bar{\Delta}$ remains larger as compared to other single-electron subbands. For instance, a large jump in $\bar{\Delta}$ in Fig. 4.1(c) measures the onset of depairing in the single-electron subband $(j, m) = (2, -1)$, whose contribution to $\bar{\Delta}$ is of about 13% at $H_{||} = 0$, which appears to be sufficient in order to lead to a significant jump in $\bar{\Delta}$ but it is not sufficient to "kill" the superconducting solution without a remaining after-jump tail. Such a tail is not an artifact of our numerical calculations. In particular, the after-jump tail in Fig. 4.1(c) was self-consistently calculated to within an accuracy of about 10^{-6} meV.

When switching from the nanowire-like regime to the nanofilm-like behavior by increasing the ratio R/d, see Figs. 4.2(b)-(f) and 4.3(b)-(f), we find significantly smaller jumps in $\bar{\Delta}$ as function of $H_{||}$. In particular, Figs. 4.2(b)-(f) show patterns of the superconductor-to-normal transition for $R = 1.0$ nm for the five resonant thicknesses $d = 1.8$, 2.12, 2.8, 3.07 and 3.77 nm, respectively. It is instructive to compare these patterns with those of Figs. 4.1(b),(d)-(f) [results for the non-resonant thickness $d = 1.9$ nm are given in Fig. 4.1(c)]. As seen, the quantum-size cascades are still well pronounced but jumps become smaller for $R = 1.0$ nm (and the numbers of the jumps increases). In addition, there are clear signatures of after-jump tales in $\bar{\Delta}$ in panels (e) and (f) of Fig. 4.2. This is similar to the non-resonant picture shown in Fig. 4.1(c). The reason for all the features mentioned above is a rise in the number of relevant subbands that make a contribution to the superconducting order parameter (i.e., entering the Debye window). The larger R, the smaller the centrifugal energy in Eq. (4.5), which results in a decrease of the interband energy spacing. So, more and more single-electron subbands come in play and the role of any particular subband diminishes. For instance, the typical eventual drop to zero in $\bar{\Delta}$ at $H_{||} = H_{c,||}$ present in most cases in Fig. 4.1 and 4.2 breaks into a chain of almost insignificant jumps in Figs. 4.3(b)-(f), notwithstanding whether d is close to a superconducting resonance [as $d = 3.1$ nm in Fig. 4.3(e)] or not [as $d = 1.9$, 2.04, 2.64 and 3.9 nm shown in Fig. 4.3(b), (c), (d) and (f), respectively]. Further increase in R/d leads to a smoothing of the jumps together with the accompanying cascade structure. Here it is worth noting that the microscopic basis of the resonant enhancement for large R/d is different as compare to those for small R/d. Indeed, for a superconducting resonance at a small ratio R/d we have, as a rule, one single-electron subband whose bottom is situated in the Debye window $|\xi_{jmk}| < \hbar\omega_D$. For large R/d the bottoms of many subbands are condensed in the vicinity of the

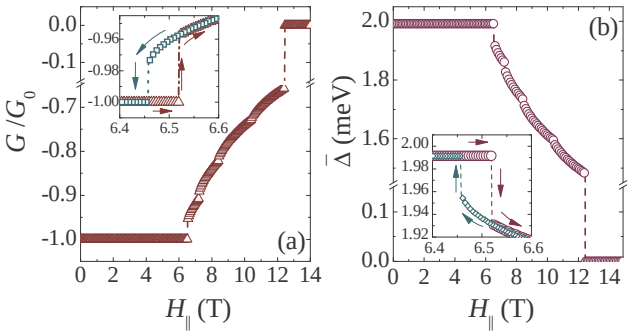

Fig. 4.4 (Color online) The Gibbs free-energy of the superconducting state (at $T = 0$) of the hollow nanocylinder for $R = 0.5$ nm and $d = 1.36$ nm as a function of the parallel magnetic field.

level $\frac{\hbar^2}{2m_e}\frac{\pi^2(j+1)}{d^2}$ due to an extremely small centrifugal energy. When such a level occurs in the Debye window, we obtain a nanofilm-like superconducting resonance. Due to the contribution of many different azimuthal numbers, the response of the system to the external parallel magnetic field is no longer as dramatic as for small R/d.

To conclude this section, we make some additional remarks on the superconductor -to-normal transition in the presence of the quantum-size cascades. In Fig. 4.4 we show the Gibbs-free energy (measured from G_0, with G_0 the Gibbs-free energy of the normal state) versus $H_{||}$, panel (a), together with the corresponding dependence of $\bar{\Delta}$ on $H_{||}$, panel (b). As seen, jumps in $\bar{\Delta}$ are accompanied by discontinuities in G/G_0 (see also clear hysteretic patterns in the inserts). It is well-known that when the thermodynamic potential acquires a discontinuity, the system loses its thermodynamic stability at this point. Thus, any jump in $\bar{\Delta}$ is an off-equilibrium transition associated with depairing in one of single-electron subbands. Even in the presence of smoothing (e.g., induced by an increase in R or d), the system can remain thermodynamically unstable in the vicinity of the point of a smoothed drop. This can significantly extend the domain, where the quantum-size cascades of jumps in the order parameter can be observed experimentally. It is similar to depairing in the presence of a uniform supercurrent in bulk. Here the supercurrent first increases with the superfluid velocity but, after reaching its maximal value, starts to decrease quickly to zero. The regime of a continuous decrease of the supercurrent with increasing superfluid velocity can not be realized experimentally because of a thermodynamic instability [101]. In practice, after reaching the maximal value of the supercurrent, the system will pass from the superconducting state to the normal one with a jump similar to our jumps in $\bar{\Delta}$ as function of $H_{||}$ (see also the recent paper about current-induced cascades [102]).

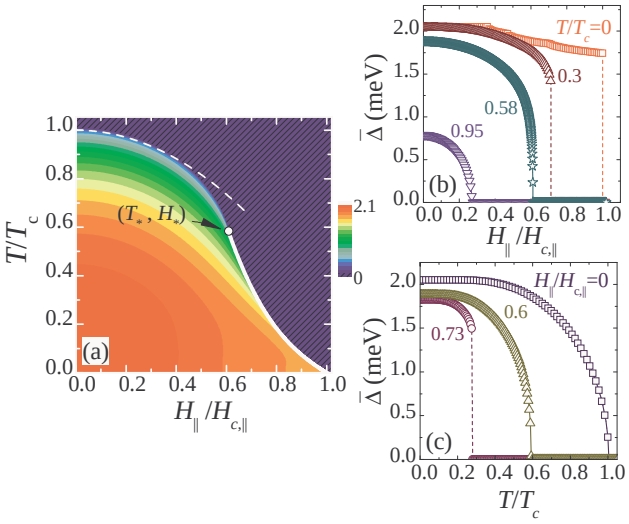

Fig. 4.5 (Color online) Effect of temperature on the quantum-size cascades for $R = 0.1\,\text{nm}$ and $d = 1.44\,\text{nm}$ (no spin-magnetic-field interaction): (a) the contour plot of the spatially averaged order parameter $\bar{\Delta}$(in meV) as function of $H_{||}/H_{c,||}$ (with $H_{c,||} = 24.5\,\text{T}$) and T/T_c (with $T_c/T_{c,\text{bulk}} = 11.4$); (b) $\bar{\Delta}$ versus $H_{||}/H_{c,||}$ for $T/T_c = 0, 0.3, 0.6$ and 0.95; (c) $\bar{\Delta}$ as dependent on T/T_c for $H_{||}/H_{c,||} = 0, 0.6$ and 0.73. The solid curve in (a) shows the position of the discontinuous jump in $\bar{\Delta}$ down to zero (ending at (T_*, H_*)). The dashed curve in (a) represents the temperature-dependent critical field $H_{c,||}(T) = 1.17H_{c,||}(1 - T/T_c)^{1/2}$.

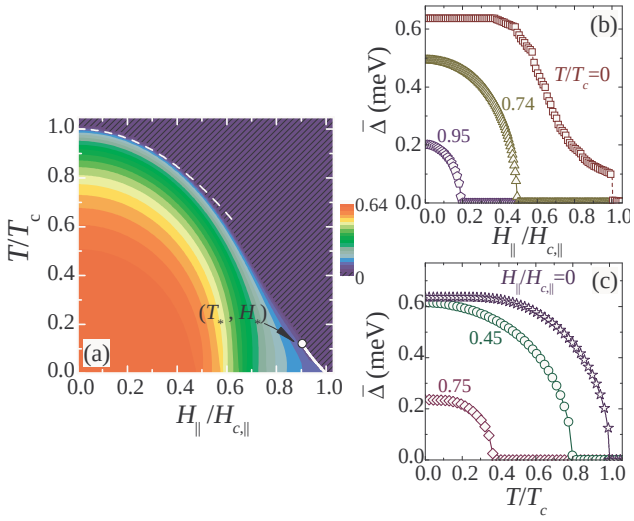

Fig. 4.6 (Color online) The same as in Fig. 4.5 but for $R = 1\,\text{nm}$ and $d = 3.07\,\text{nm}$. Panel (b) shows data for $T/T_c = 0, 0.74$, and 0.95 (with $T_c/T_{c,\text{bulk}} = 2.8\,\text{K}$), panel (c) shows results for $H_{||}/H_{c,||} = 0, 0.45$, and 0.75 (with $H_{c,||} = 1.99\,\text{T}$). Here the dashed curve corresponds to $H_{c,||}(T) = 1.02H_{c,||}(1 - T/T_c)^{1/2}$.

4.2.3 Thermal smoothing

In previous subsection, we considered how quantum-size cascades of jumps in the order parameter as function of a parallel magnetic field change with the confining geometry. In particular, it was shown that cascades becomes much less pronounced with increasing the ratio R/d. The reason is a significant increase in the number of relevant single-electron subbands and, so, a decrease of the relative contribution of each particular subband. As a result, the number of jumps in a cascade increases but jumps become smaller. Then, they are converted into kinks in the dependence of $\bar{\Delta}$ on $H_{||}$ and, finally, the kinks also disappear with a further increase in R/d.

In the present subsection we consider another variant of smoothing of the quantum-size cascades that is due to thermal effects. Switching on the temperature means that in addition to quasiparticles with negative energy, there appears a contribution to $\bar{\Delta}$ from quasiparticles with positive energy $E_{jmk} \sim k_B T$. One can expect that this will result in a smoothing of jumps but, unlike the case of increasing R/d, the number of jumps (or smoothed jumps) in a cascade will not change with temperature. In particular, Fig. 4.5 illustrates how the cascade structure of the superconductor-to-normal transition is smoothed by temperature for the nanowire-like regime $R/d \ll 1$ ($R = 0.1$ and $d = 1.44\,\text{nm}$): (a) the contour plot of $\bar{\Delta}$ as function of T/T_c

and $H_{||}/H_{c,||}$, with T_c the critical temperature at zero magnetic field; (b) $\bar{\Delta}$ as function of $H_{||}/H_{c,||}$ for $T/T_c = 0$, 0.3, 0.6, and 0.95; (c) $\bar{\Delta}$ as function of T/T_c for $H_{||}/H_{c,||} = 0$, 0.6, and 0.73. Here $T_c/T_{c,\mathrm{bulk}} = 11.5$, with $T_{c,\mathrm{bulk}} = 1.65\,\mathrm{K}$ for our parameters, and $H_{c,||} = 24.5\,\mathrm{T}$. Our numerical analysis shows that the jump of $\bar{\Delta}$ to zero (that measures the critical magnetic field as calculated at $T = 0$) survives up to $T_*/T_c = 0.58$ [see the solid curve in Fig. 4.5(a)]. Physically, we can assume that T_* is mainly determined by the magnitude of the jump in $\bar{\Delta}$ at zero temperature, i.e., $\bar{\Delta}|_{\mathrm{jump}} \approx 1.74\,\mathrm{meV}$. A naive expectation suggests that the ratio $\bar{\Delta}|_{\mathrm{jump}}/k_B T_*$ can be close to the BCS parameter 1.76, i.e., the ratio of the energy gap to the critical temperature. Interestingly, this expectation is supported by our numerical results. In Fig. 4.6 we have $\bar{\Delta}|_{\mathrm{jump}}/k_B T_* \approx 1.85$. A similar result is obtained for $R = 1.0\,\mathrm{nm}$ and $d = 3.07\,\mathrm{nm}$, see Fig. 4.7, where panel (a) shows the contour plot of $\bar{\Delta}$ as dependent on T/T_c and $H_{||}/H_{c,||}$ (here $T_c/T_{c,\mathrm{bulk}} = 2.8$ and $H_{c,||} = 1.99\,\mathrm{T}$); panel (b) represents the data for $\bar{\Delta}$ as dependent on $H_{||}/H_{c,||}$ for $T/T_c = 0$, 0.3, 0.6, and 0.95; (c) gives $\bar{\Delta}$ as function of T/T_c for $H_{||}/H_{c,||} = 0$, 0.6, and 0.73. Here $\bar{\Delta}|_{\mathrm{jump}} \approx 0.086\,\mathrm{meV}$ and $T_* = 0.12T_c$, which results in $\bar{\Delta}|_{\mathrm{jump}}/k_B T_* \approx 1.81$. Smaller jumps in the cascade are smoothed into continuous drops even below T_*. Hence, we can consider that T_* measures the temperature above which the cascade structure is almost washed out due to thermal effects. T_* strongly oscillates with changing R and d and exhibits an overall decrease with increasing R and d, which is similar to other superconducting characteristics. This can be seen from Fig. 4.7, where our numerical results for $R = 8\,\mathrm{nm}$ and $d = 2.12\,\mathrm{nm}$ are given: (a), the contour plot of $\bar{\Delta}$; (b), the data for $\bar{\Delta}$ as function of $H_{||}/H_{c,||}$ for $T/T_c = 0$, 0.65, and 0.97 (with $H_{c,||} = 0.234\,\mathrm{T}$ and $T_c/T_{c,\mathrm{bulk}} = 1.88$); (c), $\bar{\Delta}$ versus T/T_c for $H_{||}/H_{c,||} = 0$, 0.65, and 0.9. As follows from our discussion in previous section, only small jumps survive in $\bar{\Delta}$ at such R and d. For instance, jumps of about $0.02 - 0.03\,\mathrm{meV}$ are still visible at $T = 0$ in the vicinity of $H_{||} = H_{c,||}$ in Fig. 4.7(b). They are smoothed out when reaching $T_* = 0.08T_c$. So, the ratio T_*/T_c decreases from Fig. 4.5 to Fig. 4.7 and, in addition, T_c also reduces. It is of interest to discuss the behavior of the temperature-dependent critical magnetic field $H_{c,||}(T)$ for $T \to 0$ (i.e., the temperature dependence of the position of the final drop to zero in $\bar{\Delta}$ as function of $H_{||}$). By numerically fitting, we find ($H_{c,||}(0) = H_{c,||}$)

$$H_{c,||}(T)/H_{c,||}(0) = 1 - \alpha T/T_c \quad (T \to 0), \tag{4.16}$$

with $\alpha \approx 1.53$ for $R = 0.1\,\mathrm{nm}$ and $d = 1.44\,\mathrm{nm}$. As seen, the temperature dependent contribution to $H_{c,||}(T)$ is linear in T for $T \to 0$, which has nothing to do with the temperature dependence of the thermodynamic critical field in a bulk superconductor with the leading-order temperature correction $\propto (T/T_c)^2$ (see [67]). In turn, numerical fits for $R = 1.0\,\mathrm{nm}$, $d = 3.07\,\mathrm{nm}$ and $R = 8.0\,\mathrm{nm}$, $d = 2.12\,\mathrm{nm}$ give $\alpha \approx 1.0$ and 0.73, respectively. The factor α in Eq. (4.16) decreases to zero with increasing R and d (our numerical results for other values of R and d shows that such a decrease is accompanied by

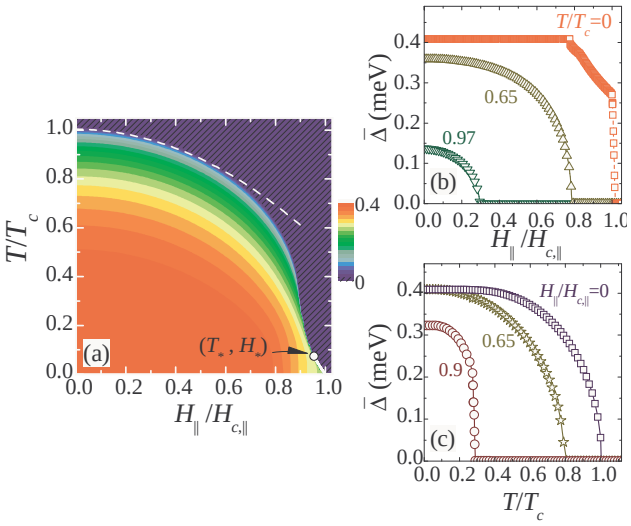

Fig. 4.7 (Color online) The same as in Fig. 4.5 but for $R = 8\,\text{nm}$ and $d = 2.12\,\text{nm}$. The dashed curve in panel (a) represents $H_{c,||}(T) = 1.43H_{c,||}(1 - T/T_c)^{1/2}$; the solid line in (a) shows the position of an abrupt decay of $\bar{\Delta}$ to zero by a cascade of jumps of about $0.02 - 0.03\,\text{meV}$. Panel (b) shows our results for $T/T_c = 0$, 0.65, and 0.97 ($T_c/T_{c,\text{bulk}} = 1.9\,\text{K}$), panel (c) displays the data for $H_{||}/H_{c,||} = 0, 0.65$, and 0.9 (with $H_{c,||} = 0.234\,\text{T}$).

size-dependent oscillations). The difference in the low-temperature behavior of $H_{c,||}(T)$ as compared to the bulk thermodynamic field is directly related to the temperature dependence of $\bar{\Delta}$ for $H_{||} > H_*$. Here, due to the presence of the large jump in $\bar{\Delta}$ as function of $H_{||}$, we obtain a similar jump in $\bar{\Delta}$ as function of T, as seen from the results for $H_{||}/H_{c,||} = 0.73$ in Fig. 4.5(c). Only for $H_{||} < H_*$ the ordinary BCS-like dependence of the order parameter on the temperature is recovered, see Fig. 4.5(c), the data for $H_{||}/H_{c,||} = 0$, 0.6, and Figs. 4.6(c) and Fig. 4.7(c).

For $T \to T_c$, $H_{c,||}(T)$ goes to zero which can be fitted to the expression

$$H_{c,||}(T)/H_{c,||}(0) = \beta(1 - T/T_c)^{1/2} \quad (T \to T_c), \tag{4.17}$$

with $\beta \approx 1.17$, 1.02 and 1.44 for the parametric sets $(R, d) = (0.1, 1.44)\,\text{nm}$, $(1.0, 3.07)\,\text{nm}$, and $(8.0, 2.12)\,\text{nm}$, respectively. Despite the regular BCS-like temperature dependence of the order parameter $\bar{\Delta} \propto (1 - T/T_c)^{1/2}$ in the domain $H_{||}/H_{c,||} \ll 1$, the critical field $H_{c,||}(T)$ again does not exhibit any similarity with the bulk thermodynamic field [the latter is proportional to $1 - T/T_c$ $(T \to T_c)$, see the textbook [67]]. The reason is that the magnetic field easily penetrates into a nanoscale superconductor, which is completely different from a bulk type-I superconductor. In the case under investigation

$H_{c,||}(T)$ is always close to $H_{||}$ at which the resonant subband (or the former resonant subband for the nonresonant case) begins to supply the system with negative-energy quasiparticles (thermal effects do not alter this trend but results in a smoothing of jumps in the cascade). So, based on Eq. (4.11), we can expect that $H_{c,||}(T) \approx \Delta_{jm}/(\mu_B m)$, where j and $m < 0$ are the quantum numbers of a subband making a major contribution to the superconducting quantities. As $\Delta_{jm} \sim \bar{\Delta} \propto (1 - T/T_c)^{1/2}$, we recover the result of Eq. (4.17). Similar to the factor α in Eq. (4.16), the factor β in Eq. (4.17) varies with R and d, as well. However, our numerical analysis does not show any signature of a systematic reduction of β. Unlike β, the factor α in Eq. (4.16) exhibits a significant overall decrease to zero with increasing R and d. It means that the low-temperature trend of Eq. (4.16) disappears together with the quantum-size cascades for large enough R and d. Equation (4.17) is still applicable until d approaches the magnetic penetration depth. From this point on we can no longer consider a homogeneous magnetic field and neglect the contribution of the diamagnetic currents.

4.3 PARAMAGNETIC EFFECTS

4.3.1 Formalism

When taking the spin-magnetic-field interaction into account, the spin-generalized BdG Eqs. (1.79) are needed and can be rewritten as follows,

$$\begin{bmatrix} H_{e,\uparrow} & \Delta & 0 & 0 \\ \Delta^* & -H^*_{e,\downarrow} & 0 & 0 \\ 0 & 0 & H_{e,\downarrow} & \Delta \\ 0 & 0 & \Delta^* & -H^*_{e,\uparrow} \end{bmatrix} \begin{bmatrix} u_{N,\uparrow} \\ v_{N,\downarrow} \\ u_{N,\downarrow} \\ -v_{N,\uparrow} \end{bmatrix} = \epsilon_N \begin{bmatrix} u_{N,\uparrow} \\ v_{N,\downarrow} \\ u_{N,\downarrow} \\ -v_{N,\uparrow} \end{bmatrix}, \tag{4.18}$$

where $N = (\nu, \sigma)$, with $\nu = \{j, m, k\}$ and $\sigma = \pm 1$ the spin-like discrete index, and the spin-dependent Hamiltonian $H_{e,\alpha}$ ($\alpha = \{\uparrow, \downarrow\}$) is given by

$$H_{e,\alpha} = \frac{1}{2m_e}(-i\hbar\nabla - \frac{e}{c}\mathbf{A})^2 + \Phi_\alpha - \mu_F, \tag{4.19}$$

with $\Phi_\uparrow = -\Phi_\downarrow = \mu_B H_{||}$. The self-consistency relation is now written in the form

$$\Delta(\mathbf{r}) = V \sum_N \left[u_{N,\uparrow}(\mathbf{r}) v^*_{N,\downarrow}(\mathbf{r})(1 - f_N) + u_{N,\downarrow}(\mathbf{r}) v^*_{N,\uparrow}(\mathbf{r}) f_N \right]. \tag{4.20}$$

Making use of Anderson's approximation, we put

$$u_{N,\alpha}(\mathbf{r}) = \tilde{u}_{N,\alpha}\, \vartheta_{jm}(\rho) \tfrac{e^{im\varphi}}{\sqrt{2\pi}} \tfrac{e^{ikz}}{\sqrt{L}}, \tag{4.21}$$

$$v_{N,\alpha}(\mathbf{r}) = \tilde{v}_{N,\alpha}\, \vartheta_{jm}(\rho) \tfrac{e^{im\varphi}}{\sqrt{2\pi}} \tfrac{e^{ikz}}{\sqrt{L}}, \tag{4.22}$$

where the factors $\tilde{u}_{N,\alpha}$ and $\tilde{v}_{N,\alpha}$ can be chosen real. Here it is necessary to note that the constraint $\tilde{u}^2_{jmk} + \tilde{v}^2_{jmk} = 1$, as used for the BdG equations in the absence of the spin-magnetic energy, is now replaced by

$$\sum_{\alpha} \left(\tilde{u}^2_{N,\alpha} + \tilde{v}^2_{N,\alpha}\right) = 1. \tag{4.23}$$

When inserting Eqs. (4.22) into Eq. (4.18), Eq. (4.18) is reduced to four linear algebraic equations that form two systems of two equations with two variables, i.e.,

$$\epsilon_N \tilde{u}_{N,\uparrow} = \left(\xi^{+}_{jmk} + \Phi_{\uparrow}\right)\tilde{u}_{N,\uparrow} + \Delta_{jm}\tilde{v}_{N,\downarrow}, \tag{4.24}$$

$$\epsilon_N \tilde{v}_{N,\downarrow} = \Delta_{jm}\tilde{u}_{N,\uparrow} - (\xi^{-}_{jmk} + \Phi_{\downarrow})\tilde{v}_{N,\downarrow}. \tag{4.25}$$

and

$$\epsilon_N \tilde{u}_{N,\downarrow} = \left(\xi^{+}_{jmk} + \Phi_{\downarrow}\right)\tilde{u}_{N,\downarrow} - \Delta_{jm}\tilde{v}_{N,\uparrow}, \tag{4.26}$$

$$\epsilon_N \tilde{v}_{N,\uparrow} = -\Delta_{jm}\tilde{u}_{N,\downarrow} - \left(\xi^{-}_{jmk} + \Phi_{\uparrow}\right)\tilde{v}_{N,\uparrow}, \tag{4.27}$$

where $\xi^{\pm}_{jmk}$ and Δ_{jm} are defined by Eqs. (4.9) and (4.10). Equations (4.24) have a nontrivial solution when $\epsilon_N = \sqrt{\xi^2_{jmk} + \Delta^2_{jm}} + (m+1)\mu_B H_{||}$ (here a sign "+" in front of the square root is taken for the physical solution, as usual). However, this quasiparticle energy is not the same as that for the nontrivial solution of Eqs. (4.27) $\epsilon_N = \sqrt{\xi^2_{jmk} + \Delta^2_{jm}} + (m-1)\mu_B H_{||}$. It means that we obtain two different excitation branches, i.e.,

$$\epsilon_{jmk,\sigma} = \sqrt{\xi^2_{jmk} + \Delta^2_{jm}} + (m+\sigma)\mu_B H_{||}, \tag{4.28}$$

where for $\sigma = 1$ we have $\tilde{u}_{N,\uparrow}, \tilde{v}_{N,\downarrow} \neq 0$ while $\tilde{u}_{N,\downarrow} = \tilde{v}_{N,\uparrow} = 0$; and for $\sigma = -1$ we obtain $\tilde{u}_{N,\uparrow} = \tilde{v}_{N,\downarrow} = 0$ and $\tilde{u}_{N,\downarrow}, \tilde{v}_{N,\uparrow} \neq 0$. Now, solving Eqs. (4.24) and (4.27) together with the constraint of Eq. (4.23) for both quasiparticle branches, we arrive at the following spin-generalized BCS-like equation:

$$\Delta_{j'm'} = -\sum_{jmk} g_{j'm',jm} \frac{\Delta_{jm}\left(1 - \sum_{\sigma} f_{jmk,\sigma}\right)}{2\sqrt{\xi^2_{jmk} + \Delta^2_{jm}}}, \tag{4.29}$$

with $g_{j'm',jm}$ given by Eq. (4.13). Following the cut-off rule of Eq. (4.1), the summation in Eq. (4.29) runs over the states with $|\xi_{jmk}| < \hbar\omega_D$. The position dependent superconducting order parameter is now of the form

$$\Delta(\rho) = \frac{g}{4\pi L} \sum_{jmk} \vartheta^2_{jm}(\rho) \frac{\Delta_{jm}\left(1 - \sum_{\sigma} f_{jmk,\sigma}\right)}{\sqrt{\xi^2_{jmk} + \Delta^2_{jm}}}. \tag{4.30}$$

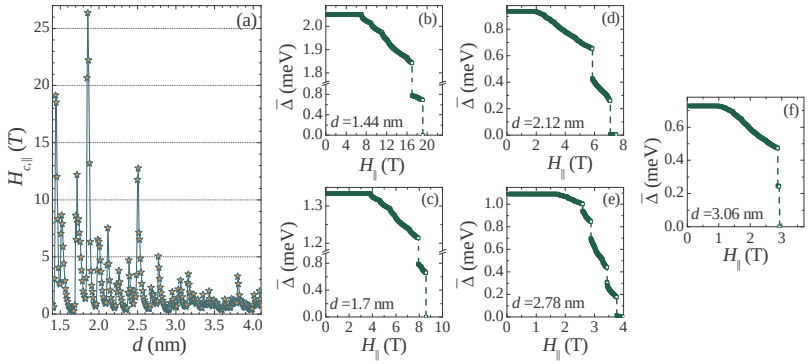

Fig. 4.8 (Color online) Including the spin-magnetic-field potential energy: (a) $H_{c,||}$ as function of d for $R = 0.1$ nm; (b)-(f) quantum-size cascades in $\bar{\Delta}$ as function of $H_{||}$ for $d = 1.7$, 2.12, 2.78, 3.06 and 3.81 nm, respectively.

4.3.2 Including the spin-magnetic-field interaction

Similar to Eq. (4.12), the magnetic field $H_{||}$ influences the solution of Eq. (4.29) only through the quasiparticle occupation number $f_{jmk,\sigma}$. It means that Δ_{jm} is not sensitive to $H_{||}$ for $f_{jmk,\sigma} = 0$, i.e., for positive quasiparticle energies at zero temperature. So, we expect that the spin-magnetic-field interaction will not qualitatively change the cascade scenario of the superconductor-to-normal transition. However, including spin magnetic moments, we obtain an extra contribution into the quasiparticle energy that splits the excitation spectrum into the two different branches. This can transform some of the jumps in the order parameter as function of $H_{||}$ into smaller jumps. Another quantitative effect of the spin-magnetic-field interaction concerns the magnitude of the critical magnetic field. When the relevant azimuthal quantum numbers are large enough (i.e., for large R and d), the spin-magnetic-field potential energy can not significantly alter $H_{c,||}$. However, for small R and d, when a major contribution to the order parameter comes from states with $|m| < 10 - 20$, one expects a persistent effect of spin magnetic moments on $H_{c,||}$.

Let us first examine the dependence of the zero-temperature critical magnetic field on d as shown in Figs. 4.8(a) [$R = 0.1$ nm] and 4.9(a) [$R = 1.0$ nm]. As was expected, qualitative patterns of the quantum-size oscillations in $H_{c,||}$ do not change when including the spin-magnetic-field interaction. In particular, we again observe the same irregular sequence of resonant enhancements of $H_{c,||}$ for the nanowire-like regime at $R = 0.1$ nm, see Fig. 4.8(a). The only difference is that $H_{c,||}$ is generally smaller by $10 - 20\%$ in the presence of the spin-magnetic-field interaction (this is clearly seen at the resonant points). However, there are a few exceptions, e.g., $H_{c,||}$ increases when the spin-magnetic-field moments are included, see, e.g., $d = 1.85$ nm. At first

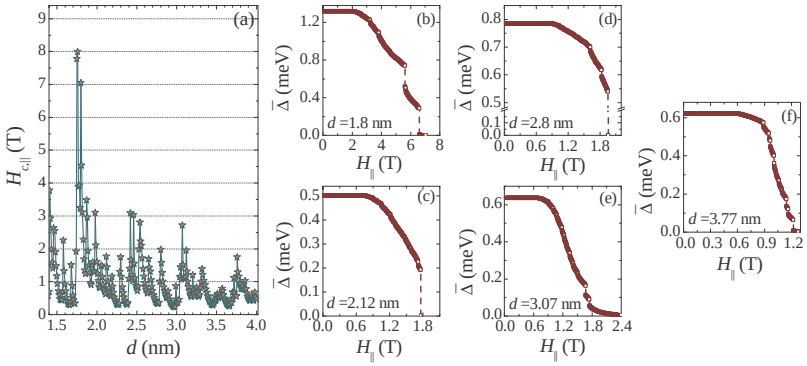

Fig. 4.9 (Color online) The same as Fig. 4.8 but for $R = 1\,\text{nm}$. Panels (b, c, d, e, f) shows results for $d = 1.8$, 2.12, 1.8, 3.07 and 3.77 nm.

sight this looks strange. However, the underlying reason is rather simple. The spin-magnetic-field interaction splits any resonant subband into two smaller subbands. This not only transform the final jump to zero in $\bar{\Delta}$ into smaller drops but, sometimes, also leads to the appearance of an after-jump tale in $\bar{\Delta}$ [see Fig. 4.1(c) and the related discussion]. If such a tale is significant, we obtain an increase in $H_{c,||}$ rather than a decrease due to the definition of $H_{c,||}$ used in the present work. Recall that $H_{c,||}$ is set in our numerical study as the magnetic field at which $\bar{\Delta}(H_{||})$ drops below $0.01\Delta_{\text{bulk}}$. The decrease in $H_{c,||}$ as induced by the spin-magnetic-field interaction is less pronounced for $R = 1.0\,\text{nm}$, see Fig. 4.9(a). Here $H_{c,||}$ almost does not exhibit any change as compared to Fig. 4.2(a) except the domain $d < 2\,\text{nm}$, where a general decrease of about $5 - 10\%$ is observed. This is quite expected because of a significant increase in the absolute value of the relevant azimuthal quantum numbers when passing from $R = 0.1\,\text{nm}$ to $R = 1.0\,\text{nm}$. Note that due to an even more significant increase in $|m|$ for $R = 8\,\text{nm}$, we did not find changes that are more than 1% in the corresponding $H_{c,||}$ as compared to our results without the spin-magnetic-field interaction.

In Figs. 4.8(b)-(f) we show how the spatially averaged order parameter $\bar{\Delta}$ depends on $H_{||}$ when including the spin-magnetic-field potential energy in the nanowire-like regime for $d = 1.44$, 1.7, 2.12, 2.78, and 3.06 nm (only resonant points are given). As discussed in the first paragraph of this subsection, including the spin-magnetic-field interaction not only reduces, as a rule, $H_{c,||}$ but also breaks jumps in $\bar{\Delta}$ into smaller jumps. This is clearly the case, as seen from the comparison of our results in Fig. 4.8 with those in Fig. 4.1. For instance, in Fig. 4.8(b) the order parameter decays through 2 large jumps while in Fig. 4.1(b) only one significant jump appears. In Fig. 4.1(e) there are two pronounced jumps in $\bar{\Delta}$ as function of $H_{||}$ (here two single-electron subbands with $(j, m) = (0, -5)$ and $(1, -5)$ are responsible for the decay of

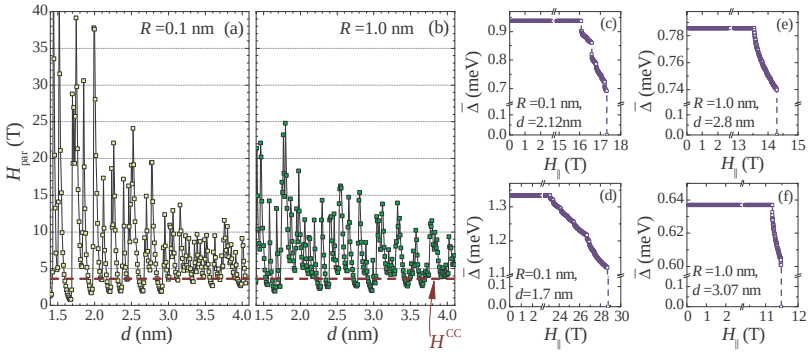

Fig. 4.10 (Color online) Paramagnetic breakdown of superconductivity: (a) and (b) quantum-size oscillations of the paramagnetic limiting field $H_{\rm par}$ as function of d (the dashed line represents the Clogston-Chandrasekhar bulk field H^{CC}); (b)-(f) the spatially averaged order parameter $\bar{\Delta}$ versus $H_{||}$ (in the presence of only spin-magnetic-field interaction) for $(R, d) = (0.1, 2.12)$ nm, $(0.1, 1.7)$ nm, $(1.0, 2.8)$ nm, and $(1.0, 3.07)$ nm, respectively.

$\bar{\Delta}$). So, it is natural to expect that these two jumps are replaced by 4 smaller jumps in the presence of the spin-magnetic-field interaction, see Fig. 4.8(e). It is interesting that such a trend of doubling the number of jumps is not fully supported by the results given in Figs. 4.9(b)-(f), where $\bar{\Delta}$ as function of $H_{||}$ is shown for the resonant thicknesses $d = 1.8$, 2.12, 2.8, 3.07, and 3.77 nm. Notice that there are also examples [see panels (c) and (d)] when including the spin magnetic moments, contrary to expectation based on Figs. 4.8(b)-(f), results in the appearance of a single pronounced jump substituting for several smaller ones. This kind of behavior can be observed only for large enough R and d in the presence of many resonant subbands. Here the spin-Zeeman splitting of different but close to each other quasiparticle branches does not result in the formation of clearly distinguished subbranches any more. Instead, we can obtain bunches of almost degenerate subbranches: we note that the term $\mu_B H_{||}(m + \sigma)$ in Eq. (4.28) has the same value, e.g., for $m = -3$, $\sigma = 1$ and for $m = -1$, $\sigma = -1$. This complex interplay can lead to a significant rearrangement of jumps in $\bar{\Delta}$ and, sometimes, even to larger jumps that arise due the spin-Zeeman splitting. Another deviation from, say, the doubling rule mentioned above is for resonant enhancements that develops owing to contribution of states with $|m| = 1$. In this case we will obtain a jump in $\bar{\Delta}$ driven by a downward shift of the quasiparticle branch associated with $m = -1$. The spin-Zeeman splitting replaces m by $m + \sigma$. For $\sigma = 1$ $E_{jmk,\sigma}$ does not include the Zeeman term any more. It appears only in $E_{jmk,\sigma}$ for $\sigma = -1$. As a result, one jump in the absence of the spin-magnetic-field interaction will be replaced by a smaller jump in its presence.

4.3.3 Quantum-size oscillations of the paramagnetic limiting field

It is well-known that the upper limit for the critical magnetic field is controlled by the paramagnetic breakdown of the Cooper pairs.[96] To investigate how such a breakdown is sensitive to the quantization of the electron motion, here we continue our numerical study of the spin-generalized BdG equations but we switch off the orbital-magnetic interaction, i.e. the term $\mu_B m H_{||}$ is removed from Eq. (4.28). As the states with negative azimuthal quantum numbers are responsible for the cascades of jumps in $\bar{\Delta}$ as function of $H_{||}$, one can easily see that removing the aforementioned term makes the system less sensitive to $H_{||}$. So, the resulting paramagnetic limiting field $H_{\rm par}$ will be generally larger than $H_{||}$ discussed in previous subsection. To go in more detail on this issue, we plot $H_{\rm par}$ as calculated from the spin-generalized BdG equations versus d for $R = 0.1\,$nm and $1.0\,$nm, see Figs. 4.10(a) and (b). Comparing the results in panel (a) with those of Figs. 4.8(a) we can see that $H_{\rm par}$ is larger than $H_{c,||}$ by a factor of about $2-3$. The difference between $H_{\rm par}$ and $H_{c,||}$ gets enhanced when passing to larger R. In particular, $H_{\rm par}$ in Fig. 4.10(b) differs from $H_{c,||}$ by a factor of about $3-4$ for the resonant points and by an order of magnitude for nonresonant thicknesses. Such a significant difference agrees with the fact that the spin-magnetic-field interaction brings only small corrections ($\sim 10\%$) to the effect of the orbital magnetic moments, as found in previous subsection. Due to the quantum-size effects, $H_{\rm par}$ exhibits pronounced size-dependent oscillations with significant resonant enhancements over the Clogston-Chandrasekhar field H^{CC} [the dashed line in Figs. 4.10(a) and (b)], i.e., the paramagnetic limiting field in bulk $H^{CC} = \Delta_{\rm bulk}/(\sqrt{2}\mu_B) \approx 3.6\,$T. However, when a superconducting resonance decays due to a change in d, $H_{\rm par}$ can drop even below H^{CC}. It is instructive to get a simple analytic estimate for the paramagnetic limiting field for a superconducting nanowire. Based on Eq. (4.28) and the above discussion of our numerical results, we can find$H_{\rm par} \approx \Delta_{jm}(H_{||} = 0)/\mu_B$, where j and m are the quantum numbers associated with a resonant subband (or a former resonant subband as for the nonresonant case). In most cases $\Delta_{jm} \approx \bar{\Delta}$ and, so we obtain

$$H_{\rm par} \approx \bar{\Delta}(H_{||} = 0)/\mu_B. \tag{4.31}$$

There are two points that make Eq. (4.31) different from the Clogston-Chandrasekhar result. First, the translational invariance in the radial direction is broken and, so, the spatially averaged order parameter appears in Eq. (4.31) rather than the uniform pairing energy as in the expression for the Clogston-Chandrasekhar field. Second, the factor $1/\sqrt{2}$ is not present in Eq. (4.31). At first sight it can lead to some inconsistency because it seems that $H_{\rm par}$ of Eq. (4.31) does not approach H^{CC} when, e.g., $d \to \infty$. However, this is not true because the result of Eq. (4.31) is derived for $R, d \ll \lambda$, with λ the magnetic penetration depth, i.e., when a magnetic field easily penetrates the system.

Despite the rather simplified character of Eq. (4.31), it provides a reasonable estimate of $H_{\rm par}$. This can be seen from Figs. 4.10(c)-(e), where the de-

pendence of $\bar{\Delta}$ on $H_{||}$ is shown for $R = 0.1\,\mathrm{nm}$ and $d = 2.12\,\mathrm{nm}$ (c), $R = 0.1\,\mathrm{nm}$ and $d = 1.7\,\mathrm{nm}$ (d), $R = 1.0\,\mathrm{nm}$ and $d = 2.8\,\mathrm{nm}$ (e), and $R = 1.0\,\mathrm{nm}$ and $d = 3.07\,\mathrm{nm}$ (f). For panel (c), Eq. (4.31) gives 19 T, which is only 10% higher than $H_{\mathrm{par}} = 17.3\,\mathrm{T}$ shown in the figure. It is worth noting that the Clogston-Chandrasekhar-like estimate produces $\bar{\Delta}(H_{||} = 0)/(\sqrt{2}\mu_B) = 13\,\mathrm{T}$, which is 30% lower than the result from a numerically solution of the spin-generalized BdG equations. For panel (d), use of Eq. (4.31) results in the estimate $H_{\mathrm{par}} \approx 26.6\,\mathrm{T}$, which is about 10% lower than our numerical result $H_{\mathrm{par}} = 28.9\,\mathrm{T}$. In Figs. 4.10(e) and (f) we have $H_{\mathrm{par}} = 14.3$ and $11.5\,\mathrm{T}$, respectively. Here Eq. (4.31) gives $15.7\,\mathrm{T}$ and $12.7\,\mathrm{T}$. As seen, corrections to the estimate given by Eq. (4.31) are generally within 10%. Concluding this subsection, it is worth noting that the quantum-size cascades survive in the dependence of $\bar{\Delta}$ on $H_{||}$ even in the absence of the orbital-magnetic interaction. They appear because the quasiparticle branches with $\sigma = -1/2$ are not degenerate due to the difference in Δ_{jm}. As already mentioned in previous section, this difference is a manifestation of the formation of Andreev states induced by quantum confinement (see [97]).

4.4 DISCUSSION ON SURFACE ROUGHNESS AND SUPERCONDUCTING FLUCTUATIONS

We want to note that up to now our analysis was limited to ideal case of a hollow nanocylinder without surface roughness and in the absence of any diameter variation along the wire. Typical experimental diameter variations along the wire are relatively slow and can be taken into account via an adiabatic treatment, resulting in a variation of the superconducting order parameter along the longitudinal coordinate. As a result, along the wire there will be a set of domains with enhanced superconducting condensate (they correspond to resonant values of the diameter) interconnected by weak superconducting links (governed by non-resonant diameters). The evolution of each domain in a parallel magnetic field will exhibit a cascade decay of the local superconducting order parameter similar to that in an ideal nanocylinder. Understanding the impact of surface roughness requires a more involved analysis. In high-quality superconducting nanowires one should distinguish the perpendicular and longitudinal motion. As the electron mean free path is close to or even larger than the nanowire width, the perpendicular motion can not be considered as diffusive. In this case an adequate manner to take into account the surface roughness is to invoke available models for accounting such imperfections in semiconductor nanowires, see, e.g., [103, 104]. These models introduce corrections to single-electron energies due to the presence of the electron-impurity potential. Below we are based on a simplified approach of [65], where the single-electron energies in the presence of surface imperfections, i.e., $\xi^{(\mathrm{im})}_{jmk}$, are approximated by (for simplicity, let us consider $R = 0$,

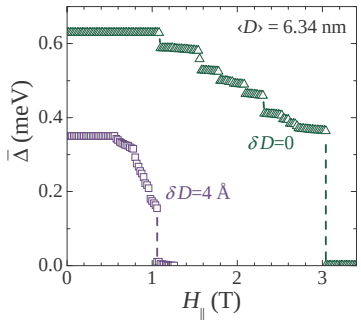

Fig. 4.11 (Color online) $\bar{\Delta}$ as function of $H_{||}$ in the presence of surface roughness for $R = 0$ and $\langle D\rangle = 2\langle d\rangle = 6.34\,\text{nm}$: triangles are for the ideal case with $\delta D = 0$; squares represent the results obtained from Eq. (4.32) with $\delta D = 4\,\mathring{A}$.

i.e., a cylinder with diameter $D = 2d$)

$$\xi_{jmk}^{(\text{im})} = \xi_{jmk} + s_{jmk}\left|\frac{d\xi_{jmk}}{dD}\right|\delta D, \tag{4.32}$$

with ξ_{jmk} given by Eq. (4.5) and s_{jmk} a random variable uniformly distributed in $[-0.5, 0.5]$. As seen, Eq. (4.32) accounts for the uncertainty in the single-particle kinetic energy due to fluctuations in the confining dimension. We performed a numerical study of the BdG equations with Eq. (4.32). For illustration, in Fig. 4.11 the spatially averaged order parameter is shown versus $H_{||}$ for $R = 0$ and $\langle d\rangle = 3.17\,\text{nm}$ (i.e., for a cylindrical nanowire with the mean diameter $\langle D\rangle = 6.34\,\text{nm}$) for the ideal case of $\delta D = 0$ (triangles) and in the presence of the surface roughness with $\delta D = 4\mathring{A}$. As could be expected, surface roughness smoothes the size-dependent oscillations of the DOS at the Fermi level and, as a result, makes resonant enhancements less pronounced. In particular, for $\delta D = 4\mathring{A}$ the critical magnetic field $H_{c,||}$ in Fig. 4.11 is decreased by almost a factor of 3 and $\bar{\Delta}$ (taken at at $H_{||} = 0$) becomes smaller by a factor of 2. However, even in the presence of such significant surface imperfections the cascade decay of $\bar{\Delta}$ survives. Our choice of $D = 6.34\,\text{nm}$ is not crucial for the basic conclusions and similar results with clear signatures of remaining quantum cascades can be obtained for other diameters, see Fig. 4.12.

Another important point to address concerns the superconducting fluctuations in metallic nanowires. As mentioned in the Introduction, our previous numerical investigation [23] shows that the quantum cascades in $\bar{\Delta}$ as function of $H_{||}$ can be significant in superconducting nanowires with diameters $\lesssim 15\,\text{nm}$. However, it is known that quantum phase slips proliferate in superconducting nanowires with diameters $\lesssim 8\,\text{nm}$, see, e.g., [9, 10, 90], which corrupts the superconducting state, leading to a long tail in the resistance below the critical temperature. This may question use of the mean-field model

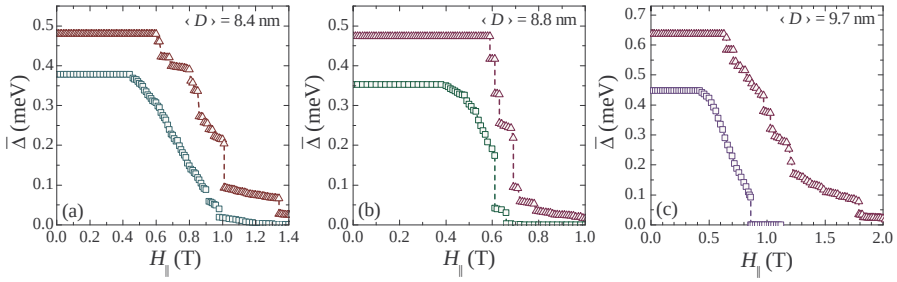

Fig. 4.12 (Color online) Effect of surface roughness on $\bar{\Delta}$ as function of $H_{||}$ for $R = 0$ and various mean diameters $\langle D\rangle = 2\langle d\rangle = 8.4\,\mathrm{nm}$ (a), 8.8 nm (b) and 9.7 nm (c). In each panel triangles represent the ideal cylindrical nanowire and squares show results calculated from Eq. (4.32) with $\delta D = 2\mathring{A}$.

for our nanoscale superconducting systems. However, as already mentioned in the Introduction, the mean-field approach is useful even for nanowires with proliferating quantum-phase fluctuations of the order parameter. The amplitude of the mean-field order parameter is an important quantity that controls the rate of the quantum-phase slips and, therefore, the remaining resistance below the critical temperature. So, based on the predictions of our work, one can expect the appearance of a cascade of jumps in the remaining resistance below T_c as function of a magnetic field. It is also of interest to discuss thermal fluctuations. They are not extremely pronounced in high-quality superconducting nanowires. In particular, from [9] we can learn that the resistance drops rather fast below T_c even for aluminum nanowires with thickness $\sim 10\,\mathrm{nm}$. Such a drop is more than by order of magnitude when T decreases from T_c to $0.9\,T_c$, see Fig. 2 in [9]. It means that we still have a well-pronounced transition with a thermal broadening of about $\delta T = 0.1\,T_c$. This broadening can provide us with an estimate of the Ginzburg-Levanyuk parameter ($\mathrm{Gi} \sim \frac{\delta T}{T_c} \approx 0.1$) that measures the impact of thermal fluctuations around T_c. In the situation when the conventional Ginzburg-Landau formalism is not well justified for superconducting nanowires (the nanowire diameter can be much smaller than the BCS coherence length), this gives a reasonable guess about the role of thermal fluctuations. Such an estimate of Gi shows that the mean-field treatment is still applicable for low enough temperatures even in high-quality nanowires with diameters down to $5 - 10\,\mathrm{nm}$. It is worth noting that a naive calculation of Gi in superconducting nanowires with width $\sim 10\,\mathrm{nm}$ based on conventional Ginzburg-Landau theory in the clean limit, see [27], produces a similar result, i.e., $\mathrm{Gi} \sim 0.1$ for diameters $\approx 10\,\mathrm{nm}$ and $\mathrm{Gi} \sim 0.2$ for diameters $\approx 5\,\mathrm{nm}$. We also note that high-quality Al and Sn superconducting nanowires discussed in [8–10, 16] are far from the dirty limit of strongly disordered superconducting nanowires, e.g., made of MoGe, see [105]. In disordered nanowires the electron mean free path is significantly smaller

than the nanowire diameter, and the electron motion is diffusive. As a result, the superconducting temperature is systematically reduced with decreasing the nanowire diameter. In addition, the superconducting fluctuations play a more significant role. For the transition temperature of about 3.5 K in MoGe superconducting nanowires with width ~ 10 nm the thermal broadening of the resistance transition is ≈ 1 K, see [105]. This makes it possible to expect that Gi ≈ 0.3, which is by a factor of 3 larger than the above estimate for aluminum nanowires. In high quality superconducting nanowires the electron mean free path is about the nanowire diameter (i.e., the main issue of disorder is surface roughness), and the formation of single-electron subbands is not overshadowed by impurity/roughness scattering. As a consequence, the superconducting temperature is systematically shifted up as compared to bulk with decreasing diameter, see [26].

4.5 CONCLUSIONS

Concluding, we investigated how quantum-size cascades appearing in the scenario of a superconducting-to-normal transition in metallic nanowires with increasing parallel magnetic field can be influenced by changing the confining geometry, by thermal smoothing and by the spin-magnetic-field interaction. Our study was based on a numerical solution of the BdG equations for a hollow metallic nanocylinder. Varying its inner radius R and its wall thickness d, we observed a qualitative change in the cascades when passing from the nanowire-like regime, i.e., $R/d \ll 1$, to the nanofilm-like regime, i.e., $d \ll R$. In particular, while being pronounced for $R/d \ll 1$, jumps in the order-parameter as function of an external parallel magnetic field are significantly smoothed for $R \gg d$. The reason for such a smoothing is that an increase in R results in a significant increase of the number of single-electron subbands that contribute to the order parameter. Hence, the relative contribution of each subband is strongly reduced and, as a result, the appearance of negative quasiparticle energies in one of subbands will no longer have an appreciable effect on the solution.

We also found that a smoothing of the jumps in the cascades occurs when temperature is non-zero. However, here the reason for smoothing is different. The point is that at finite temperature there is a non-zero population of quasiparticles already at zero magnetic field, i.e., there is thermally-activated depairing. Therefore, the effect of any additional depairing mechanism, e.g., due to the negative-energy excitations appearing in the magnetic field, is weakened because of such thermally-activated depairing.

We found that taking into account the spin-magnetic-field interaction increases the number of small jumps in a given cascade, which is due to the spin-Zeeman splitting of the quasiparticle energies. In most cases the critical magnetic field is smaller in the presence of the spin-magnetic-field interaction. However, interestingly, due to the complex interplay of the orbital and spin-

magnetic-field effects, the critical magnetic field can sometimes be enhanced. The reason is that pronounced jumps in quantum-size cascades occur when a quasiparticle branch associated with the resonant subband touches zero at some magnetic field. In this case the order parameter, as a rule, immediately drops down to zero, which measures $H_{c,||}$. The spin-magnetic-field interaction splits each quasiparticle branch in two parts, which, as a rule, divides the initial pronounced jump in two smaller ones. Sometimes, the second of them can be situated at a higher magnetic field as compared to the initial jump and, thus, we obtain a higher critical field. In addition, the spin-Zeeman splitting reduces the effect of each subband on the superconducting quantities, which can lead to smoothing of some of the jumps in the cascades. This can also contribute to rare enhancements of $H_{c,||}$ when taking into account the spin magnetic moments. Due to significant orbital motion in a hollow nanocylinder, we found that the paramagnetic-limiting field $H_{\rm par}$ is essentially larger than $H_{c,||}$ calculated when including orbital and spin magnetic moments. This can be different for less symmetric confining geometries, e.g., for a rectangular-cross-section nanowire, and deserves additional investigations. The paramagnetic limiting field $H_{\rm par}$ was shown to significantly oscillate with R and d due to the quantum-size effects. For the resonant points, $H_{\rm par}$ is significantly enhanced as compared to the bulk Clogston-Chandrasekhar field H^{CC} due to resonant enhancements of the pairing energy. We remark that the spin-orbit coupling, as is known [55], can reduce effects of the paramagnetic pair breaking. However, due to a minor contribution of the paramagnetic mechanism, the role of spin-orbit coupling will not be essential in our system and we leave this subject for future investigations.

Publications. The results presented in this chapter were published as:

- **Yajiang Chen**, A. A. Shanenko, M. D. Croitoru, and F. M. Peeters, *Quantum cascades in nano-engineered superconductors: geometrical, thermal and paramagnetic effects*, J. Phys.: Condens. Matter (accepted).

5

Molecule-like pairing in superconducting nanofilms

5.1 INTRODUCTION

Advances in self-assembly and nanofabrication resulted recently in the thinnest superconductors, i.e., single-crystalline metallic nanofilms with atomically uniform thickness down to a few monolayers, see, e.g., Refs. [5, 13, 19, 61, 106]. They are characterized by an extraordinary purity and, so, the only issue of disorder in the case of interest is due to the interface between the substrate and the nanofilm. Such an interface has an effect on the reflection of electron waves (it is not perfectly specular). Nevertheless, there are clear signatures of the formation of discrete levels for the perpendicular electron motion [i.e., quantum-well states (QWS)] in tunneling spectra [5, 19]. Pairing correlations appear to be very robust in single-crystalline nanofilms so that even Pb and In films with thickness of 1 ML were found not to exhibit any considerable signs of degradation of superconductivity due to fluctuations [13]. Experimental results for the temperature dependence of the pairing gap show almost no deviations from the ordinary BCS picture, see, e.g., Refs [5, 13, 19]. However, it is worth noting that, for some samples, there appear signatures of suppression of density of states (DOS) in the tunneling spectra at low voltage above T_c, which resembles, to some extent, the pseudogap physics of high-T_c superconductors [13, 60].

Another recent experimental breakthrough concerns the iron-pnictides (for a review see, e.g., Ref. [93]), i.e., a new generation of multi-band superconductors specified by the interplay of different band-dependent superconducting condensates. This renewed the interest in multi-band superconductivity. In particular, one of the most intriguing points is a competition of the characteristic lengths of the different condensates [107–110] and a possible contri-

bution of such a competition to new phenomena, including recently observed and strongly debated unconventional patterns of the vortex distribution in magnesium-diboride [108].

The question arises if there is any relation between bulk multi-band superconductors and high-quality superconducting nanofilms? In fact, they are similar in many important respects. As already mentioned above, tunneling experiments demonstrate that the conduction band in metallic nanofilms splits up into a series of subbands in such a way that the bottom of each subband is at the energy position of the corresponding QWS [5, 19, 60]. For example, Pb nanofilms with thickness 4-5 ML are two-band(subband) superconductors [5, 19]. In those metallic superconducting nanofilms the energetic position of each subband with respect to the Fermi level E_F changes with thickness, i.e., the discrete perpendicular levels scale as $1/d^2$, with d the thickness of the nanofilm while the accompanying variation of E_F is almost insignificant. Typically, E_F only slightly shifts down when increasing the thickness. However, such a shift becomes more pronounced for smaller thicknesses, i. e., in the presence of a few single-electron subbands. In particular, for only one available subband, its bottom can never cross the Fermi level which will simply shifts together with the subband bottom. Additional reasons for shifting in energy of the subband bottoms as measured from E_F are due to fabrication circumstances: the presence or absence of a protective cover, an effect of the wetting layer, use of different substrates etc., which can significantly change the behavior of the single-electron wave functions at the interface (and, so, the QWS energy). Thus, the relevant microscopic parameters of the different subbands, e.g., DOS and the Fermi velocity (in the parallel direction), are not fixed and can significantly vary from sample to sample even for the same thickness. It is possible to expect that these parameters can, in principle, be tailored in future experiments. Therefore, it is timely to investigate in more detail the properties of the superconducting state in metallic single-crystalline nanofilms in the case when the bottom of one of the relevant single-electron subbands approaches the Fermi level. Below we show that the pairing in such a subband exhibits a clear molecule-like trend, which is very similar to the BCS-BEC crossover investigated at length in cold atomic gases, see, e.g., Ref. [111]. In particular, we predict that striking results can be obtained for Pb nanofilms with thicknesses 4-5 ML, where up to half of all the Cooper pairs nearly collapse, i.e., shrinking in the lateral size (parallel to the nanofilm) down to a few nanometers. Our finding significantly compliments the recent first observation of the BCS-BEC crossover in a solid-state material, i.e., in one of the available subbands in a multiband superconducting iron-chalcogenide $FeSe_xTe_{1-x}$, see Ref. [112].

The present chapter is organized as follows. In Sec. 5.2 we address the criterion of the BCS-BEC crossover in a given single-electron subband. We show that a condensed pair of electrons significantly shrinks in its lateral size (parallel to the nanofilm) when the ratio of the parallel kinetic energy of electrons to the absolute value of the potential energy becomes smaller than

one, i.e., when the subband bottom approaches the Fermi level. In Sec. 5.3 we investigate 4 and 5 ML thick lead nanofilms, where only two single-electron subbands are occupied, i.e., we have a coherent mixture of two condensates, and one of them is formed by extremely small Cooper pairs. Our conclusions are given in Sec. 5.4.

5.2 BCS-TO-BEC CROSSOVER DRIVEN BY QUANTUM-SIZE EFFECTS

It is well-known that the governing parameter for the BCS-BEC crossover in the system with fermionic pairing correlations is the ratio of the relevant kinetic energy K to the absolute value of the potential energy U. When $K/|U| > 1$, we are in the BCS regime with loosely bound and rather extensive Cooper pairs (the BCS limit corresponds to $K/|U| \to \infty$). On the opposite side of the crossover, when $K/|U| \ll 1$, molecule-like bound pairs appear with the BEC limit $K/|U| \to 0$. Here it is worth noting that an extensive analysis of the behavior of the kinetic and potential energy through the BCS-BEC crossover for the attractive Hubbard model [113] gave $K/|U| \approx 2.2$ at the BCS side, while approaching the BEC regime it resulted in $K/|U| \approx 0.03$. Interestingly, the right balance between the strength of the kinetic and interaction energy has been considered as an essential feature of high-T_c superconductivity [114].

Keeping in mind the criterion based on the ratio $K/|U|$, let us examine what happens with a Cooper pair in a given subband when changing the position of its bottom with respect to E_F in single-crystalline nanofilms. If the bottom of the subband is situated far below the Fermi level, the mean kinetic energy of electrons in this subband comes mostly from the parallel motion, i.e., $K_\perp \ll K_{||} \sim E_F$. In this case $K_{||}/|U| \sim E_F/|U| \gg 1$. However, when the subband bottom (or the corresponding QWS) approaches the Fermi surface, we have $K_\perp \to E_F$ and, so, $K_{||}$ becomes much smaller than E_F. The parallel motion of electrons is reduced, and such a redistribution of the kinetic energy between the perpendicular and parallel spatial degrees of freedom leads to a significant decrease in the ratio $K_{||}/|U|$. Furthermore, when the subband bottom goes above the Fermi level (such a subband still makes a contribution unless its bottom is above $E_F + \hbar\omega_D$, with ω_D the Debye frequency), $K_{||} \to 0$ and, hence, $K_{||}/|U|$ becomes extremely small, i.e., $K_{||}/|U| \ll 1$. Therefore, when assuming that the ratio $K_{||}/|U|$ controls the lateral size of a condensed fermionic pair associated with the corresponding subband in the nanofilm, we expect from the above arguments a significant reduction in the lateral size of the Cooper pairs.

To go into more detail, let us consider a superconducting nanoslab in the clean limit, with perfectly specular reflection at the boundaries. Possible effects of the scattering of electrons at the interface between a substrate and the

nanofilm will be discussed later. The translational invariance in the perpendicular direction is broken due to quantum confinement and, so, we deal with a spatially nonuniform order parameter $\Delta(\mathbf{r})$ problem. As a consequence, the ordinary BCS self-consistent equation should be abandoned in favor of a more elaborate analysis based on the BdG equations (or, equally, on the Gor'kov Green's function formalism). As shown in Ref. [115], the BdG equations are appropriate to describe the BCS-BEC crossover in spatially nonuniform fermionic systems at nearly zero temperatures. In particular, it has been shown in Ref. [115] that the BdG equations reproduce the Gross-Pitaevskii equation for the condensate wave function at the BEC side of the crossover. Therefore, if our reasoning based on $K_{||}/|U|$ is correct, we can expect that the spatial profile of the wave function of a condensed electronic pair will change (dramatically) crossing over from the BCS regime (i.e., $K_{||}/|U| \gg 1$) to the BEC regime (i.e., $K_{||}/|U| \ll 1$). In the BCS regime this pair-wave function will have many oscillations with the period of the Fermi wavelength λ_F and will decay over a significantly larger distance (as compared to λ_F) determined by the size of the extended Cooper pairs. Approaching the BEC regime, the pair-wave function will have only some insignificant residual oscillations (e.g., due to the presence of the ultraviolet cut-off) and will be concentrated at short separations between electrons associated with the size of a molecule-like pair (it is close to or smaller than λ_F). We limit ourselves to zero temperature and ignore pairing of electrons between different subbands, which is justified when the intersubband energy spacing, i.e., $\delta \sim \frac{\hbar^2}{2m}\frac{\pi^2}{d^2}$, is significantly larger than the pairing energy (it is always true for ultrathin films). In this case it is possible to take into account only the pairing of the time reversed states, which means that (see Sec. 1.2.3.2)

$$u_{i,\mathbf{k}}(\mathbf{r}) = \mathcal{U}_{i,\mathbf{k}}\phi_{i,\mathbf{k}}(\mathbf{r}), \quad v_{i,\mathbf{k}}(\mathbf{r}) = \mathcal{V}_{i,\mathbf{k}}\phi_{i,\mathbf{k}}(\mathbf{r}), \tag{5.1}$$

where i is the quantum number associated with the quantum-confined motion in the z direction, $\mathbf{k}$ is the wave vector of the quasi-free motion of electrons in the direction parallel to the nanofilm, $u_{i,\mathbf{k}}(\mathbf{r})$ and $v_{i,\mathbf{k}}(\mathbf{r})$ are the particle-like and hole-like quasiparticle wave functions, and $\hat{H}_e\phi_{i,\mathbf{k}}(\mathbf{r}) = \xi_{i,\mathbf{k}}\phi_{i,\mathbf{k}}(\mathbf{r})$ with $\xi_{i,\mathbf{k}}$ the single-electron energy measured from the Fermi level, and the factors $\mathcal{U}_{i,\mathbf{k}}$ and $\mathcal{V}_{i,\mathbf{k}}$ are chosen real, together with the order parameter. Based on Eqs. (1.45), (1.62) and (5.1), one can find

$$\mathcal{U}^2_{i,\mathbf{k}} = \frac{1}{2}\Big[1 + \frac{\xi_{i,\mathbf{k}}}{\varepsilon_{i,\mathbf{k}}}\Big], \quad \mathcal{V}^2_{i,\mathbf{k}} = \frac{1}{2}\Big[1 - \frac{\xi_{i,\mathbf{k}}}{\varepsilon_{i,\mathbf{k}}}\Big], \tag{5.2}$$

with $\varepsilon_{i,\mathbf{k}} = \sqrt{\xi^2_{i,\mathbf{k}} + \Delta_i^2}$, where the subband-dependent gap

$$\Delta_i = \int \mathrm{d}^3 r\, \phi^*_{i,\mathbf{k}}(\mathbf{r})\Delta(\mathbf{r})\phi_{i,\mathbf{k}}(\mathbf{r}) \tag{5.3}$$

obeys the following BCS-like self-consistency equation:

$$\Delta_{i'} = \sum_{i,\mathbf{k}} \Phi_{i'i} \frac{\Delta_i}{2\varepsilon_{i,\mathbf{k}}}, \tag{5.4}$$

with $\Phi_{i'i} = g \int \mathrm{d}^2 r |\phi_{i',\mathbf{k}'}(\mathbf{r})|^2 \phi_{i,\mathbf{k}}(\mathbf{r})|^2$. As usual, to avoid the ultraviolet divergence, the sum in Eq. (5.4) runs over the states with $|\xi_{i,\mathbf{k}}| < \hbar\omega_D$, where ω_D stands for the Debye frequency. For Pb we adopt $\hbar\omega_D = 8.27\,\mathrm{meV}$, see Ref. [67].

To check our arguments about the influence of the ratio $K_{||}/U$ on the lateral subband-dependent size of the Cooper pairs, we need to study the "wave function" of a condensed fermionic pair, i.e., the anomalous average of the field operators $\langle\hat{\psi}_\uparrow(\mathbf{r})\hat{\psi}_\downarrow(\mathbf{r}')\rangle$. More precisely, the anomalous average is proportional to the bound-like eigenfunction of the two-particle density matrix, which can be safely interpreted as the wave function of a condensed fermionic pair, see, e.g., Refs. [116] and [117]. This quantity is related to the particle-like and hole-like vectors of the BdG equations through the Bogoliubov canonical transformation

$$\hat{\psi}_\uparrow(\mathbf{r}) = \sum_{i,\mathbf{k}} \Big[u_{i,\mathbf{k}}(\mathbf{r})\, \gamma_{i,\mathbf{k},\uparrow} - v^*_{i,\mathbf{k}}(\mathbf{r})\, \gamma^\dagger_{i,-\mathbf{k},\downarrow} \Big], \tag{5.5a}$$

$$\hat{\psi}_\downarrow(\mathbf{r}) = \sum_{i,\mathbf{k}} \Big[u_{i,\mathbf{k}}(\mathbf{r})\, \gamma_{i,-\mathbf{k},\downarrow} + v^*_{i,\mathbf{k}}(\mathbf{r})\, \gamma^\dagger_{i,\mathbf{k},\uparrow} \Big], \tag{5.5b}$$

where $\gamma^\dagger$ and γ are the quasiparticle (bogolon) operators. From Eq. (5.5) we find (for $T = 0$)

$$\langle\hat{\psi}_\uparrow(\mathbf{r})\hat{\psi}_\downarrow(\mathbf{r}')\rangle = \sum_{i,\mathbf{k}} \mathcal{U}_{i,\mathbf{k}}\mathcal{V}_{i,\mathbf{k}}\, \phi^*_{i,\mathbf{k}}(\mathbf{r})\phi_{i,\mathbf{k}}(\mathbf{r}'), \tag{5.6}$$

which can be rearranged to

$$\langle\hat{\psi}_\uparrow(\mathbf{r})\hat{\psi}_\downarrow(\mathbf{r}')\rangle = \sum_i \frac{\Delta_i}{2}\, \varphi_i(z)\varphi^*_i(z')\, \eta_i(x-x', y-y'), \tag{5.7}$$

where $\varphi_i(z)$ is the single-electron wave function associated with the $i-$th QWS, and $\eta_i(x-x', y-y') = \eta_i(\rho)$ [with $\rho = \sqrt{(x-x')^2 + (y-y')^2}$] controls the decay of the fermionic-pair "wave function" in the direction parallel to the nanofilm. This quantity can be represented in the form

$$\eta_i(\rho) = \int \frac{\mathrm{d}k}{2\pi}\, k\, \theta(\hbar\omega_D - |\xi_{i,\mathbf{k}}|)\, \frac{J_0(k\rho)}{\sqrt{\xi^2_{i,\mathbf{k}} + \Delta^2_i}}, \tag{5.8}$$

with $k = \sqrt{k_x^2 + k_y^2}$ and J_0 the Bessel function of the first kind of order 0. Let us here introduce the QWS energy $\varkappa_i$, which makes it possible to write

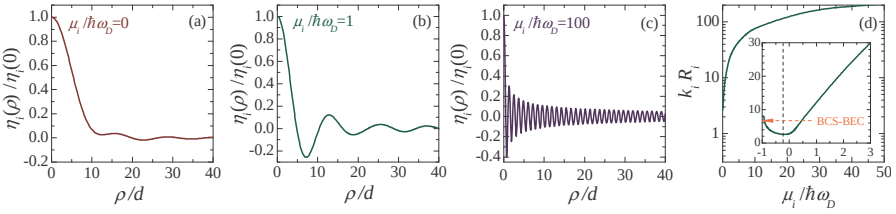

Fig. 5.1 (Color online) (a,b,c) The subband-dependent pair "wave function" $\eta_i(\rho)$ versus ρ for different values of μ_i, i.e., $\mu_i/\hbar\omega_D = 0$ (a), $\mu_i/\hbar\omega_D = 1$ (b), and $\mu_i/\hbar\omega_D = 100$ (c). Panel (d) shows how the product $k_i R_i$ depends on the ratio $\mu_i/\hbar\omega_D$ ($1/k_i$ is the measure for the mean distance between electrons in a given subband and R_i stands for the pair size). The inset in (d) is a room around $\mu_i = 0$, which shows details of a drop in the product $k_i R_i$ when the bottom of the corresponding single-electron subband approaches the Fermi level (the BCS-BEC crossover is reached below the dashed line, i.e., $k_i R_i < 2\pi$).

$\xi_{i,\mathbf{k}} = \frac{\hbar^2}{2m}(k_x^2 + k_y^2) - \mu_i$, with $\mu_i = E_F - \varkappa_i$. The asymptote for $\eta_i(\rho)$ at large ρ can be calculated analytically in several interesting cases. When the QWS level (i.e., the subband bottom) is situated far below the Fermi level, i.e., $\mu_i > 0$ and $\mu_i \gg \Delta_i$, we find

$$\eta_i(\rho) \simeq \frac{m}{\pi\hbar^2} J_0(k_i\rho)\, K_0(\rho/R_i^{(1)}) \quad \left[\rho/R_i^{(1)} \gtrsim 1\right], \tag{5.9}$$

where K_0 is the Macdonald function and $R_i^{(1)} = \hbar v_i/\Delta_i$, with $v_i = \hbar k_i/m$ the subband-dependent Fermi velocity (for parallel motion). This is nothing more but the ordinary BCS behavior: first, there are fast oscillations with period of the subband-dependent Fermi wavelength $\lambda_i = 2\pi/k_i$ [this comes from $J_0(k_i\rho)$]; second, we obtain the exponential overall decay governed by $R_i^{(1)}$, as seen from the asymptote of $K_0(\rho/R_i^{(1)})$.

When QWS touches the Fermi level, i.e., $\mu_i = 0$, Eq. (5.9) does not hold any more and the behavior of $\eta_i(\rho)$ changes dramatically. In this case, assuming $\rho \to \infty$, we arrive at

$$\eta_i(\rho) \simeq \frac{m}{\pi\hbar^2} J_0(\rho/R_i^{(2)})\, K_0(\rho/R_i^{(2)}) \quad \left[\rho/R_i^{(2)} \gtrsim 1\right], \tag{5.10}$$

with $R_i^{(2)} = \hbar/\sqrt{m\Delta_i}$. As seen, the characteristic length controlling the decay of the pair "wave function" in Eq. (5.10) is completely different from that in Eq. (5.9). Moreover, $R_i^{(2)}$ is significantly smaller than $R_i^{(1)}$. As $R_i^{(1)}$ can be well approximated by $\hbar v_F/\Delta_i$, with $v_F = \sqrt{2E_F/m}$, then we obtain

$$R_i^{(1)}/R_i^{(2)} \propto \sqrt{E_F/\Delta_i}. \tag{5.11}$$

In addition, the fast oscillations present in Eq. (5.9) disappear in Eq. (5.10). Instead, we obtain a rather slowly oscillating factor $J_0(\rho/R_i^{(2)})$ but the role

of these oscillations is almost negligible because they can only manifest themselves for separations of electrons in a condensed pair such that $\eta_i(\rho)$ almost approaches zero. So, our expectations based on the behavior of the parameter $K_{||}/|U|$ are relevant: when the subband bottom touches the Fermi level, the Cooper pairs associated with this subband nearly collapse (as compared to typical values of the zero-temperature BCS coherence length) in the lateral direction, shrinking by a factor of $\sqrt{E_F/\Delta_i} \sim 10^2$. Such shrinking continues when μ_i crosses zero and becomes negative. In particular, when $\hbar\omega_D \gg |\mu_i| \gg \Delta_i$, Eq. (5.8) results in

$$\eta_i(\rho) \simeq \frac{m}{\pi\hbar^2} K_0(\rho/R_i^{(3)}) \quad \left[\rho/R_i^{(3)} \gtrsim 1\right], \tag{5.12}$$

with $R_i^{(3)} = \hbar/\sqrt{2m|\mu_i|} \ll R_i^{(2)}$. Thus, based on Eqs. (5.10), (5.11) and (5.12), we find a giant drop, from microns to nanometers, in the lateral size of a condensed fermionic pair associated with the single-electron subband whose bottom approaches E_F. This molecule-like trend in the reconstruction of the electronic pairing is very similar to the one predicted previously for high-quality superconducting nanowires [23, 27, 91].

More details about $\eta_i(\rho)$ can be obtained by numerically calculating the integral in Eq. (5.8). Using $\Delta_i = 1.08\,\text{meV}$, which results from tunneling measurements of 4 ML thick lead nanofilms [5, 19], we investigate how the total profile of η_i evolves with changing μ_i, in addition to the asymptotic behavior discussed in the previous paragraph. Figure 5.1 shows numerical results for $\eta_i(\rho)$ for different values of μ_i, i.e., $\mu_i/\hbar\omega_D = 0$ (a), $\mu_i/\hbar\omega_D = 1$ (b), and $\mu_i/\hbar\omega_D = 100$ (c). As seen, the numerical results fully support the analytical results given by Eqs. (5.9), (5.10) and (5.12). In particular, we obtain the typical BCS picture of anomalous correlations when the subband bottom is situated far below E_F [see panel (c)] but we approach a molecule-like character of the spatial distribution of electrons in a condensed pair for $\mu_i \to 0$ [see panel (a)]. Fast oscillations in $\eta_i(\rho)$ at Fig. 5.1(c) are first converted into slow oscillations shown in panel (b) [here λ_i significantly increases as compared to panel (c)] and, then, are almost washed out in Fig. 5.1(a). Only small residual oscillations can be observed in panel (a), and the period of these oscillations is about the decay radius for $\eta_i(\rho)$, which is in agreement with Eq. (5.10).

To further highlight similarities with the ordinary BCS-BEC crossover driven by the Feshbach resonance in ultracold Fermi gases, we show in Fig. 5.1(d) how the product $k_i R_i$ depends on μ_i, where R_i is the mean square radius calculated with the "wave function" $\eta_i(\rho)$ and $k_i = (3\pi^2 n_i)^{1/3}$, with n_i the mean electron density in subband i. We note that here k_i is introduced to measure the mean distance $\approx \lambda_i = 2\pi/k_i$ between the electrons in the i-th subband, notwithstanding the presence/absence of the real Fermi motion and the position of the subband bottom with respect to E_F. When the bottom of a subband is far below the Fermi level this definition of k_i (and of λ_i) recovers the definition used in Eq. (5.9). Following the results of Ref. [118], we can expect that the BCS-BEC crossover is approached in a given subband when

$1/\pi < k_i R_i < 2\pi$. In other words, the size of a condensed fermionic pair R_i becomes smaller than the mean distance between electrons in the corresponding subband. Having at our disposal this inequality, we can learn from Fig. 5.1(d), that the BCS-BEC crossover is definitely approached when the subband bottom approaches E_F, i.e., when $|\mu_i|/\hbar\omega_D \lesssim 1$. Here it is worth noting that, as seen from the inset in panel (d), the product $k_i R_i$ slightly increases with decreasing μ_i for $\mu_i < -0.2\hbar\omega_D$. This feature appears due to the presence of the ultraviolet cut-off and demonstrates that the regime of Eq. (5.12) is not reached in our calculations. The point is that Eq. (5.12) essentially assumes that $\hbar\omega_D \gg |\mu_i| \gg \Delta_i$ but this can not be realized for the parameters used to calculate the data of Fig. 5.1, i.e., for $\hbar\omega_D = 8.27\,\text{meV}$ and $\Delta_i = 1.08\,\text{meV}$. It is also of importance to note here that despite a significant shrinking in their lateral size down to λ_i, the condensed pairs of electrons do not suffer from the Coulomb repulsive effects. In metals such effects can be expected only for the separations smaller than 0.3-0.4 nm whereas in the subband whose bottom is in the vicinity of the Fermi level $\lambda_i \sim$ 5-10 nm, i.e., the mean density of electrons in the subband whose bottom approaches E_F is significantly smaller than the total mean electron density. We stress that this does not prevent this subband from making a significant contribution to coherent phenomena, see Sec. 5.3.

Based on the results of this section, we can conclude that the redistribution of the kinetic energy between the perpendicular and parallel spatial degrees of freedom leads to a significant reconstruction of the internal distribution of electrons in a condensed pair so that we find a clear molecule-like trend in the pairing. Here it is worth noting the paper by Eagles [72], that is well-known as one of the pioneering works on the BCS-BEC crossover. In this paper the author discussed the appearance of BEC features of fermionic pairs in a one-band system with low carrier concentration, where the chemical potential drops below the bottom of the band. Eagles also investigated the formation of uncondensed fermionic pairs in such a band. For instance, in the two-dimensional case this can happen for arbitrary small values of the coupling constant g. Here, the critical parameter is the ratio of the kinetic energy to the pairing energy. At low carrier concentrations the kinetic energy is depleted and, this ratio becomes small enough resulting in the BCS-BEC crossover. In Ref. [72] the chemical potential drops below the band bottom due to a substantial decrease in the density of charge carriers. In our case it occurs due to shifts of QWS's in energy, i.e., the quantum-size mechanism. This can be compared with the more familiar scenario of BCS-BEC crossover driven by a change in the coupling constant through a Feshbach resonance in atomic ultracold gases, see, e.g., Ref. [111].

We discussed the pair condensate in a subband whose bottom approaches the Fermi level. In total, we have a coherent superposition of different subband-dependent condensates. So, the question arises what happens to such a coherent mixture when approaching the BCS-BEC crossover condition in one of the available subbands. This point is addressed in the next section.

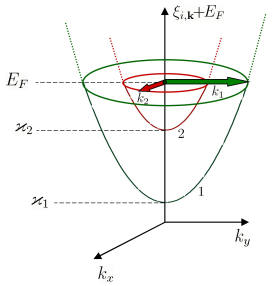

Fig. 5.2 (Color online) Sketch of the single-electron energy spectrum $\xi_{i,\mathbf{k}} + E_F$, with $\mathbf{k} = \{k_x, k_y\}$, for the lower (1) and upper (2) subbands in 4-5 ML lead single-crystalline nanofilms. Two thick arrows show the subband-dependent Fermi wavenumbers.

5.3 COHERENT MIXTURE OF SMALL AND LARGE CONDENSED FERMIONIC PAIRS

In the previous section we discussed the results for the fermionic condensate associated with one of the single-electron subbands appearing due to quantization of the perpendicular electron motion in the nanofilm. However, due to the presence of multiple subbands we have a coherent mixture of subband-dependent fermionic condensates each making a different contribution to the total condensate and superconducting characteristics. In nanofilms, due to the quasi-2D character of the electron motion, such contributions are, as a rule, almost equal to each other, except in the case when the subband bottom becomes significantly higher than $E_F - \hbar\omega_D$. In particular, when it approaches the level $E_F + \hbar\omega_D$, the corresponding subband stops to contribute due to the ultraviolet cut-off. The most interesting choice is realized when there are only two relevant subbands, which is the case for, e.g., lead nanofilms with thicknesses 4 and 5 ML (see the sketch given in Fig. 5.2). The optimal variant of tuning the subband positions is when the bottom of the upper subband is situated at $E_F - \hbar\omega_D$. First, the contribution of such a subband to the superconducting characteristics is almost the same as that of the lower subband with the bottom far below E_F. Second, the lateral size of the condensed fermionic pairs associated with the upper subband in this case only slightly increases as compared to $\mu_i = 0$, see Fig. 5.1(d). Our numerical results for this variant are shown in Fig. 5.3 for lead nanofilms with thicknesses 4 ML (the left panel) and 5 ML (the right panel). 1 ML corresponds to 0.286 nm in our calculations [119]. Here the quantity

$$w(R) = 1 - \frac{\iint\limits_{\rho<R} \mathrm{d}^3 r \mathrm{d}^3 r' \, |\langle \hat{\psi}_\uparrow(\mathbf{r}) \hat{\psi}_\downarrow(\mathbf{r}') \rangle|^2}{\iint \mathrm{d}^3 r \mathrm{d}^3 r' \, |\langle \hat{\psi}_\uparrow(\mathbf{r}) \hat{\psi}_\downarrow(\mathbf{r}') \rangle|^2}, \tag{5.13}$$

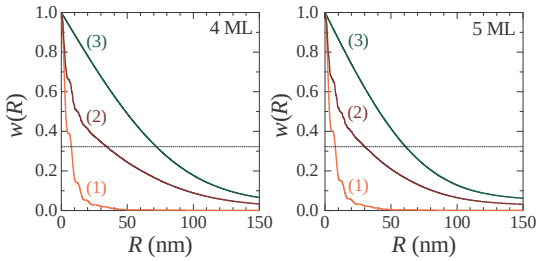

Fig. 5.3 (Color online) The probability of finding a Cooper pair with lateral size larger than R for Pb superconducting nanofilms with thickness 4 ML (the left panel) and 5 ML (the right panel). The results for a condensed fermionic pair in the upper subband are given by curve 1; the total probability for the both contributing subbands is represented by curve 2; the results for the Cooper pairs associated with the lower subband are given by 3. The Fermi level is adjusted so that the bottom of the upper of the two available subbands is at the energy $E_F - \hbar\omega_D$. The dotted line in both panels correspond to $w = 0.32$.

i.e., the probability of finding a Cooper pair with the lateral size larger than R, is plotted versus R. In both panels of Fig. 5.3 the different curves are for: (1), the results for the upper subband, whose bottom touches $E_F - \hbar\omega_D$ [when keeping only its contribution to Eq. (5.7)]; (2), the total results of both contributing subbands; and (3), the data for the lower single-electron subband whose bottom is far below E_F. Here the coupling constant g is chosen such that the experimental critical temperature T_c, as reported in Ref. [19], is obtained. For illustrative purposes, the confining interaction was taken as zero inside the nanofilm and infinite outside. The Fermi level E_F is adjusted so that to get the second QWS at $E_F - \hbar\omega_D$, i.e., $E_F = \varkappa_2 + \hbar\omega_D$. As seen from Fig. 5.3, the results for 4 ML and 5 ML are quite close to each other. If we adopt that the lateral diameter of the fermionic pair is defined by $w(R) = 0.32$ [recall that for the normal distribution $1 - \int_{-\sigma}^{+\sigma} \mathrm{d}\tau \rho_{\mathrm{norm}}(\tau) = 0.32$], then we find that the Cooper-pair radius associated with the lower subband is $R_{\mathrm{low}} = 72$ nm for 4 ML and 62 nm for 5 ML. The minor difference here is due to slightly different Fermi velocities (in the parallel direction) and critical temperatures. As for the pair radius for the upper subband, we obtain $R_{\mathrm{up}} = 7.6$ nm for (a) and $R_{\mathrm{up}} = 7.8$ nm for (b). These results are well explained by the trend given by Eq. (5.10), i.e., $R_{\mathrm{up}} \propto \hbar/\sqrt{m_e k_B T_c}$, with $T_c = 6.7$ K for 4 ML and 6.3 K for 5 ML (see Ref. [19]). For the total radius we have for curve (2) $R_{\mathrm{tot}} = 34$ nm for panel (a) and $R_{\mathrm{tot}} = 32$ nm for panel (b). The drop of R_{tot} as compared to the bulk-like result for the lower subband is due to the contribution of the extremely small pairs associated with the upper subband. It is worth noting that the introduction of the characteristic pair size for a coherent mixture of two different condensates is somewhat conventional. As seen from Fig. 5.3, curve (2) exhibits a bimodal behavior

with a clear crossover from the short-range regime governed by the upper band to the long-range one controlled by the lower band. Such a behavior can not be, of course, accurately specified by one characteristic length. This is in agreement with the recent analytical results for the extended Ginzburg-Landau formalism for multiband superconductors [110] and with numerical investigations of the coherent properties of MgB_2, see, e.g., Ref. [120, 121]. Thus, $R_{\rm tot}$ measures the short-to-long crossover in $w(R)$ rather than the size of a condensed fermionic pair. Nevertheless, the probability to pick up a condensed pair with lateral size smaller than $R_{\rm tot}$ is about 0.68. Moreover, as $w(R)$ decreases relatively slow around $R_{\rm tot}$, the probability to find a condensed pair with size smaller than 10 nm is about 0.5: almost half of the condensed fermionic pairs are smaller than 10 nm in lateral size.

What are the possible experimental evidences of such a shrinking of Cooper pairs in single-crystalline nanofilms? First of all, we remark that it is not an easy task to measure directly the Cooper-pair function and the related pair radius. This is possible for ultracold atomic condensates through rf-spectroscopy [122], but, to our knowledge, there are no similar measurements for solid-state systems. So, we need to rely upon indirect consequences of the BCS-BEC crossover in superconducting nanofilms. One possibility is to measure the characteristic length of the spatial variations of the superconducting order parameter $\Delta(\mathbf{r})$. It is well-known that for a single-band superconductor, such a characteristic length (also known as the healing length and, close to T_c, it approaches the Ginzburg-Landau coherence length) is almost proportional to the Cooper-pair size (i.e., to the BCS coherence length), and this proportionality becomes exact when approaching T_c. For two-band superconductors we have a more complex pattern when the spatial characteristic length of the pair condensate depends on the Cooper-pair radii of both subbands both band(subband) Cooper-pair radii, see, e.g., formulas (33) and (34) in Ref. [109]. However, what is of importance for us is that a drop in the Cooper-pair size in one of the available subbands will be accompanied by a drop in the spatial characteristic length of the superconducting order parameter. So, the profile of the order parameter in the core of the vortex will be sensitive to the presence of an admixture of extremely small Cooper pairs, which can be probed via scanning tunneling microscopy, see, e.g., Ref. [61]. In addition, Josephson physics and Andreev states will be also sensitive to a drop in the healing length of the condensate caused by the BCS-BEC crossover. In particular, this can be probed with hybrid superconducting devices similar to, e. g., a carbon nanotube joining a superconducting loop [123, 124]. In our case the single-crystalline metallic nanofilm will transmit the current between superconductors over mesoscopic distances (to keep the nanofilm in the normal state it is necessary to have the critical temperature of leads higher than that of the nanofilm).

Another interesting possibility is based on a competition of the spatial lengths associated with the subband-dependent condensates. It was recently shown that such a competition leads to the appearance of a long-range attrac-

tion between vortices in a two-band superconductor, see Ref. [125]. In this case the Abrikosov lattice of vortices formed in a perpendicular magnetic field will melt, resulting in the formation of stripes and clusters of vortices [107, 108]. The nonmonotonous interaction between vortices and patterns of their spatial distribution will be sensitive to the BCS-BEC crossover. Here the question can arise about the Josephson coupling between single-electron subbands in the superconducting nanofilm. Indeed, one may expect that large Josephson couplings can significantly reduce any difference between the subband-dependent condensates. Based on results of, e.g., Refs. [109, 110], one finds that the Josephson coupling in our case is controlled by the ratio $\Phi_{12}/(\Phi_{11}\Phi_{22}-\Phi_{12}^2)$, see the definition of $\Phi_{i'i}$ in Eq. (5.4). It can be estimated as 0.8 for nanofilms with two single-electron subbands and, for instance, this is significantly larger than the corresponding ratio, i.e., about 0.23, in the well-known two-band superconductor MgB_2, see Ref. [126]. However, it is difficult to say in advance if such a strong Josephson coupling will destroy any interplay between length scales of two subband-dependent condensates. The point is that a large ratio of the subband-dependent Fermi velocities (this is exactly our case) enhances significantly the difference between the subband-dependent length scales [126] and the corresponding attraction between vortices in a two-band superconductor [125]. Which of the two competing mechanisms prevails in the single-crystalline nanofilms, will be a subject of our future investigations. Note that the ratio of the subband-dependent Fermi velocities can be extremely large in the presence of a subband whose bottom is located just below the Fermi level.

One more interesting expectation related to the observations of the BCS-BEC-like crossover in single-crystalline metallic nanofilms is based on a proliferation of the pairing fluctuations for sufficiently small Cooper pairs. Such fluctuations can result in a pronounced suppression of the DOS at the Fermi level above the critical temperature [127, 128], i.e., in the appearance of the pseudogap behavior driven by the quantum-size induced BCS-BEC-like crossover. However, it is now difficult to say whether or not these pairing fluctuations make a contribution to the pseudogap-like behavior revealed recently in single-crystalline lead nanofilms which were found to depend on the nanofilm thickness [60]; other mechanisms can also be involved (see discussion in Ref. [60]) and, so, a comprehensive study is necessary. Last but not least, photoemission experiments can give information about the relevant quasiparticle spectrum that exhibits dramatic changes in the domain of the BCS-BEC crossover, see, for instance, Ref. [112].

5.4 CONCLUSIONS

In conclusion, we demonstrated that quantum confinement of the perpendicular motion of electrons in single-crystalline metallic superconducting nanofilms leads to the formation of a nanoscale multi-band(subband) superconductor.

The position in energy of each subband can vary significantly depending on the fabrication process, and it is possible that the bottom of one of such subbands is situated in the vicinity of the Fermi level. We showed that the character of the superconducting pairing in such a subband changes dramatically and exhibits a clear molecule-like trend, which is very similar to the BCS-BEC crossover but now driven by the perpendicular size-quantization.

Though we have considered the system in the clean limit, our results will also be relevant in the presence of a moderate disorder. The main issue for disorder in high-quality metallic superconducting nanofilms comes from the scattering of electrons at the interface between a substrate and the nanofilm, which leads to a broadening of the QWS levels. Though this will smoothen a drop in the lateral size of the Cooper pairs, our results given in Fig. 5.2(d) make it possible to expect that the effect in question will survive to a great extent until the broadening essentially exceeds 40 meV. Here it is worth noting that in experiments with lead nanofilms, the level broadening of QWS can be reduced, in the presence of a crystalline interface, down to 30-40 meV (at zero temperature and at energies close to E_F), see Ref. [129]. We would also like to note that the line width for the perpendicular discrete levels increases with temperature due to electron-phonon scattering. Though such an increase is not very pronounced for temperatures around T_c, i.e., it is of about 20 meV, see Ref. [129], this will cause an additional temperature-dependent smoothing. So, the optimal choice to probe the BCS-BEC-like crossover in single-crystalline nanofilms is to stay at nearly zero temperatures.

We would also like to highlight strong similarities between our findings and recent angle resolved photoemission results [112] for multiband superconducting iron-chalcogenide $FeSe_xTe_{1-x}$. It was found in Ref. [112] that the investigated sample of $FeSe_xTe_{1-x}$ does not lay deep in either the BCS or BEC regimes but lays instead in the BCS-BEC crossover domain. As demonstrated above, the same conclusion holds for 4 ML and 5 ML thick lead nanofilms when the bottom of one of the relevant single-electron subbands approaches E_F. Thus, one can in general conclude that multiband superconductors (both, bulk and with quantum-confined induced subbands, see also Refs. [23, 27, 91] and [95, 130]) offer new important possibilities towards a further understanding of the physics of the BCS-BEC crossover in solid-state materials.

Publications. The results presented in this chapter were published as:

- **Yajiang Chen**, A. A. Shanenko, A. Perali, and F. M. Peeters, *Superconducting nanofilms: molecule-like pairing induced by quantum confinement*, J. Phys.: Condens. Matter **24**, 185701 (2012).

6

Phonon mediated electron-electron coupling in Pb nanofilms

6.1 INTRODUCTION

Quantum-size effects on the excitation gap [20, 26] and the transition temperature [4, 5, 7] in superconducting ultrathin films have been a subject of study since Blatt and Thompson in 1963 predicted that the superconducting gap in ultrathin films oscillates as a function of the thickness [20]. Such oscillations are caused by the quantization of the electron motion in the direction normal to the film. In particular, the formation of discrete electron levels, i.e., the quantum well states (QWS) [18, 19], splits the three-dimensional (3D) conduction band into a series of two-dimensional (2D) subbands. The bottom of each subband is at the energy position of the corresponding QWS and so it is shifted down (up) when increasing (decreasing) the nanofilm thickness. When one of the QWS approaches the Fermi level, the density of the single-electron states at the Fermi level $N(0)$ increases, resulting in enhanced superconductivity.

Recently, superconducting Pb nanofilms have been intensively investigated experimentally where electronic effects are much stronger than effects due to strain. The critical temperature of atomically flat Pb nanofilms with thickness down to a few monolayers on a Si(111) substrate have been measured under different conditions [3–7, 13, 19]. It was found that superconductivity is not destroyed by fluctuations even when the thickness of the nanofilm is only a single monolayer [13], and the dependence of the critical temperature on thickness shows oscillations with a period close to two monolayers (ML) [3, 5], i.e., the even-odd staggering in the superconducting properties.

In addition to $N(0)$, the phonon-mediated coupling g between electrons also makes an important contribution to superconductivity. Large efforts [119,

131–133] have been made to understand how the formation of QWS can affect the electron mass-enhancement factor $\lambda \sim gN(0)$ [only in the weak-coupling limit $\lambda = gN(0)$]. Experimentally, from the information of the temperature dependence of the line widths of QWS in Ag films deposited on top of Fe(111) whisker, it was found that λ exhibits an overall decrease with increasing film thickness so that λ approaches its bulk value as $\approx 1/N$, where N is the number of monolayers [131]. The experimental study of λ in Pb(111) nanofilms on silicon showed that the mass-enhancement factor increases with increasing N. In both cases λ exhibits pronounced thickness-dependent oscillations. As it is mentioned above, a well-known reason for these oscillations is the variation of $N(0)$ with the nanofilm thickness. However, this is not the only important reason. There is an additional (less known) effect coming from thickness-dependent oscillations of the coupling g. The interplay of the oscillations of g and $N(0)$ is not well understood yet and often overlooked. The previous paper [26] initiated a study of such an interplay based on intuitive arguments and used an ansatz for the thickness dependent g. In the present Chapter we revisit the problem and develop a simple model to justify this ansatz and to analyze all the currently available experimental data of T_c versus film thickness. Our investigation is based on a numerical solution of the BdG equations. However, instead of solving the full BdG formalism [26]. we make use of the Anderson recipe for a very accurate approximate semi-analytical solution to the BdG equations: corrections to the Anderson approximation are less than a few percent for nanofilms. This will significantly simplify our numerical analysis.

This Chapter is organized as follows. In Sec. 6.2 we outline the BdG equations for a superconducting slab, including the basic moments concerning the Anderson approximation. In Sec. 6.3 we discuss our numerical results on the critical temperature in ultrathin superconducting nanofilms and highlight important aspects due to the interplay of the thickness-dependent oscillations of $N(0)$ and g. We demonstrate that this interplay is responsible for significant variations in the amplitude of the quantum-size oscillations of T_c from one experiment to another. Our conclusions are given in Sec. 6.4.

6.2 FORMALISM

6.2.1 Bogoliubov-de Gennes equations for a superconducting slab

Anderson's approximation assumes that the particle- and hole-like quasiparticle wave functions are proportional to the single-electron wave functions (see Sec. 1.2.3.2)

$$u_{i\mathbf{k}}(\mathbf{r}) = \mathcal{U}_{ik}\psi_{i\mathbf{k}}(\mathbf{r}), \quad v_{i\mathbf{k}}(\mathbf{r}) = \mathcal{V}_{ik}\psi_{i\mathbf{k}}(\mathbf{r}), \tag{6.1}$$

where $\mathcal{U}_{ik}$ and $\mathcal{V}_{ik}$ are multiplicative factors (real) and $\psi_{i\mathbf{k}}(\mathbf{r})$ is the single-electron wave function, i.e., $\hat{H}_e\psi_{i\mathbf{k}}(\mathbf{r}) = \xi_{ik}\psi_{i\mathbf{k}}(\mathbf{r})$. In the case of interest, i.e.,

for a superconducting slab, we have

$$\psi_{i\mathbf{k}}(\mathbf{r}) = \frac{\varphi_i(z)}{\sqrt{L_x L_y}} e^{i(k_x x + k_y y)}, \tag{6.2}$$

where $\varphi_i(z)$ is the QWS wave function and L_x, L_y are the dimensions of the unit cell used for the periodic boundary conditions in the x and y directions. For infinite confinement of electrons in the slab with thickness d ($L_x, L_y \gg d$) we have $\varphi_i(z) = \sqrt{2/d}\sin(\pi(i+1)z/d)$ and

$$\xi_{ik} = \frac{\hbar^2}{2m_e}\Big[\frac{\pi^2(i+1)^2}{d^2} + k^2\Big] - \mu. \tag{6.3}$$

Inserting Eq. (6.1) into Eq. (1.45) and introducing the subband-dependent gap [in the case of interest $\Delta(\mathbf{r}) = \Delta(z)$]

$$\Delta_i = \int \mathrm{d}z\, \varphi_i^2(z)\Delta(z), \tag{6.4}$$

we find a homogeneous system of two linear equations controlling $\mathcal{U}_{ik}$ and $\mathcal{V}_{ik}$. The determinant of the corresponding matrix should be equal to zero for a nontrivial solution, leading to $E_{ik} = \sqrt{\xi_{ik}^2 + \Delta_i^2}$. Then, by using the standard normalization condition $\mathcal{U}_{ik}^2 + \mathcal{V}_{ik}^2 = 1$, the BdG equations are reduced to the BCS-like self-consistency equation

$$\Delta_{i'} = \frac{1}{2}\int \frac{\mathrm{d}^2k}{(2\pi)^2} \sum_i \Phi_{i'i} \frac{\Delta_i}{E_{ik}} \tanh(\beta E_{ik}/2), \tag{6.5}$$

with the interaction-matrix element

$$\Phi_{i'i} = g\int \mathrm{d}z\, \varphi_{i'}^2(z)\varphi_i^2(z). \tag{6.6}$$

As T approaches the critical temperature T_c, E_{ik} reduces to the single-electron energy ξ_{ik} independent of Δ_i. Hence, at T_c Eq. (6.5) becomes a linear homogeneous system of equations for Δ_i that has a nontrivial solution when the corresponding determinant is zero, i.e.,

$$\det[M_{i'i} - \delta_{i'i}] = 0, \tag{6.7}$$

from which we obtain T_c. In Eq. (6.7)

$$M_{i'i} = \frac{m_e}{2\pi\hbar^2} \int\limits_{-\hbar\omega_D}^{\hbar\omega_D} \mathrm{d}\xi\, \theta(\xi - \varepsilon_i) \frac{\Phi_{ii'}}{2|\xi|} \tanh\big(\beta_c|\xi|/2\big), \tag{6.8}$$

with $\beta_c = 1/(k_B T_c)$ and $\varepsilon_i = \frac{\hbar^2}{2m_e}\frac{\pi^2(i+1)^2}{d^2} - \mu$. We note that a numerical solution of Eq. (6.7) is significantly faster than the procedure based on a numerical study of the BdG equations. The point is that Eq. (6.7) yields directly

the value of T_c. In contrast, to calculate T_c from the BdG equations, one first needs to find Δ_i as function of temperature. Then, T_c can be extracted from these data as the temperature above which there exists only zero solution for Δ_i. In addition, such a BdG-based numerical procedure of determining T_c is rather capricious in practice because at temperatures close to T_c convergence becomes rather slow and it is difficult to estimate an appropriate number of iterations to approach a solution. This often results in an overestimation of T_c that is larger than the corrections to the Anderson approximation, i.e., one more solid argument in favor of the present numerical scheme.

6.2.2 Quantum-size variations of the electron-electron coupling

In Sec. 6.2.1 it is assumed that the phonon mediated coupling of electrons g is not position dependent. It is true for bulk and a good approximation even for metallic nanofilms with thickness $d \gtrsim$ 10-20 nm (see our results below). However, this is not the case for ultrathin nanofilms due to significantly different (as compared to bulk) conditions for the lattice vibrations at the interface between the film and the semiconductor substrate. As we are interested in superconducting quantum-size oscillations typical for ultrathin metallic films, the question arises how our formalism should be modified to take account of this feature.

The coupling between electrons will depend on the proximity to the interface, i.e., $g = g(z)$. Deep in the film, $g(z)$ approaches the bulk coupling g_0. For Pb we take [35, 67] $g_0 N_{\rm bulk}(0) = 0.39$, with $N_{\rm bulk}(0)$ the bulk density of states at the Fermi energy. Approaching the interface, $g(z)$ is not equal to g_0 any longer but acquires a different value $g_{\rm if}$. Therefore, to first approximation we can replace $g(z)$ by the step function

$$g(z) = \begin{cases} g_{\rm if} & 0 \le z \le d_{\rm if}, \\ g_0 & d_{\rm if} < z \le d, \end{cases} \tag{6.9}$$

where $d_{\rm if}$ can be interpreted as the interface thickness. When introducing the spatial dependence of the coupling between electrons, Eq. (6.6) is replaced by

$$\Phi_{i'i} = \int \mathrm{d}z\, g(z)\, \varphi^2_{i'}(z)\varphi^2_i(z), \tag{6.10}$$

so that we obtain

$$\Phi_{i'i} \approx \frac{\bar{g}}{d}(1+\delta_{i'i}), \quad \bar{g} \approx \frac{1}{d}\int\limits_0^d \mathrm{d}z g(z). \tag{6.11}$$

As seen, to take into account the interface effect on the electron-electron effective coupling, one should replace g in all the relevant formulas in Sec. 6.2.1 by its spatially-averaged value $\bar{g}$ given by Eq. (6.11). Based on Eqs. (6.9) and

(6.11), we can find

$$\bar{g} = g_0 - \frac{d_{\rm if}(g_0 - g_{\rm if})}{aN}, \tag{6.12}$$

where a is the lattice constant in the direction of the film growth and N is the number of monolayers in the film ($d = aN$, and we take $a = 0.286\mathring{A}$ for Pb(111), see Ref. [119]). As seen from Eq. (6.12), the presence of the interface results in an extra contribution to $\bar{g}$ decaying with increasing thickness as $1/N$. This is typical of the surface effects whose relative contribution can be estimated as roughly proportional to the ratio of the whole surface area to the system volume. Such a contribution to the coupling was first reported in Ref. [131], where the electron-phonon mass enhancement parameter λ in Ag films grown on top of Fe(100) was experimentally studied and found to dependent on the film thickness. As known, $\lambda = gN(0)$ for $g \to 0$, with $N(0)$ the density of states, and λ is often called the (dimensionless) coupling constant. *Ab initio* DFT-calculations of λ also revealed the presence of the $1/N$-contribution, see, e.g., Refs. [131, 133]. Note that the well-known softening of the phonon modes due to surface effects (see, e.g., Ref. [86]) can be incorporated in a similar manner. Below we assume that all surface effects are included in $g_{\rm if}$. The same holds for effects due to a protective cover.

While g_0 is the film-material constant, $g_{\rm if}$ is not and changes from one experiment to another. Moreover, $g_{\rm if}$ varies also with changing nanofilm thickness because of quantum-size oscillations in the interface properties, see, for instance, theoretical results and discussion about the surface energy and the work function in nanofilms [119]. Generally, the quantum-size oscillations are controlled by a multiple-subband structure appearing in the single-electron spectrum due to the formation of QWS. Each time when the bottom of a subband (QWS) crosses μ, a shape (quantum-size) resonance appears [20] with a significant effect on the system characteristics. From Eq. (6.3) it is clear that the shape resonances are periodic with period half the Fermi wavelength $\lambda_F/2$. Thus, assuming that $g_{\rm if}$ exhibits thickness-dependent oscillations with period $\lambda_F/2$, Eq. (6.11) can be represented in the form

$$\bar{g} = g_0 - \frac{g_1(4\pi aN/\lambda_F)}{N}, \tag{6.13}$$

where $g_1(x)$ is a periodic function with $g_1(0) = g_1(2\pi)$. Below, in our numerical study of the BdG equations, we replace g in the formulas of Sec. 6.2.1 by $\bar{g}$ given by Eq. (6.13).

It is worth noting that one should distinguish oscillations of g from those of the electron-phonon mass enhancement parameter λ. As $\lambda \approx gN(0)$, there are two sources of quantum-size oscillations in λ, i.e., (i) the density of states that exhibits an increase each time when a new QWS crosses μ, and (ii) the phonon-mediated coupling g. The oscillations of λ are a known point that was investigated previously in experiments and in theoretical studies, see, e.g., Refs. [119, 131–133]. However, effects of the interplay of oscillations of $N(0)$ with those of g were not investigated and reported.

Experimentally measured values of the period of the quantum-size oscillations in Pb nanofilms are found to be very close to 2 ML. However, the period is not exactly 2 ML so that the even-odd staggering in the basic superconducting properties has phase-slip points where the phase of the even-odd oscillations changes by π. When $4a/\lambda_F = 1$, i.e., the period is equal to 2 ML, then we deal only with two parameters $g_1(\pi)$ and $g_1(2\pi)$ because $g_1(4\pi aN/\lambda_F)$ is equal to $g_1(\pi)$ for an odd number of monolayers and to $g_1(2\pi)$ for an even number of ML's. On the contrary, when $4a/\lambda_F$ is not an integer, we need to go into more detail about the dependence of g_1 on N. There is the possibility to overcome this problem by using, say, a "minimal scenario" when choosing the chemical potential such that the period of the quantum-size oscillations is exactly 2 ML. In this case we are able to limit ourselves to only two fitting parameters $g_1(\pi)$ and $g_1(2\pi)$. Therefore, our theoretical analysis will be restricted to the data between the phase-slip points where the effects of the mismatch between $\lambda_F/2$ and 2 ML can be neglected. Within such a minimal scenario, the parabolic band approximation used in Eq. (6.3) dictates that $\mu = 1.150\,\text{eV}$. It corresponds to λ_F being four times the single monolayer thickness a, i.e., $\lambda_F = 1.14\,\text{nm}$.

Now, we have everything at our disposal to check if the interplay between thickness-dependent oscillations of $N(0)$ and g can provide a solid understanding of the significant variations in the amplitude of the quantum-size oscillations of T_c found in different experiments.

6.3 RESULTS AND DISCUSSIONS

6.3.1 Brief review of experimental results on the T_c-oscillations

In Fig. 6.1 we show all reported sets of recent experimental data on the thickness dependence of T_c in ultrathin Pb(111) nanofilms on silicon. The data indicated by circles are from Ref. [3] and were obtained by *ex situ* resistivity measurements. Here Pb nanofilms were deposited on a Si(111) substrate (with the Si(111) $(7\times7)-$reconstruction) and covered by a protective Au layer with thickness 4 ML. This set of data exhibits clear even-odd quantum-size staggering for thicknesses of 22-28 ML. For smaller thicknesses there are only data for odd number of atomic layers, i.e., $N = 15$, 17, 19 and 21. A clear phase slip of π in the even-odd oscillations can be observed at $N = 22$ ML. At this point the even-odd staggering in T_c changes its trend: above the thickness $N = 22$ ML the critical temperature increases when passing from an odd number of monolayers to an even number, however it decreases from $N = 21$ ML to $N = 22$ ML. Below we will limit the analysis of this data-set to $N \geq 23$.

The results of Ref. [4] are given by stars and obtained from *ex situ* magnetic-susceptibility measurements for Pb films on Si(111) with the interface Si(111) $(\sqrt{3}\times\sqrt{3})$. The samples were protected by a Ge cap. The set includes data for films with an odd number of atomic layers $N = 5$, 7, 9, 11, 13 and with

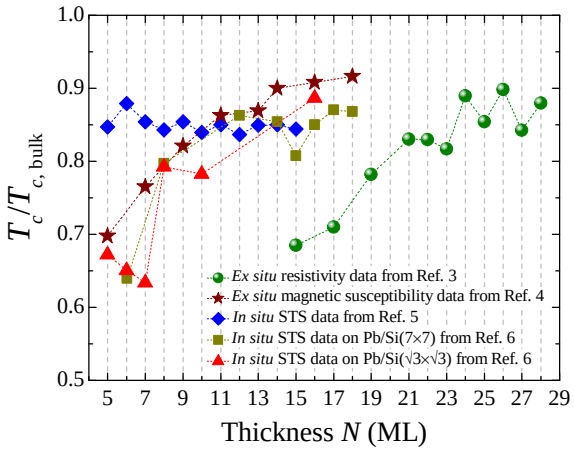

Fig. 6.1 (Color online) Experimental data on the thickness dependence of the critical temperature T_c of Pb nanofilms on Si(111) from different experiments.

even numbers $N = 14$, 16 and 18. Here it is not possible to obtain significant information about the even-odd oscillations of T_c: we can only compare the data for $N = 13$ and $N = 14$. As seen from this comparison, the increase of T_c from $N = 13$ to $N = 14$ is about two times smaller than the averaged amplitude of the even-odd oscillations observed in the previous set of data from Ref. [3].

The third experimental set of thickness dependent T_c (rhombuses, Ref. [5]) is for Pb nanofilms on the substrate Si(111)(7 × 7). Here the data were measured by *in situ* scanning tunneling spectroscopy. There was no protective layer covering the Pb film in this case. Clear signatures of even-odd quantum-size oscillations are visible down to thickness of 5 ML. However, the amplitude of these oscillations is about 2-3 times smaller than that of the first data-set [3]. It is worth noting that T_c of the third data set does not show an overall decrease with decreasing film thickness. It is seen that there are two points where the phase of the even-odd staggering of T_c slips by π, i.e., at $N = 6$ and at $N = 14$. For this set of data we will focus on the domain $7 \leq N \leq 13$.

The fourth (squares) and fifth (triangles) data sets are from the same group [6] and were measured by *in situ* scanning tunneling spectroscopy. They correspond to Pb nanofilms on a Si(111) substrate with reconstruction Si(111)(7 × 7) and Si(111)($\sqrt{3} \times \sqrt{3}$), respectively. The fourth set shows the even-odd staggering of T_c for $N = 14$-18. However, here the slip-point is situated at $N = 16$, which significantly reduces the number of points available for our analysis (below we work with data for $N \leq 15$). The fifth experimental set for T_c does not provide us with a clear pattern of even-odd oscillations.

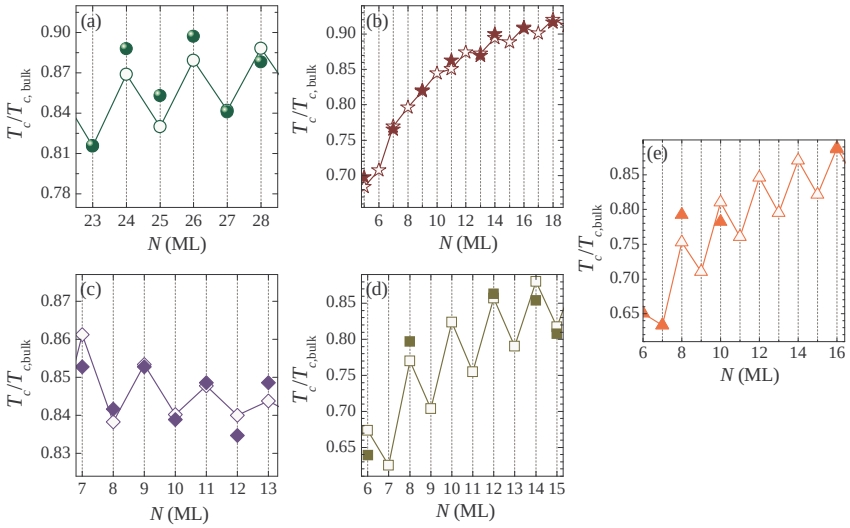

Fig. 6.2 (Color online) Theoretical results for the even-odd oscillations of T_c (open symbols) versus the experimental data (solid symbols): (a) theoretical data were calculated for $g_1(\pi) = 1.67g_0$ (odd numbers) and $g_1(2\pi) = 2.13g_0$, the experimental set is from Ref. [3]; (b) theoretical data were calculated for $g_1(\pi) = 0.64g_0$ (odd) and $g_1(2\pi) = 1.46g_0$ (even), experimental results are from Ref. [4]; (c) the same as in the previous panels but for $g_1(\pi) = -0.12g_{\mathrm{eff}}$ and $g_1(2\pi) = 0.84g_{\mathrm{eff}}$ (where $g_{eff}N_{\mathrm{bulk}}(0) = 0.36$) and the experimental set is from Ref. [5]; (d) the same as in previous panels but for $g_1(\pi) = 1.08g_0$ and $g_1(2\pi) = 1.54g_0$ and the experimental set is from Ref. [6] (for the interface Si(111)$(7 \times 7) - \mathrm{Pb}$); (e) the theoretical data were calculated for $g_1(\pi) = 1.05g_0$ and $g_1(\pi) = 1.59g_0$ and the experimental set is from Ref. [6] (for the interface Si(111)$(\sqrt{3} \times \sqrt{3}) - \mathrm{Pb}$).

Only from the data for film thicknesses $N = 5$, 6 and 7 we can guess that the amplitude of such oscillations is not pronounced. The phase-slip point of the even-odd staggering is visible at $N = 6$ (below we make a numerical fit to the data for $N \geq 7$). We note that the data of the fourth set are in significant variance with those of the third set in spite of the fact that the type of measurement and the substrate-film interface were similar in both experiments.

6.3.2 Impact of the thickness-dependent coupling between electrons

Results of our numerical analysis (open symbols) are given versus the experimental data (solid symbols) in Fig. 6.2. In panel (a) we compare our data with the T_c-values from the first set (Ref. [3]). Here we choose the range $N = 23$-28, i.e., above $N = 22$, the experimental phase-slip point of the even-odd oscillations in T_c (see the discussion in the previous section). Our calculations have been performed for $g_1(\pi) = 1.67g_0$ (odd numbers) and $g_1(2\pi) = 2.13g_0$ (even numbers), which yields good agreement with experiment. At first sight these values of g_1 seem too large to produce a deviation of only about 10%-20% from bulk. However, g_1/N is the correction to the electron-electron coupling rather than g_1. In particular, for $N = 20$ we obtain $g_1/N = 0.084g_0$ for odd numbers and $g_1/N = 0.11g_0$ for even numbers. It is worth noting that g_1 is larger for even numbers and so the resulting coupling $g_0 - g_1/N$ is smaller. However, T_c is generally larger for even numbers as compared to that for odd numbers in Fig. 6.1(a). The reason for this counterintuitive behavior is that there is an essential interplay between the even-odd oscillations in the density of states $N(0)$ and similar oscillations in the coupling g. In the case of panel (a) the drop in g for even N is fully overcome by an increase in $N(0)$ so that the product $gN(0)$ [$T_c \sim e^{-1/(gN(0))}$] slightly increases for even-number films and decreases for odd-number films.

Figure 6.2(b) shows our theoretical results versus the experimental data of the second set from Ref. [4]. Here we used the fitting parameters $g_1(\pi) = 0.64g_0$ (for odd numbers) and $g_1(2\pi) = 1.46g_0$ (for even numbers). As seen, g_1 for odd numbers is three times smaller than for even numbers but T_c does not exhibit any pronounced even-odd staggering. The explanation is again the interplay of the quantum-size variations of $N(0)$ with thickness-dependent oscillations in g: the effect of the difference between $g_1(\pi)$ and $g_1(2\pi)$ is almost compensated due to significant drops of $N(0)$ for even numbers of atomic layers. It is worth noting the surprisingly good agreement over the full range of experimental data.

Now we switch to the analysis of the third set of experimental data for T_c from Ref. [5]. These data are compared with our theoretical results in Fig. 6.2(c) for $N = 7$ ML to $N = 13$ ML (i.e., between the two phase-slip points $N = 6$ and $N = 14$). For this data-set T_c does not exhibit an overall decrease with decreasing N but oscillates around a value that is about 15% lower than the bulk critical temperature of 7.2 K. Even for $N = 50$ ML the

critical temperature was found to be about 15% smaller than in bulk. The bulk value of T_c and the superconducting energy gap were achieved only for relatively thick films with $N = 500\,\mathrm{ML}$. To incorporate this feature, we introduce a slightly smaller effective electron-phonon coupling constant g_{eff} which replaces the bulk coupling constant g_0. By choosing $g_{\mathrm{eff}} N_{\mathrm{bulk}}(0) = 0.36$, $g_1(\pi) = -0.12 g_{\mathrm{eff}}$ and $g_1(2\pi) = 0.84 g_{\mathrm{eff}}$, we compare our results (the open symbols) with the experimental critical temperature data (the solid symbols). As follows from Fig. 6.2(c), we again obtain very good agreement with the experimental data. As $g_1(\pi) < 0$, the total electron-phonon coupling constant $g_{\mathrm{eff}} - g_1/N$ for the odd-layered nanofilms is slightly above the effective-bulk value 0.36 and increases when decreasing N. This is totally different from our analysis of the previous data sets, and the direct consequence of this feature is that T_c does not show an overall decrease with decreasing nanofilm thickness. As seen, in this case the thickness-dependent oscillations of the electron-electron coupling "kills" such a decrease typical of the remaining experimental data sets. Note that the appearance of the positive interface-induced contribution to g for the odd-layered films, is not a surprise. For example, a similar effect was found for Ag films deposited on top of Fe(100) whisker.

Figures 6.2(d) and (e) show the comparison of our numerical data with data (the fourth and fifth sets, respectively) for T_c from Ref. [6]. For Pb nanofilms grown epitaxially on Si(111)(7×7) [panel (d)] we performed calculations with the fitting parameters $g_1(\pi) = 1.08 g_0$ and $g_1(2\pi) = 1.54 g_0$. For films with interface Si(111)$(\sqrt{3}\times\sqrt{3})-$Pb we used $g_1(\pi) = 1.05 g_0$ and $g_1(\pi) = 1.59 g_0$. For the fourth set we focus on the range below the phase slip point $N = 16$ ($N \leq 15$). For the fifth set we work above the phase-slip thickness $N = 6$ ($N \geq 7$). Here T_c increases for the even-layered nanofilms and decreases for the odd-layered ones for both data sets. However, similar to what was previously found for the first data set, the coupling $g_0 - g_1/N$ exhibits just the opposite size oscillations. As T_c follows the trend $\sim e^{-1/(gN(0))}$, one sees that the thickness-dependent oscillations of $N(0)$ are π-shifted with respect to the oscillations of g, but the increase of $N(0)$ has a more significant effect than the corresponding decreases of g for even number of MLs. It is interesting to note that the fourth and fifth experimental data-sets are characterized by almost the same coupling between electrons (the difference in g is less than 1%). So, for the experiments reported in Ref. [6], g is not sensitive to the change of Si(111) surface crystal ordering from (7×7) to $(\sqrt{3}\times\sqrt{3})$. Here the question arises why the results of Ref. [6] are so different with respect to those of Ref. [5]. One possible reason may be the difference in the quality of the silicon substrate which may have a significant impact on the interface phonons, as seen form the completely different values of g_1 found from our analysis in (c) and (d).

Note that the first and second data-sets in the present study were considered in our previous work [26]. However, in that paper time consuming calculations invoking the full BdG formalism were performed. As already

explained above (see the discussion after Eq. (6.7)), the full-BdG-based numerical procedure of determining the critical temperature often results in an overestimation of T_c that are larger than the errors of about a few percent induced by the Anderson approximation. This is reason why in the present work we have chosen to use the Anderson-approximation-based analysis of the available data, including the two data-sets considered previously in Ref. [26].

We also note that we did not discuss error bars for the experimental data in the present work because they do not influence our results qualitatively: the fitting parameters may be slightly different but the main conclusion about the crucial importance of the interplay of quantum-size oscillations of g and $N(0)$ will remain unaltered.

6.4 CONCLUSIONS

We have analyzed five experimental data-sets for the critical temperature of ultrathin Pb nanofilms deposited on top of Si(111). We have demonstrated that all these data sets can be reproduced within the BdG formalism by including the interface effect of the coupling. We addressed the important problem that the experimentally found amplitudes of the quantum-size oscillations of T_c vary significantly from one experiment to another. We showed that the reason for this difference is an interplay of the quantum-size variations in the single-electron density of states with the thickness-dependent oscillations in the phonon-mediated coupling between the electrons. Such oscillations of the coupling depends on the substrate material, the quality of the interface, the presence or absence of a protection cover and other fabrication details that change from one experiment to another. In addition, we demonstrated that oscillations in the coupling g and their interplay with the thickness-dependent variation of the density of states can even significantly change the overall trend of T_c with decreasing nanofilm thickness.

Publications. The results presented in this chapter were published as:

- **Yajiang Chen**, A. A. Shanenko, and F. M. Peeters, *Superconducting quantum-size oscillations in Pb nanofilms: Impact of the thickness-dependent oscillations of the phonon mediated electron-electron coupling*, Phys. Rev. B (accepted)..

7

Single vortex profile in two-band nanocylinders

7.1 INTRODUCTION

The superconducting properties of two-band MgB_2 [51] are of great interest and have been intensely studied. The particular character of MgB_2 is resulted from its two distinct types of electronic bonding, i.e., electron bands π and σ, which possess their own Fermi velocities, phonon-mediated electron-electron coupling in Pb nanofilms (i.e., Fermi velocities) and electron-electron couplings. When the temperature drops down to its unique critical temperature T_c, Cooper pairs formed from electrons of these bands exhibit two gap energies with $\Delta_\pi(0) = 2.2$ meV and $\Delta_\sigma(0) = 7.1$ meV [134–137]. From the BCS theory, the coherence lengths ξ of the π and σ bands at zero temperature are estimated to be about 51 nm and 13 nm, respectively, and the BCS coherence length of the π band matches the experimental result (49.6 ± 0.9 nm at 2 Kelvin) measured from the scanning tunneling spectroscopy [135]. Furthermore, the Ginzburg-Landau parameters κ of these two condensates show that the π component of the order parameter belongs to the type I superconductor, while the σ component is a type II superconductors. As a result, the single crystal MgB_2 reveals a vortex pattern [108] distinct from the cases in the intermediate state of type I superconductors and the Abrikosov lattice in type II superconductors.

The condensates in all bands are not independent because of the nonzero interband coupling, i.e., the superconducting order parameter of a certain band is not simply proportional to the Cooper-pair amplitude in this band but involves a sum over all band pairing amplitudes, each multiplied by a specific coefficient, i.e., the interband coupling constant, which depends on the material of the two-band superconductor. However, if the interband cou-

pling vanishes, we will face a superconducting system with two criticalities. In this case, the coherence lengths of both bands diverge at the relevant critical temperature. Thus, the interband coupling can be regarded as a source field controlling the appearance of two criticalities. In this Chapter, we investigate the influence of the interband coupling on the coherence length of the weak band through the numerical single-vortex solution to the two-band Bogoliubov-de Gennes (BdG) equations in a superconducting nanocylinder.

This Chapter is organized as follows. In Sec. 7.2, we represent the formalism of single-vortex solution (with winding number equal to 1) to the two-band BdG equation in a nanocylinder, as well as the formalism of solving the two-band BdG equation for bulk samples in the absence of vortex. In Sec. 7.3, besides the vortex profiles of both bands and the coherence length of the weak band in a two-band nanocylinder, the dependence of the bulk order parameter of the weak band on the interband coupling and the temperature is also shown and discussed. The conclusions are given in Sec. 7.4.

7.2 FORMALISM

7.2.1 Two-band Bogoliubov-de Gennes equations

The two-band BdG equations are written as

$$\begin{bmatrix} \hat{H}_i & \Delta_i(\mathbf{r}) \\ \Delta_i^*(\mathbf{r}) & -\hat{H}_i^* \end{bmatrix} \begin{bmatrix} u_{i\nu}(\mathbf{r}) \\ v_{i\nu}(\mathbf{r}) \end{bmatrix} = E_{i\nu} \begin{bmatrix} u_{i\nu}(\mathbf{r}) \\ v_{i\nu}(\mathbf{r}) \end{bmatrix}. \tag{7.1}$$

where i enumerate the two bands, ν stands for the set of relevant quantum numbers, $\Delta_i(\mathbf{r})$ is the order parameter, $u_{i\nu}(\mathbf{r})$ and $v_{i\nu}(\mathbf{r})$ are the quasiparticle wave functions, $E_{i\nu}$ is the quasiparticle energy, and

$$\hat{H}_i = \frac{1}{2m_e}\big(-i\hbar\nabla - \frac{e}{c}\mathbf{A}\big)^2 - \mu_i, \tag{7.2}$$

with m_e the electron band mass (set to the free electron mass), μ_i the chemical potential of a certain band measured from its bottom, and $\mathbf{A}$ the vector potential. The order parameter $\Delta_i(\mathbf{r})$ is given by

$$\Delta_i(\mathbf{r}) = \sum_{j\nu} g_{ij} u_{j\nu}(\mathbf{r}) v_{j\nu}^*(\mathbf{r}) \big[1 - 2f(E_{j\nu})\big], \tag{7.3}$$

where g_{ij} is the 2-by-2 coupling constant matrix with $g_{12} = g_{21}$, $f(E_{i\nu})$ is the Fermi distribution. The summation for every component of the order parameter is taken over the states which have single electron energy in the Debye window around the corresponding Fermi level.

Here we consider a nanocylinder with the radius $R = 300$ nm, and neglect the magnetic field in the single-electron Hamiltonian, i.e., we restrict ourselves in the approximation of the extreme type II superconductors. Due to the

chosen geometry, the cylindrical coordinates system is applied. And the single-electron Hamiltonian is rewritten as follows,

$$\hat{H}_i = -\frac{\hbar^2}{2m_e}\left[\frac{\partial^2}{\partial\rho^2} + \frac{1}{\rho}\frac{\partial}{\partial\rho} + \frac{1}{\rho^2}\frac{\partial^2}{\partial\varphi^2} + \frac{\partial^2}{\partial z^2}\right] - \mu_i. \tag{7.4}$$

Due to the assumption of an isolated vortex line with the winding number equal to one and the quantum confinement on the transverse boundary, the quasiparticle wave functions $u_{i\nu}(\mathbf{r})$ and $v_{i\nu}(\mathbf{r})$ are set to have a fixed phase difference, and their radio components are expanded in terms of the Bessel functions in radial direction,

$$u_{iJmk}(\mathbf{r}) = \bar{u}_{iJm}(\rho)\tfrac{1}{\sqrt{2\pi}}e^{i(m-1/2)\varphi}\tfrac{1}{\sqrt{L}}e^{ikz}, \tag{7.5}$$

$$v_{iJmk}(\mathbf{r}) = \bar{v}_{iJm}(\rho)\tfrac{1}{\sqrt{2\pi}}e^{i(m+1/2)\varphi}\tfrac{1}{\sqrt{L}}e^{ikz}, \tag{7.6}$$

with

$$\begin{aligned}
\bar{u}_{iJm}(\rho) &= \sum_{j=1}^{N} c_{ijJm}\phi_{j,m-1/2}(\rho),\\
\bar{v}_{iJm}(\rho) &= \sum_{j=1}^{N} d_{ijJm}\phi_{j,m+1/2}(\rho),\\
\phi_{j,m+1/2}(\rho) &= \frac{\sqrt{2}}{R\mathcal{J}_{m+3/2}(\alpha_{j,m+1/2})}\mathcal{J}_{m+1/2}\big(\alpha_{j,m+1/2}\frac{\rho}{R}\big).
\end{aligned} \tag{7.7}$$

In the above equations, m is half and odd integer, $\mathcal{J}_m(x)$ is the Bessel function of the first kind of the m-order, α_{jm} is the jth zero of this function, and c_{jJm} and d_{jJm} are real coefficients. By using Eq. (7.4) and the expansions of quasiparticle wave functions, the BdG Eq. (7.1) are reduced into the following form

$$\begin{bmatrix} \xi_i & \Delta_i \\ \Delta_i^{\hat{T}} & -\xi_i \end{bmatrix}\begin{bmatrix} c_{ijJm} \\ d_{ijJm} \end{bmatrix} = E_{i\nu}\begin{bmatrix} c_{ijJm} \\ d_{ijJm} \end{bmatrix}, \tag{7.8}$$

where $\hat{T}$ is the transposition operation of a matrix, and the matrix elements are given by

$$\begin{aligned}
\xi_{ijj'} &= \delta_{jj'}\left[\frac{\hbar^2}{2m_e}\left(\frac{\alpha_{j,m-1/2}^2}{R^2} + k^2\right) - \mu_i\right],\\
\Delta_{ijj'} &= \int \rho d\rho\, \phi_{j,m-1/2}(\rho)|\Delta_i(\rho)|\phi_{j',m+1/2}(\rho).
\end{aligned} \tag{7.9}$$

By inserting the expansions of $u_{i\nu}(\mathbf{r})$ and $v_{i\nu}(\mathbf{r})$ into Eq. (7.3), the order parameter is rewritten as

$$\begin{aligned}
\Delta_i(\rho,\varphi) &= \Delta_i(\rho)\, e^{-i\varphi}\\
&= \sum_{j\nu}\frac{g_{ij}}{2\pi L}\bar{u}_{j\nu}(\rho)\bar{v}_{j\nu}(\rho)\big[1-2f(E_{j\nu})\big]e^{-i\varphi},
\end{aligned} \tag{7.10}$$

where the order parameter in the radial direction $\Delta_i(\rho)$ is real. From Eq. (7.10), we can see that an isolated vortex line with the winding number equal to one has been constructed in the nanocylinder. Making use of Eqs. (7.9) and (7.10), the eigenvalue problem in Eqs. (7.8) is solved self-consistently.

7.2.2 Bulk solution of the two-band BdG equations

As a comparison to the single-vortex solution, the bulk solution is also of great important. Here we solve the bulk solution of the two-band BdG equations in the absence of the external magnetic field. In this case, the system keeps the translational symmetry, so the quasiparticle wave functions are set to be proportional to plane waves,

$$u_{i\mathbf{k}}(\mathbf{r}) = \widetilde{U}_{i\mathbf{k}}\sqrt{\frac{1}{\Omega}}e^{i\mathbf{k}\cdot\mathbf{r}}, \quad v_{i\mathbf{k}}(\mathbf{r}) = \widetilde{V}_{i\mathbf{k}}\sqrt{\frac{1}{\Omega}}e^{i\mathbf{k}\cdot\mathbf{r}}, \tag{7.11}$$

where Ω is the volume of a sample and i is the index of bands.

By inserting Eqs. (7.11) into the BdG Eqs. (7.1) and the expression of the order parameter Eq. (7.3), we have the spatial independent order parameter Δ_i for both bands. The quasiparticle energy and the temperature-dependent order parameter are given by

$$E_{i\mathbf{k}} = \sqrt{\xi_{i\mathbf{k}}^2 + \Delta_i^2} \tag{7.12}$$

$$\Delta_i = \frac{1}{\Omega}\sum_{j\mathbf{k}} g_{ij}\frac{\Delta_j}{2E_{j\mathbf{k}}}\big[1 - 2f(E_{j\mathbf{k}})\big], \tag{7.13}$$

where $\xi_{i\mathbf{k}} = \frac{\hbar^2}{2m_e}\mathbf{k}^2 - \mu_i$.

Moreover, Eq. (7.13) can be rewritten as follows

$$\begin{aligned} \Delta_1 &= g_{11}A_1\Delta_1 + g_{12}A_2\Delta_2, \\ \Delta_2 &= g_{21}A_1\Delta_1 + g_{22}A_2\Delta_2 \end{aligned} \tag{7.14}$$

with

$$A_i = \frac{1}{L^3}\sum_{\mathbf{k}}\frac{[1 - 2f(E_{i\mathbf{k}})]}{2E_{i\mathbf{k}}} = \frac{1}{2\pi^2}\int k^2 dk\frac{[1 - 2f(E_{i\mathbf{k}})]}{2E_{i\mathbf{k}}}. \tag{7.15}$$

The above linear equations result in an identical equation

$$(g_{11}A_1 - 1)(g_{22}A_2 - 1) = g_{12}^2 A_1 A_2, \tag{7.16}$$

from which the unique critical temperature T_c can be easily obtained due to the factor that when arriving at T_c the order parameters become zero and the quasiparticle energy is reduced into the single-electron energy, i.e., the only

variable appearing in Eq. (7.2.2) is T_c. When considering the approximation $\hbar\omega_D \gg k_B T_c$, the coefficients A_i read

$$A_i = \frac{1}{L^3}\sum_{\mathbf{k}} \frac{[1-2f(\xi_{i\mathbf{k}})]}{2\xi_{i\mathbf{k}}} = N_i(0) ln \frac{1.14\hbar\omega_D}{k_B T_c}, \tag{7.17}$$

where $N_i(0) = \frac{1}{4\pi^2}\left(\frac{2m_e}{\hbar^2}\right)^{\frac{3}{2}}\sqrt{\mu_i}$ is the density of states of one band at the Fermi surface μ_i. With this approximation, the solution to Eq, (7.14) is

$$ln\frac{1.14\hbar\omega_D}{k_B T_c} = \frac{(g_{11}N_1 + g_{22}N_2) \pm \sqrt{(g_{11}N_1 - g_{22}N_2)^2 + 4g_{12}^2 N_1 N_2}}{2(g_{11}g_{22} - g_{12}^2)N_1 N_2}. \tag{7.18}$$

This result is in agreement with that in Refs. [138] and [109] deduced from the weak-coupling approach of the Eilenberger equations. Between two solutions of T_c, normally the larger one corresponds to the critical temperature of the system, while the other is possibly a hidden criticality.

7.3 RESULTS AND DISCUSSION

In order to compare our results with the γGL equations, instead of g_{ij} we introduce $\lambda_{ii} = g_{ii}N(0)$ as the coupling constant (where $N(0) = \sum_i N_i(0)$) and a dimensionless parameter $\gamma = \lambda_{12}/(\lambda_{11}\lambda_{22})$ as the interband coupling. The parameters taken in the numerical calculations are shown in Table 7.1.

Table 7.1 Constant parameters used in the numerical calculations.

μ_1	μ_2	λ_{11}	λ_{22}	$\hbar\omega_D$
30 meV	80 meV	0.94	0.41	10 meV

In Fig. 7.1(a), the single-vortex profile of the order parameters of both bands is shown for the interband coupling $\gamma = 0.0002$ at zero temperature. The coherence lengths for both bands are defined by the horizontal dashed line in the figure which stands for the condition $\Delta_i(\rho = \xi_i) = 0.8\Delta_{i,\mathrm{bulk}}$, i.e., $\xi_1 = 14$ nm and $\xi_2 = 74$ nm. Such choice of the criteria is reasonable because it makes the coherence lengths of these two bands close to the uncoupled BCS coherence length at zero temperature. We can see that after the order parameters arrive at their bulk values, fast oscillations near the boundary $R = 300$ nm show up and finally drop to zero. The behavior of approaching the bulk order parameter is because the size of the sample is sufficiently large compared to the coherence lengths and the region with radius about 240 nm is equivalent to the place deep inside the superconductor, while the fast oscillations are resulted from the quantum confinement. Fig. 7.1(b) shows the temperature-dependent of the coherence length of the weak band for different

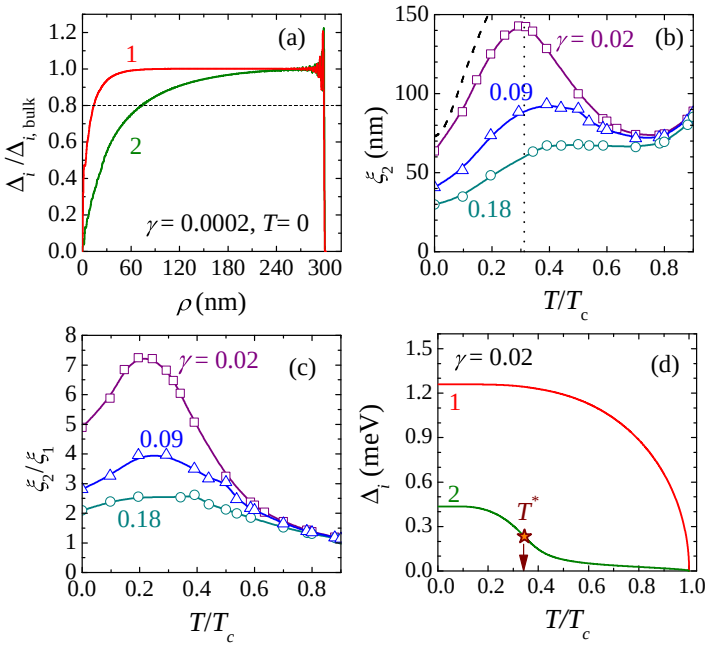

Fig. 7.1 (a) The single-vortex profile of a two-band nanocylinder as calculated for $\gamma = 0.0002$ at $T = 0$ K. The coherence lengths ξ_i defined by $\Delta_i(\rho = \xi_i) = 0.8\Delta_{i,\mathrm{bulk}}$ are $\xi_1 = 14$ nm and $\xi_2 = 74$ nm. (b) The coherence length of the weak band ξ_2 as a function of T/T_c for different γ. The dashed curve represents ξ_2 in the independent-band limit $\gamma \to 0$, and the dotted line marks $T_{c2} = 2.645$ K (for comparison, they are shown versus T/T_c with T_c calculated for $\gamma = 0.02$). (c) The ratio of the coherence lengths ξ_2/ξ_1 versus temperature. (d) The bandgaps versus temperature and the definition of the crossover temperature T^* (where ξ_2 reaches the maximum) extracted from the condition $\frac{\partial^2 \Delta_2}{\partial T^2} = 0$.

interband couplings. The dashed curve corresponds for the result of uncoupled case i.e., $\gamma = 0$, and the vertical dotted line labels the crossover temperature (T^*) where the maximum ξ_2 locates for $\gamma = 0.02$. With the chosen parameters for μ_i and λ_{ii}, the uncoupled critical temperature $T_{c2} = 2.645$ K is about one fourth of the T_c. As seen in this figure, at temperature close to T_{c2} there exists a peak in ξ_2. It becomes more pronounced with decreasing the γ, and the curve in the range from 0 to T_{c2} approaches to the curve of the case $\gamma = 0$. Although, the coherence length ($\xi_2 < 150$ nm) of the weak band is limited by the radius of the nanocylinder, Fig. 7.1(b) gives the clear signal of the existence of the hidden criticality at T_{c2} and $\gamma \to 0$. The ratio ξ_2/ξ_1 as a function of the of the temperature is shown in Fig. 7.1(c). As a result of the divergence behavior at temperature near T_{c2}, we also observe the most difference between these

two coherence lengths in the same temperature region when $\gamma \to 0$. At the temperature near to T_c, the coherence lengths of both bands diverge at the almost same speed. As seen in Figs. 7.1(b,c), with increasing coupling γ the temperature where ξ_2 peaks, labeled T^*, increases while the peak itself decreases (for the chosen parameters, the peak is washed out for $\gamma > 0.2$). It is interesting that T^* can be evaluated without a time-consuming numerical study of the vortex solution, being very close to the temperature at which $\partial^2\Delta_2/\partial T^2 = 0$ for a bulk superconductor. This is illustrated in Fig. 7.1(d) for $\gamma = 0.02$, where the inflection point of $\Delta_2(T)$ at $T = 0.33\ T_c$ matches well with $T^* = 0.31\ T_c$ found from the peak position in panel (b). In either case, T^* should be seen as the crossover temperature between the two regimes: lower temperatures - where Δ_2 is governed by the properties of the weaker band (for sufficiently small γ), and higher temperatures - where Δ_2 is controlled by the tunneling from the stronger band.

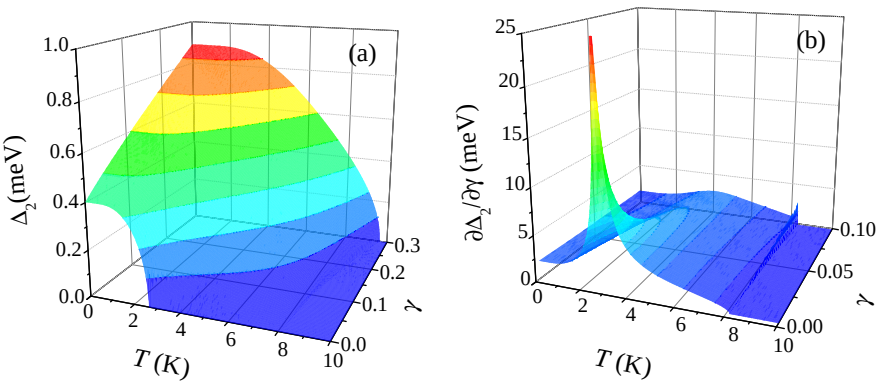

Fig. 7.2 (a) The order parameter Δ_2 of the weak band as a function of the temperature T and the interband coupling γ calculated from the two-band BdG equations for bulk. (b) The $\gamma-$susceptibility $\frac{\partial\Delta_2}{\partial\gamma}$ as a function of T and γ.

Now we discuss the numerical bulk solution of the two-band BdG equations. Fig. 7.2(a) shows that the increase in Δ_2 with γ becomes faster as T approaches $T_{c2} \approx 2.645$ K. In Fig. 7.2(b) we can see that at $T_c = T_{c2}$ the critical behavior of Δ_2 as a function of γ leads to a diverging $\gamma-$susceptibility, which also explains the divergence of ξ_2 at temperature close to T_{c2} and $\gamma \to 0$.

Finally, we briefly discuss available two-gap materials from the point of view of the hidden criticality. Based on the coupling constants available from Refs. [136, 139–142], we estimate the dimensionless coupling strength γ for various two-gap superconductors in Table 7.2. According to our calculations the best candidates to observe the effects associated with the hidden criticality seem to be V_3Si and $FeSe_{1-x}$ due to their particularly low values of coupling γ and low T^* and T_{c2} in comparison with the bulk T_c. This is supported by

Material	λ_{11}	λ_{22}	λ_{12}	$T_{c1}(K)$	$T_{c2}(K)$	$T^*(K)$	$T_c(K)$	γ	Ref.
MgB_2	1.88	0.5	0.21	38	3.9	14	39	0.22	[136]
OsB_2	0.39	0.29	0.0084	2.1	1.2	1.5	2.1	0.074	[139]
LiFeAs	0.63	0.642	0.061	17.7	6.7	(14)	18	0.15	[140]
V_3Si	0.566	0.472	0.0074	16.4	8.1	9	16.5	0.03	[141]
$FeSe_{1-x}$	0.482	0.39	0.001	8.3	3.1	3.2	8.3	0.005	[142]

Table 7.2 The coupling constants, calculated nominal critical temperatures T_{c1} and T_{c2} of the separate bands, the approximate crossover temperature T^*, the critical temperature T_c and the interband coupling γ for selected two-gap materials. The coupling constants are taken from the references in the last column of the table.

the experimentally observed anomalies close to T^* in these two materials, see Refs. [141, 142].

7.4 CONCLUSIONS

By solving the single-vortex solution of two-band BdG equations in a nanocylinder with sufficiently large radius, we obtained the profiles of both two components of the order parameter and the temperature-dependent coherence lengths for different interband coupling. We found that there exists an hidden criticality at the critical temperature of the weak band in the uncoupled case, and the interband coupling is the source field controlling the proximity to this critical point. In the vicinity of this point, the coherence length of the weak band in the nanocylinder diverges, and the bulk order parameter of the weak band shows a $\gamma-$susceptibility.

Publications. The results presented in this chapter were published as:

- L. Komendová, **Yajiang Chen**, A. A. Shanenko, M. V. Milošević, and F. M. Peeters, *Two-band superconductors: Hidden criticality deep in the superconducting state*, Phys. Rev. Lett. **108**, 207002 (2012).

Samenvatting

Recent hebben verscheidene ontwikkelingen in nano-fabricatie geleid tot supergeleidende metallische dunne nano-filmen en nano-draden van hoge kwaliteit. Door deze materialen uitermate zuiver te maken kon men verstrooiing dermate beperken dat de gemiddelde vrije weglengte van de elektronen even groot of groter dan de dikte van de systemen werd. In zulke situaties wordt de invloed van de quantum-mechanische opsluitingspotentiaal in de loodrechte (transversale) richting groot wat maakt dat de conductie-band in een aantal één-electron subbanden splitst. Dit resulteert in supergeleidende bekomen we een supergeleidende systemen die zich gedragen als meerbandssupergeleiders die modificeerbaar zijn op nano-schaal. Zulke systemen bieden nieuwe mogelijkheden door hun eigenschappen die sterk verschillen van elementaire bulk supergeleiders. In deze thesis, onderzoeken we de supergeleidende eigenschappen, en de invloed van quantum-mechanische opsluiting hierop, van metallische nano-draden (we beschouwen zowel nano-cilinders als holle nano-cilinders) en nano-filmen. In dit onderzoek wordt voornamelijk de zuivere limiet onder de loep genomen en de Bogoliubov-de Gennes vergelijkingen worden gehanteerd als basisformalisme. In het volgende overlopen we kort wat de voornaamste theoretische bevindingen van deze thesis zijn.

In **Hoofdstuk 1** geven we kort de historische achtergrond weer van het fenomeen supergeleiding en bespreken we de fenomenologische London vergelijkingen en het Ginzburg-Landau formalisme. Verder introduceren we het microscopisch formalisme van het Bardeen-Cooper-Schrieffer model en de veralgemening van dit model voor een ruimtelijk gemoduleerde orde parameter, gekend als de BdG vergelijkingen (samen met een spin-veralgemeende versie).

Numerieke methodes om de BdG vergelijkingen op te lossen worden hier ook in detail besproken. In het laatste gedeelte van dit Hoofdstuk worden twee belangrijke wijzen van nano-fabricatie beschreven, namelijk, molecuulbundel-epitaxie en lift-off lithografie, alsook wordt scanning tunneling spectroscopie besproken.

In **Hoofdstuk 2** nemen we een nano-cilinder als model voor een metallische supergeleidende nano-draad om de invloed van een positie-afhankelijke Hartree-Fock potentiaal, op de distributie van de supergeleidende orde parameter $\Delta(\mathbf{r})$ en de kritische transitie-temperatuur T_c, te bestuderen. In een bulk supergeleider is de Hartree-Fock potentiaal onafhankelijk van de positie zodat de één-electron energiën en de chemische potentiaal een vergelijkbare invloed ondervinden. Omdat $\Delta(\mathbf{r})$ and en T_c afhangen van de één-electron energiën gemeten vanaf de chemische potentiaal, blijven deze onveranderd onder ompolen van de Hartree-Fock interactie. Dit is niet het geval voor nano-supergeleider. We tonen aan dat, in tegenstelling tot een bulk supergeleider, in de aanwezigheid van een quantum-mechanische opsluitingspotentiaal de positie-afhankelijke Hartree-Fock potentiaal resulteert in een verschuiving van de systeem-afhankelijke oscillaties van de kritische temperatuur (alsook van de bandkloof en de orde parameter uitgemiddeld over de posities) naar grotere diameters.

In **Hoofdstuk 3** onderzoeken we hoe een quantum-opsluitingspotentiaal de supergeleiding beïnvloed in een holle metallische nano-cilinder. De radiale kuantisatie door de opsluitingspotentiaal in een holle nano-cilinder leidt tot de splitsing van de conductie-band in meerdere subbanden die verschuiven in energie als de binnenste straal R, van de dikte van de cilinderwand d, aangepast worden. Een dergelijke bandenstructuur met meerdere subbanden zorgt voor quantum supergeleidende oscillaties, zo zullen bijvoorbeeld de supergeleidende eigenschappen variëren met d bij een vaste R. Verder vinden we dat de karakteristieke eigenschappen van deze variaties kwalitatief verandert als R groter dan een bepaalde waarde komt: het onregelmatige patroon van supergeleidende resonanties wordt periodisch. De reden voor deze transitie is de verandering van de rol dat de centrifugale energie speelt. Wanneer R vergroot, verkleint deze energie zodanig dat de een-elektron subbanden, dewelke verschillende waarden voor het azimutaal quantumnummer in absolute waarde $|l|$ (maar met hetzelfde radiaal quantumnummer j) bezitten, bijna ontaard zijn in energie . Dit leidt tot bundels van subbanden die verantwoordelijk zijn voor de equidistante resonanties in de fundamentele supergeleidende grootheden als funktie van d. We tonen aan dat de vorming van de subbanden verder kan leiden tot meerdere supergeleidende bandkloven, door interactie tussen quantum opsluiting en het mechanisme van Andreev-reflectie. Het verschil tussen deze subband-afhankelijke supergeleidende bandkloven is groot in het onregelmatige regime, maar ze worden bijna gelijk in het regime van periodische resonanties. Daar is de verhouding van de kritische temperatuur over de bandkloof bijna gelijk aan de bulk-waarde, terwijl in het onregelmatige regime deze gereduceerd wordt met 20%-30% door de Andreev-toestanden. De rol die

de Andreev-toestanden, veroorzaakt door de quantum opsluitingspotentiaal, spelen is belangerijk bij kleine binnenste straal R, maar wordt verwaarloosbaar in het regelmatige regime.

In **Hoofdstuk 4** onderzoeken we een ander interessant fenomeen dat door een opsluitingspotentiaal geïntroduceerd wordt, namelijk een cascade struktuur van transities tussen de supergeleidende en normale toestand. Meer bepaald onderzoeken we de cascades veroorzaakt door een parallel aangelegd magnetisch veld in een metallische holle nano-cilinder. Hierbij richten we ons op de invloed van de geometrische vorm van de opsluitingspotentiaal, de thermische 'smoothing', en de interactie tussen de spin en het magnetisch veld. Wanneer de binnenste straal R en de dikte van de cilinderwand d worden gevariëerd dan vinden we dat er een kwalitatieve verandering optreedt in de cascades als we van het nano-draad regime, d.i., $R/d \ll 1$, naar het nanofilm regime, d.i., $d \ll R$, gaan. Terwijl in het geval dat $R/d \ll 1$, de cascade sterker benadrukt wordt, worden de cascade sprongen in de orde parameter, als funktie van het extern aangelegd magnetisch veld, in het andere regime, $R \gg d$, sterk gereduceerd. De reden voor het glad worden van de cascade voor grote R is dat het vergroten van R ervoor zorgt dat er meer één-electron subbanden een bijdrage leveren aan de orde parameter. Hierdoor wordt de relatieve bijdrage van elke subband kleiner en het process van ontparing in één van de beschikbare subbanden wordt niet meer vergezeld door een discrete sprong: de cascade wordt glad.

Eveneens vonden we dat bij toenemende temperatuur een aanzienlijke gladstrijking van de sprongetjes optreedt in de cascades. De reden hiervoor verschilt. Bij eindige temperaturen zijn er reeds in de afwezigheid van een magnetisch veld tekenen van ontparing, dwz. thermisch-geactiveerde ontparing. Daarom worden effecten van bijkomstige ontparingsmechismen, bv. door het magneetveld, verzwakt.

We observeerden ook dat het mee in rekening brengen van de interactie tussen spin en magneetveld het aantal kleine sprongetjes in een cascade doet toenemen, wat te wijten is aan de spin-Zeeman splitsing in de quasideeltjesenergie. De spin-magneetveldinteractie splitst elke quasideeltjesvertakking in twee delen, die, als regel, de initiële en uitgesproken sprong opdeelt in twee kleinere. In de meeste gevallen is het kritische magneetveld kleiner in de aanwezigheid van de spin-magneetveldinteractie. Soms echter, door de complexe wisselwerking van de orbitale spin-magneetveld effecten, kan het kritische magneetveld verhoogd worden. Door de significante orbitale beweging in een holle nanocylinder, vonden we dat het paramagnetisch-begrensde veld $H_{\rm par}$ in essentie groter is dan $H_{c,||}$, wanneer berekend inclusief orbitale en spinmagnetische momenten. Dit kan verschillen voor minder symmetrische opsluitingsgeometrieën, bv. voor een nanodraad met een rechthoekige doorsnede. Van het paramagnetisch begrensde veld $H_{\rm par}$ is aangetoond dat het oscilleert met R en d door kwantumschaaleffecten: op de maxima neemt $H_{\rm par}$ beduidend toe vergeleken met bulk Clogston-Chandrasekhar veld H^{CC}. Zoals geweten is, kan de spin-baan koppeling [55] de effecten van paramagnetische paarbrek-

ing verminderen. Echter, door een geringe bijdrage van het paramagnetische mechanisme, is de rol van spinbaankoppeling niet essentieel in ons systeem.

In **Hoofdstuk 5** wordt getoond hoe kwantumopsluiting voor de loodrechte beweging van elektronen in enkelvoudig kristallijne metallische supergeleidende films leidt tot de vorming van een multiband(subband) supergeleider. De energie positie van elke subband kan sterk variëren naargelang het fabricatieproces, en het is mogelijk dat de onderkant van één van dergelijke subbanden zich in de nabijheid van het Fermi-niveau bevindt. Voor Pb nanofilms met een dikte van 4 en 5 monolagen, vonden we een spectaculair scenario: tot de helft van alle Cooperparen krimpen in hun laterale afmetingen (evenwijdig aan de film) tot enkele nanometers, d.w.z. dat het supergeleidende condensaat een coherente mix wordt van de bijna molecuulachtige fermionparen met de gewone zwakgebonden en uitgebreide Cooperparen. Zulk een molecuulachtige fermionische paring is gelijkaardig aan die gerealiseerd in de BCS-BEC crossover. Hier is het effect echter een gevolg van de kwantisatie t.g.v. de opsluiting.

In **Hoofdstuk 6** analyseerden we de beschikbare experimentele datasets van de dikte-afhankelijkheid van de kritische temperatuur in ultradunne Pb nanofilms afgezet op een Si(111) substraat. De analyse was gebaseerd op een numerieke studie van de BdG vergelijkingen, voorzien van een eenvoudige theorie van de dikte-afhankelijke elektron-elektronkoppeling. Meer specifiek richtten we ons tot het belangrijke probleem dat de experimenteel gevonden amplitudes van de kwantum-grootte oscillaties in T_c significant variëren van het ene experiment tot het andere. We vonden dat de reden voor zo een verschil de competitie is van de kwantum-grootte variaties in de een-elektrontoestandsdichtheid bij het Ferminiveau met de dikte-afhankelijke oscillaties in de fononen-gemediëerde koppeling tussen elektronen. De oscillaties van de koppeling zijn afhankelijk van het type van meting, het substraatmateriaal, de kwaliteit van het tussenvlak, de aan- of afwezigheid van een beschermingslaag en andere fabricatiedetails die veranderen van experiment tot experiment.

In **Hoofdstuk 7** werd een een-vortex oplossing beschouwd voor een tweeband s-golf supergeleider die kwantumopgesloten werd in een cylinder met een straal van ongeveer de Ginzburg-Landau coherentielengte. We onderzochten hoe de verschillende genezingslengtes van de twee bandcondensaten veranderen met de interband Josephson-achtige koppeling γ en hoe het Kramer-Pesch-effect gevoelig is aan kwantumopsluiting. We vonden dat het supergeleidende gedrag van een tweebandsysteem beïnvloed wordt door een verborgen kritikaliteit diep in de supergeleidende toestand, nl. bij de kritische temperatuur van de zwakkere band beschouwd als een onafhankelijk supergeleidend systeem. In de nabijheid van dit punt, vertoont de genezingslengte van de zwakkere band een erg uitgesproken piek als functie van de temperatuur. De grootte van de piek schaalt als $\propto \gamma^{-\mu}$, met de Landau kritische exponent $\mu = \frac{1}{3}$, gelijk aan die gevonden voor het gemiddeld-veld kritische gedrag ten opzichte van het bronveld in ferromagnetisme en ferroelektriciteit. De ver-

borgen kritikaliteit in twee(multi)band supergeleiders kan dus experimenteel geobserveerd worden door bv. beeldvorming van de variaties van de vortexkern over een breder temperatuursbereik. Gelijkaardige effecten worden verwacht voor supergeleidende multilagen.

Summary

Recent advances in nanofabrication technology resulted in high-quality superconducting metallic nanofilms and nanowires. It was possible to minimize disorder so that in most fabricated samples, the electron mean-free path was estimated to be about or even larger than the specimen thickness. In this case the effects of quantum confinement for the perpendicular (transverse) electron motion are not washed out by impurity scattering, and the conduction band splits up into a series of single-electron subbands. As a result, such superconducting systems become quantum-engineered multi-band superconductors and promise a plethora of interesting phenomena that are completely different as compared to bulk elemental superconductors. In the present thesis, we investigated the superconducting properties of metallic nanowires (we considered nanocylinders and hollow nanocylinders) and nanofilms as governed by quantum confinement. The investigation was focused on the clean limit and based on the Bogoliubov-de Gennes equations. In what follows, we summarize the theoretical findings of the present thesis.

In **Chapter 1** we briefly outlined the history of the superconductivity and discussed the phenomenological London equations and Ginzburg-Landau approach. Furthermore, we introduced the microscopic formalism from the Bardeen-Cooper-Schrieffer model to its generalization for spatially modulated order parameter, i.e., the BdG equations (together with the spin-generalized version). Numerical approaches to a solution of the BdG equations were also discussed in detail. In the last part of this chapter, two important methods of nanofabrication, i.e., molecular beam epitaxy and lift-off lithography, were

described, and important insight into scanning tunneling spectroscopy was provided.

In **Chapter 2** we took a nanocylinder as a prototype of a metallic superconducting nanowire to investigate the effect of a spatially-dependent Hartree-Fock potential on the distribution of the superconducting order parameter $\Delta(\mathbf{r})$ and the critical transition temperature T_c. In a bulk superconductor, the Hartree-Fock potential is position-independent and gives the same contribution to both the single-electron energies and the chemical potential. As $\Delta(\mathbf{r})$ and T_c depend on the single-electron energies measured from the chemical potential, they remain unaltered when switching the Hartree-Fock interaction. This is no longer the case for nanoscale superconductors. Unlike a bulk superconductor, we showed that in the presence of quantum confinement the spatially Hartree-Fock potential results in a shift of the the size-dependent oscillations of the critical temperature (and also of the energy gap and the spatially-averaged order parameter) to larger diameters.

In **Chapter 3** we explored how quantum confinement can modify superconductivity in a hollow metallic nanocylinder. The radial quantization of the electron motion in the hollow nanocylinder results in a splitting of the conduction band into a series of subbands whose lower edges move in energy when changing the inner radius R and thickness d. Such a multi-subband structure leads to pronounced quantum-size superconducting oscillations e.g., the superconducting properties varies with d at a fixed R. We found that the character of these variations changes qualitatively with an increase in R: the irregular pattern is replaced by almost equidistant superconducting resonant enhancements. The reason for such a crossover is the change of the role of the centrifugal energy. When R increases, this energy is diminished so that single-electron subbands with different absolute values of the azimuthal quantum number m (but with the same radial quantum number j) are nearly degenerate in energy. As a result, they form bundles of subbands responsible for equidistant resonant enhancements in the basic superconducting quantities as functions of d. We showed that the formation of subbands can result in multiple superconducting gaps due to the interplay between quantum confinement and the Andreev-reflection mechanism. The difference between the subband-dependent superconducting gaps is significant in the irregular regime but they are almost equal when coming to the regular side of the crossover. Here the ratio of the critical temperature to the energy gap approaches its bulk value while it is reduced by 20%-30% due to Andreev-type states in the irregular regime. The role of Andreev-type states induced by quantum confinement is significant for small inner radii but becomes minor in the regular domain.

In **Chapter 4** we explored another interesting phenomenon developing in the presence of quantum confinement, i.e., a cascade structure of the superconducting-to-normal transition. In particular, we investigated the cascades driven by the parallel magnetic field in a metallic hollow nanocylinder. The special focus was on the confining geometry, thermal smoothing

and spin-magnetic-field interactions. Varying the inner radius R and its wall thickness d, we observed a qualitative change in the cascades when passing from the nanowire-like regime, i.e., $R/d \ll 1$, to the nanofilm-like regime, i.e., $d \ll R$. While being pronounced for $R/d \ll 1$, the cascade jumps in the order-parameter as function of an external parallel magnetic field are significantly smoothed for $R \gg d$. The reason for this smoothing is that an increase in R results in a significant increase of the number of the single-electron subbands that contribute to the order parameter. Hence, the relative contribution of each subband becomes strongly reduced and, as a result, the depairing in one of the available subbands is not accompanied by a discontinuous jump any more: the cascade structure is smoothed out.

It has also been found that a considerable smoothing of jumps in the cascades occurs when increasing temperature. The reason for this is different. At finite temperatures there are signatures of the depairing already at zero magnetic field, i.e., the thermally-activated depairing. Therefore, effects of any additional depairing mechanism, e.g., due to the magnetic field, are weakened.

We also observed that taking into account the spin-magnetic-field interaction increases the number of small jumps in a cascade, which is due to the spin-Zeeman splitting in the quasiparticle energy. The spin-magnetic-field interaction splits each quasiparticle branch in two parts, which, as a rule, divides the initial pronounced jump in two smaller ones. In most cases the critical magnetic field is smaller in the presence of the spin-magnetic-field interaction. However, sometimes, due to the complex interplay of the orbital and spin-magnetic-field effects, the critical magnetic field can be enhanced. Due to significant orbital motion in a hollow nanocylinder, we found that the paramagnetic-limiting field $H_{\rm par}$ is essentially larger than $H_{c,||}$ calculated when including orbital and spin magnetic moments. This can be different for less symmetric confining geometries, e.g., for a rectangular-cross-section nanowire. The paramagnetic limiting field $H_{\rm par}$ has been shown to oscillate with R and d due to the quantum-size effects: at maxima $H_{\rm par}$ is significantly enhanced as compared to the bulk Clogston-Chandrasekhar field H^{CC}. The spin-orbit coupling, as is known [55], can reduce effects of the paramagnetic pair breaking. However, due to a minor contribution of the paramagnetic mechanism, the role of spin-orbit coupling will not be essential in our system.

In **Chapter 5** quantum confinement for the perpendicular motion of electrons in single-crystalline metallic superconducting nanofilms has been demonstrated to lead to the formation of a nanoscale multi-band(subband) superconductor. The position in energy of each subband can vary significantly depending on the fabrication process, and it is possible that the bottom of one of such subbands is situated in the vicinity of the Fermi level. For Pb nanofilms with thickness of 4 and 5 monolayers, we found a spectacular scenario: up to half of all the Cooper pairs nearly collapse, shrinking in the lateral size (parallel to the nanofilm) down to a few nanometers, i.e., the superconducting condensate will be a coherent mixture of almost molecule-like fermionic pairs with the ordinary loosely-bound and extended Cooper pairs. Such molecule-

like fermionic pairing is similar to that realized in the BCS-BEC crossover. However, the effect is now driven by the size quantization.

In **Chapter 6** we analyzed the available experimental data sets on the thickness dependence of the critical temperature in ultrathin Pb nanofilms deposited on a Si(111) substrate. The analysis was based on a numerical study of the BdG equations equipped with a simple theory of the thickness dependent electron-electron coupling. In particular, the important problem has been addressed that the experimentally found amplitudes of the quantum-size oscillations in T_c vary significantly from one experiment to another. We found that the reason for such a difference is an interplay of the quantum-size variations in the single-electron density of states at the Fermi level with the thickness-dependent oscillations in the phonon-mediated coupling between electrons. The oscillations of the coupling depend on the substrate material, the quality of the interface, the presence or absence of a protection cover and other fabrication details that change from one experiment to another.

In **Chapter 7** a single-vortex solution has been considered for a two-band s-wave superconductor that is quantum-confined in a cylinder with the radius of about the Ginzburg-Landau coherence length. We investigated how the different healing lengths of the two band condensates change with inter-band Josephson-like coupling γ and how the Kramer-Pesch effect is sensitive to quantum confinement. We found that the superconducting behavior of a two-band system is influenced by a hidden criticality deep in the superconducting state, i.e., at the critical temperature of the weaker band taken as an independent superconducting system. In the vicinity of this point, the healing length of the weaker band exhibits a well pronounced peak as a function of temperature. The magnitude of the peak scales as $\propto \gamma^{-\mu}$, with the Landau critical exponent $\mu = \frac{1}{3}$, the same as found for the mean-field critical behavior with respect to the source field in ferromagnets and ferroelectrics. Thus, the hidden criticality in two(multi)-band superconductors can be experimentally observed by e.g., imaging of the variations of the vortex core in a broader temperature range. Similar effects are expected for the superconducting multilayers.

Outlook

This thesis investigated the effect of quantum confinement on superconducting properties in clean metallic nanocylinders and nanofilms by numerically solving the Bogoliubov-de Gennes equations. Future work beyond this thesis may include the following aspects:

1. Consider more complex boundary profile of nanowires. In such case, the surface roughness can be investigated in more details and the model will be more practical. Moreover, such samples may exhibit distinctive superconductivity due to the complex quantum confinement.

2. Consider the effect of an electrostatic field on nanoscale superconductivity. The superconducting properties of nanostructures can be tuned by applying an electrostatic field which controls electron density distribution.

3. Consider the effect of impurities and pinning on nanoscale superconductivity. Such problems are of interest because impurities and pinning in clean metallic nanostructures change the constitution of the sample. The interplay between quantum confinement and the impurities/pinning may lead to novel superconducting properties.

4. Consider the stability of giant vortex structure in superconducting Pb nano-islands under an external magnetic field. Recently, Pb nano-islands have been fabricated and giant vortex states were observed in such systems. It is also of great interest to investigate the Andreev states located in the center of the vortex core.

Bibliography

1. E. Rotenberg, H. Koh, K. Rossnagel, H. W. Yeom, J. Schäfer, B. Krenzer, M. P. Rocha, and S. D. Kevan, Phys. Rev. Lett. **91**, 246404 (2003).
2. M. M. Özer, J. R. Thompson, and H. H. Weitering, Phys. Rev. B **74**, 235427 (2006).
3. Y. Guo, Y.-F. Zhang, X.-Y. Bao, T.-Z. Han, Z. Tang, L.-X. Zhang, X.-G. Zhu, E. G. Wang, Q. Niu, Z. Q. Qiu, J.-F. Jia, Z.-X. Zhao, Q.-K. Xue Science **306**, 1915 (2004).
4. M. M. Özer, J. R. Thompson, and H. H. Weitering, Nat. Phys. **2**, 173 (2006).
5. D. Eom, S. Qin, M.-Y. Chou, and C. K. Shih, Phys. Rev. Lett. **96**, 027005 (2006).
6. C. Brun, I.-P. Hong, F. Patthey, I. Y. Sklyadneva, R. Heid, P. M. Echenique, K. P. Bohnen, E. V. Chulkov, and W.-D. Schneider, Phys. Rev. Lett. **102**, 207002 (2009).
7. M. M. Özer, Y. Jia, Z. Zhang, J. R. Thompson, and H. H. Weitering, Science **316**, 1594 (2007).
8. M. Tian, J. Wang, J. S. Kurtz, Y. Liu, M. H. W. Chan, T. S. Mayer, and T. E. Mallouk, Phys. Rev. B **71**, 104521 (2005).
9. M. Zgirski, K.-P. Riikonen, V. Touboltsev, and K. Arutyunov, Nano Lett. **5**, 1029 (2005).

10. F. Altomare, A. M. Chang, M. R. Melloch, Y. Hong, and C. W. Tu, Phys. Rev. Lett. **97**, 017001 (2006).

11. M. Savolainen, V. Touboltsev, P. Koppinen, K.-P. Riikonen, and K. Arutyunov, Appl. Phys. A **79**, 1769 (2004).

12. N. A. Court, A. J. Ferguson, and R. G. Clark, Supercond. Sci. Technol. **21**, 015013 (2008).

13. T. Zhang, P. Cheng, W.-J. Li, Y.-J. Sun, G. Wang, X.-G. Zhu, K. He, L. Wang, X. Ma, X. Chen, Y. Wang, Y. Liu, H.-Q. Lin, J.-F. Jia, Q.-K. Xue, Nat. Phys. **6**, 104 (2010).

14. C. N. Lau, N. Markovic, M. Bockrath, A. Bezryadin, and M. Tinkham, Phys. Rev. Lett. **87**, 217003 (2001).

15. M. Zgirski and K. Y. Arutyunov, Phys. Rev. B **75**, 172509 (2007).

16. L. Jankovič, D. Gournis, P. N. Trikalitis, I. Arfaoui, T. Cren, P. Rudolf, M.-H. Sage, T. T. M. Palstra, B. Kooi, J. D. Hosson, M. A. Karakassides, K. Dimos, A. Moukarika, T. Bakas, Nano Lett. **6**, 1131 (2006).

17. Z.-L. Guan, Y.-X. Ning, C.-L. Song, J. Wang, J.-F. Jia, X. Chen, Q.-K. Xue, and X. Ma, Phys. Rev. B **81**, 054516 (2010).

18. J. J. Paggel, T. Miller, and T.-C. Chiang, Science **283**, 1709 (1999).

19. S. Qin, J. Kim, Q. Niu, and C.-K. Shih, Science **324**, 1314 (2009).

20. J. M. Blatt and C. J. Thompson, Phys. Rev. Lett. **10**, 332 (1963).

21. X.-Y. Bao, Y.-F. Zhang, Y. Wang, J.-F. Jia, Q.-K. Xue, X. C. Xie, and Z.-X. Zhao, Phys. Rev. Lett. **95**, 247005 (2005).

22. A. A. Shanenko, M. D. Croitoru, R. G. Mints, and F. M. Peeters, Phys. Rev. Lett. **99**, 067007 (2007).

23. A. A. Shanenko, M. D. Croitoru, and F. M. Peeters, Phys. Rev. B **78**, 024505 (2008).

24. A. A. Shanenko, M. D. Croitoru, M. Zgirski, F. M. Peeters, and K. Arutyunov, Phys. Rev. B **74**, 052502 (2006).

25. A. A. Shanenko and M. D. Croitoru, Phys. Rev. B **73**, 012510 (2006).

26. A. A. Shanenko, M. D. Croitoru, and F. M. Peeters, Phys. Rev. B **75**, 014519 (2007).

27. A. A. Shanenko, M. D. Croitoru, A. Vagov, and F. M. Peeters, Phys. Rev. B **82**, 104524 (2010).

28. H. K. Onnes, Comm. Phys. Lab. Univ. Leiden **12**, 120 (1911).

29. V. V. Schmidt, "The Physics of Superconductors" (Springer, 1997).

30. W. Meissner and R. Ochsenfeld, Naturwissen. **21**, 787 (1933).

31. F. London and H. London, Proc. Roy. Soc. A **149**, 71 (1935).

32. M. Tinkham, "Introduction to superconductivity" (McGraw-Hill, Inc., 1996).

33. V. L. Ginzburg and L. D. Landau, Zh. Eksp. Teor. Fiz. **20**, 1064 (1950).

34. J. Bardeen, L. N. Cooper, and J. R. Schrieffer, Phys. Rev. **108**, 1175 (1957).

35. P. G. de Gennes, "Superconductivity of Metals and Alloys" (Benjamin, New York, 1966).

36. H. F. Hess, R. B. Robinson, R. C. Dynes, J. M. Valles, and J. V. Waszczak, Phys. Rev. Lett. **62**, 214 (1989).

37. A. A. Abrikosov, Sov. Phys. JETP **5**, 1174 (1957).

38. U. Essmann and H. Trauble, Phys. Lett. **24A**, 526 (1967).

39. B. D. Josephson, Phys. Lett. **1**, 251 (1962).

40. P. W. Anderson and A. H. Dayem, Phys. Rev. Lett. **13**, 195 (1964).

41. J. G. Bednorz and K. A. Müller, Z. Phys. B **64**, 189 (1986).

42. M. K. Wu, J. R. Ashburn, C. J. Torng, P. H. Hor, R. L. Meng, L. Gao, Z. J. Huang, Y. Q. Wang, and C. W. Chu, Phys. Rev. Lett. **58**, 908 (1987).

43. H. Maeda, Y. Tanaka, M. Fukutomi, and T. Asano, Jpn. J. Appl. Phys. **27**, L209 (1988).

44. Z. Z. Sheng and A. M. Hermann, Nature (London) **332**, 138 (1988).

45. C. W. Chu, L. Gao, F. Chen, Z. J. Huang, R. L. Meng, and Y. Y. Xue, Nature (London) **365**, 323 (1993).

46. L. Gao, Y. Y. Xue, F. Chen, Q. Xiong, R. L. Meng, D. Ramirez, C. W. Chu, J. H. Eggert, and H. K. Mao, Phys. Rev. B **50**, 4260 (1994).

47. P. W. Anderson, P. A. Lee, M. Randeria, T. M. Rice, N. Trivedi, and F. C. Zhang, J. Phys.: Condens. Matter **16**, R755 (2004).

48. Z. K. Tang, L. Zhang, N. Wang, X. X. Zhang, G. H. Wen, G. D. Li, J. N. Wang, C. T. Chan, and P. Sheng, Science **292**, 2462 (2001).

49. J. L. Sarrao, L. A. Morales, J. D. Thompson, B. L. Scott, G. R. Stewart, F. Wastin, J. Rebizant, P. Boulet, E. Colineau, and G. H. Lander, Nature (London) **420**, 297 (2002).

50. F. Wastin, P. Boulet, J. Rebizant, E. Colineau, and G. H. Lander, J. Phys.: Condens. Matter **15**, S2279 (2003).

51. J. Nagamatsu, N. Nakagawa, T. Muranaka, Y. Zenitani, and J. Akimitsu, Nature (London) **410**, 63 (2001).

52. S. P. Kelty, C.-C. Chen, and C. M. Lieber, Nature (London) **352**, 223 (1991).

53. Y. Kamihara, H. Hiramatsu, M. Hirano, R. Kawamura, H. Yanagi, T. Kamiya, and H. Hosono, J. Am. Chem. Soc. **128**, 10012 (2006).

54. W. Yi, C. Zhang, L. Sun, Z.-a. Ren, W. Lu, X. Dong, Z. Li, G. Che, J. Yang, X. Shen, X. Dai, Z. Fang, Z. Zhao, Europhys. Lett. **84**, 67009 (2008).

55. J. B. Ketterson and S. N. Song, "Superconductivity" (Cambrige, 1999).

56. A. A. Shanenko, M. D. Croitoru, and F. M. Peeters, Europhys. Lett. **76**, 498 (2006).

57. P. W. Anderson, J. Phys. Chem. Solids **11**, 26 (1959).

58. N. Tombros, L. Buit, I. Arfaoui, T. Tsous, D. Gournis, P. N. Trikalitis, S. J. van der Molen, P. Rudolf, and B. J. van Wees, Nano Lett. **8**, 3060 (2008).

59. T. Nishio, T. An, A. Nomura, K. Miyachi, T. Eguchi, H. Sakata, S. Lin, N. Hayashi, N. Nakai, M. Machida, Y. Hasegawa, Phys. Rev. Lett. **101**, 167001 (2008).

60. K. Wang, X. Zhang, M. M. T. Loy, T.-C. Chiang, and X. Xiao, Phys. Rev. Lett. **102**, 076801 (2009).

61. T. Cren, D. Fokin, F. m. c. Debontridder, V. Dubost, and D. Roditchev, Phys. Rev. Lett. **102**, 127005 (2009).

62. A. Y. Cho and J. R. Arthur, Prog. Solid State Chem. **10**, 157 (1975).

63. Y.-S. Fu, S.-H. Ji, X. Chen, X.-C. Ma, R. Wu, C.-C. Wang, W.-H. Duan, X.-H. Qiu, B. Sun, P. Zhang, J.-F. Jia, Q.-K. Xue, Phys. Rev. Lett. **99**, 256601 (2007).

64. A. Bezryadin and P. M. Goldbart, Adv. Mater. **22**, 1111 (2010).

65. J. E. Han and V. H. Crespi, Phys. Rev. B **69**, 214526 (2004).

66. I. Grigorenko, J.-X. Zhu, and A. Balatsky, J. Phys.: Condens. Matter **20**, 195204 (2008).

67. A. L. Fetter and J. D. Walecka, "Quantum Theory of Many-Particle Systems" (Dover Publications, 2003).

68. A. A. Shanenko, M. D. Croitoru, and F. M. Peeters, Phys. Rev. B **78**, 054505 (2008).

69. R. A. Hein, J. W. Gibson, R. Mazelsky, R. C. Miller, and J. K. Hulm, Phys. Rev. Lett. **12**, 320 (1964).

70. J. F. Schooley, W. R. Hosler, and M. L. Cohen, Phys. Rev. Lett. **12**, 474 (1964).

71. J. F. Schooley, W. R. Hosler, E. Ambler, J. H. Becker, M. L. Cohen, and C. S. Koonce, Phys. Rev. Lett. **14**, 305 (1965).

72. D. M. Eagles, Phys. Rev. **164**, 489 (1967).

73. E. A. Ekimov, V. A. Sidorov, E. D. Bauer, N. N. Mel'nik, N. J. Curro, J. D. Thompson, and S. M. Stishov, Nature (London) **428**, 542 (2004).

74. Y. Takano, M. Nagao, I. Sakaguchi, M. Tachiki, T. Hatano, K. Kobayashi, H. Umezawa, and H. Kawarada, Appl. Phys. Lett. **85**, 2851 (2004).

75. E. Bustarret, C. Marcenat, P. Achatz, J. Kačmarčik, F. Lévy, A. Huxley, L. Ortéga, E. Bourgeois, X. Blase, D. Débarre, J. Boulmer, Nature (London) **444**, 465 (2006).

76. A. J. Leggett, Progr. Theor. Phys. **36**, 901 (1966).

77. Y. Tanaka, J. Phys. Soc. Jpn. **70**, 2844 (2001).

78. Y. Tanaka, Phys. Rev. Lett. **88**, 017002 (2001).

79. A. Gurevich and V. M. Vinokur, Phys. Rev. Lett. **90**, 047004 (2003).

80. E. Babaev, Phys. Rev. Lett. **89**, 067001 (2002).

81. E. Babaev, J. Jäykkä, and M. Speight, Phys. Rev. Lett. **103**, 237002 (2009).

82. K. Czajka, M. M. Maśka, M. Mierzejewski, and Z. Śledź, Phys. Rev. B **72**, 035320 (2005).

83. V. Vakaryuk, Phys. Rev. Lett. **101**, 167002 (2008).

84. F. Loder, A. P. Kampf, and T. Kopp, Phys. Rev. B **78**, 174526 (2008).

85. G. Schwiete and Y. Oreg, Phys. Rev. Lett. **103**, 037001 (2009).

86. D. G. Naugle, J. W. Baker, and R. E. Allen, Phys. Rev. B **7**, 3028 (1973).

87. K. Tanaka and F. Marsiglio, Phys. Rev. B **62**, 5345 (2000).

88. A. M. Garcia-Garcia, J. D. Urbina, E. A. Yuzbashyan, K. Richter, and B. L. Altshuler, Phys. Rev. Lett. **100**, 187001 (2008).

89. J. D. Shore, M. Huang, A. T. Dorsey, and J. P. Sethna, Phys. Rev. Lett. **62**, 3089 (1989).

90. K. Y. Arutyunov, D. S. Golubev, and A. D. Zaikin, Phys. Rep. **464**, 1 (2008).

91. Y. Chen, M. D. Croitoru, A. A. Shanenko, and F. M. Peeters, J. Phys.: Condens. Matter **21**, 435701 (2009).

92. P. C. Canfield and G. W. Crabtree, Phys. Today **56**, 34 (2003).

93. J. Paglione and R. L. Greene, Nat. Phys. **6**, 645 (2010).

94. E. H. Hwang, S. Das Sarma, and M. A. Stroscio, Phys. Rev. B **61**, 8659 (2000).

95. D. Innocenti, N. Poccia, A. Ricci, A. Valletta, S. Caprara, A. Perali, and A. Bianconi, Phys. Rev. B **82**, 184528 (2010).

96. A. M. Clogston, Phys. Rev. Lett. **9**, 266 (1962).

97. Y. Chen, A. A. Shanenko, and F. M. Peeters, Phys. Rev. B **81**, 134523 (2010).

98. F. M. Peeters, M. D. Croitoru, and A. A. Shanenko, Physica C **468**, 593 (2008).

99. V. A. Schweigert and F. M. Peeters, Phys. Rev. B **57**, 13817 (1998).

100. O. S. Lutes, Phys. Rev. **105**, 1451 (1957).

101. J. Bardeen, Rev. Mod. Phys. **34**, 667 (1962).

102. M. D. Croitoru, A. A. Shanenko, C. C. Kaun, and F. M. Peeters, Phys. Rev. B **80**, 024513 (2009).

103. M. D. Croitoru, V. N. Gladilin, V. M. Fomin, J. T. Devreese, W. Magnus, W. Schoenmaker, and B. Soree, J. Appl. Phys. **93**, 1230 (2003).

104. S. Jin, M. V. Fischetti, and T.-W. Tang, J. Appl. Phys. **102**, 083715 (2007).

105. A. Bezryadin, J. Phys.: Condens. Matter **20**, 043202 (2008).

106. H. H. Weitering, ChemPhysChem **10**, 3183 (2010).

107. E. Babaev and M. Speight, Phys. Rev. B **72**, 180502 (2005).

108. V. Moshchalkov, M. Menghini, T. Nishio, Q. H. Chen, A. V. Silhanek, V. H. Dao, L. F. Chibotaru, N. D. Zhigadlo, and J. Karpinski, Phys. Rev. Lett. **102**, 117001 (2009).

109. V. G. Kogan and J. Schmalian, Phys. Rev. B **83**, 054515 (2011).

110. A. A. Shanenko, M. V. Milošević, F. M. Peeters, and A. V. Vagov, Phys. Rev. Lett. **106**, 047005 (2011).

111. I. Bloch, J. Dalibard, and W. Zwerger, Rev. Mod. Phys. **80**, 885 (2008).

112. Y. Lubashevsky, E. Lahoud, K. Chashka, D. Podolsky, and A. Kanigel, Nat. Phys. **8**, 309 (2012).

113. A. Toschi, M. Capone, and C. Castellani, Phys. Rev. B **72**, 235118 (2005).

114. D. N. Basov, A. V. Chubukov, Nat. Phys. **7**, 272 (2011).

115. P. Pieri and G. C. Strinati, Phys. Rev. Lett. **91**, 030401 (2003).

116. N. N. Bogoliubov, "Lectures on Quantum Statistics" (Gordon and Breach, New York, 1970).

117. A. Y. Cherny and A. A. Shanenko, Phys. Rev. B **60**, 1276 (1999).

118. F. Pistolesi and G. C. Strinati, Phys. Rev. B **49**, 6356 (1994).

119. C. M. Wei and M. Y. Chou, Phys. Rev. B **66**, 233408 (2002).

120. A. E. Koshelev and A. A. Golubov, Phys. Rev. Lett. **90**, 177002 (2003).

121. A. E. Koshelev and A. A. Golubov, Phys. Rev. Lett. **92**, 107008 (2004).

122. C. H. Schunck, Y. Shin, A. Schirotzek, and W. Ketterle, Nature (London) **454**, 739 (2008).

123. J.-D. Pillet, C. H. L. Quay, P. Morfin, C. Bena, A. L. Yeyati, and P. Joyez, Nat. Phys. **6**, 965 (2010).

124. W. Belzig, Nat. Phys. **6**, 940 (2010).

125. M. Silaev and E. Babaev, Phys. Rev. B **84**, 094515 (2011).

126. L. Komendová, M. V. Milošević, A. A. Shanenko, and F. M. Peeters, Phys. Rev. B **84**, 064522 (2011).

127. A. Perali, P. Pieri, G. C. Strinati, and C. Castellani, Phys. Rev. B **66**, 024510 (2002).

128. A. Perali, P. Pieri, L. Pisani, and G. C. Strinati, Phys. Rev. Lett. **92**, 220404 (2004).

129. I.-P. Hong, C. Brun, F. Patthey, I. Y. Sklyadneva, X. Zubizarreta, R. Heid, V. M. Silkin, P. M. Echenique, K. P. Bohnen, E. V. Chulkov, W.-D. Schneider, Phys. Rev. B **80**, 081409 (2009).

130. A. Perali, A. Bianconi, A. Lanzara, and N. L. Saini, Solid State Comm. **100**, 181 (1996).

131. D.-A. Luh, T. Miller, J. J. Paggel, and T.-C. Chiang, Phys. Rev. Lett. **88**, 256802 (2002).

132. Y.-F. Zhang, J.-F. Jia, T.-Z. Han, Z. Tang, Q.-T. Shen, Y. Guo, Z. Q. Qiu, and Q.-K. Xue, Phys. Rev. Lett. **95**, 096802 (2005).

133. J. Noffsinger and M. L. Cohen, Phys. Rev. B **81**, 214519 (2010).

134. G. Rubio-Bollinger, H. Suderow, and S. Vieira, Phys. Rev. Lett. **86**, 5582 (2001).

135. M. R. Eskildsen, M. Kugler, S. Tanaka, J. Jun, S. M. Kazakov, J. Karpinski, and O. Fischer, Phys. Rev. Lett. **89**, 187003 (2002).

136. A. A. Golubov, J. Kortus, O. V. Dolgov, O. Jepsen, Y. Kong, O. K. Andersen, B. J. Gibson, K. Ahn, and R. K. Kremer, J. Phys.: Condens. Matter **14**, 1353 (2002).

137. M. Iavarone, G. Karapetrov, A. E. Koshelev, W. K. Kwok, G. W. Crabtree, D. G. Hinks, W. N. Kang, E.-M. Choi, H. J. Kim, H.-J. Kim, S. I. Lee, Phys. Rev. Lett. **89**, 187002 (2002).

138. V. G. Kogan, C. Martin, and R. Prozorov, Phys. Rev. B **80**, 014507 (2009).

139. Y. Singh, A. Niazi, M. D. Vannette, R. Prozorov, and D. C. Johnston, Phys. Rev. B **76**, 214510 (2007).

140. H. Kim, M. A. Tanatar, Y. J. Song, Y. S. Kwon, and R. Prozorov, Phys. Rev. B **83**, 100502 (2011).

141. Y. A. Nefyodov, A. M. Shuvaev, and M. R. Trunin, Europhys. Lett. **72**, 638 (2005).

142. R. Khasanov, M. Bendele, A. Amato, K. Conder, H. Keller, H.-H. Klauss, H. Luetkens, and E. Pomjakushina, Phys. Rev. Lett. **104**, 087004 (2010).

Appendix A

Abbreviations

- AC: Alternating current
- BCS: Bardeen-Cooper-Schrieffer
- BdG: Bogoliubov-de Gennes
- DC: Direct current
- DOS: Density of states
- GL: Ginzburg-Landau
- HF: Hartree-Fock
- LDOS: Local density of states
- MBE: Molecular beam epitaxy
- MEG: Magnetoencephalography
- ML: Monolayer
- MRI: Magnetic resonance imaging
- NMR: Nuclear magnetic resonance
- QWS: Quantum well states

- RHEED: Reflection high energy electron diffraction
- SQUID: Superconducting quantum interference device
- STM: Scanning tunneling microscope
- STS: Scanning tunneling spectroscopy
- TEM: Transmission electron microscope

Appendix B

List of publications

1. **Yajiang Chen**, Mauro M. Doria, and F. M. Peeters, *Vortices in a mesoscopic cone: A superconducting tip in the presence of an applied field*, Phys. Rev. B **77**, 054511 (2008).
2. **Yajiang Chen**, M. D. Croitoru, A. A. Shanenko, and F. M. Peeters, *Superconducting nanowires: quantum confinement and spatially dependent Hartree-Fock potential*, J. Phys.: Condens. Matter **21**, 435701 (2009).
3. **Yajiang Chen**, A. A. Shanenko, and F. M. Peeters, *Hollow nanocylinder: Multisubband superconductivity induced by quantum confinement*, Phys. Rev. B **81**, 134523 (2010).
4. **Yajiang Chen**, A. A. Shanenko, A. Perali, and F. M. Peeters, *Superconducting nanofilms: molecule-like pairing induced by quantum confinement*, J. Phys.: Condens. Matter **24**, 185701 (2012).
5. **Yajiang Chen**, A. A. Shanenko, M. D. Croitoru, and F. M. Peeters, *Quantum cascades in nano-engineered superconductors: geometrical, thermal and paramagnetic effects*, J. Phys.: Condens. Matter (accepted).
6. **Yajiang Chen**, A. A. Shanenko, and F. M. Peeters, *Superconducting quantum-size oscillations in Pb nanofilms: Impact of the thickness-dependent oscillations of the phonon mediated electron-electron coupling*, Phys. Rev. B (accepted).

7. L. Komendová, **Yajiang Chen**, A. A. Shanenko, M. V. Milošević, and F. M. Peeters, *Two-band superconductors: Hidden criticality deep in the superconducting state*, Phys. Rev. Lett. **108**, 207002 (2012).

Curriculum Vitae

CURRICULUM VITAE – YAJIANG CHEN

PERSONAL INFORMATION

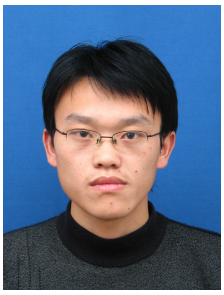

Name: **Yajiang Chen**
Birth: 17th Jun. 1984
Nationality: P. R. China
Address:
Building U211, Physics Department
Groenenborgerlaan 171,
BE-2020, Antwerpen, Belgium
Tel: +32 483252980
Email: Yajiang.Chen@ua.ac.be

EDUCATION

Ph. D. of Science in Physics Sep. 2007 - June 2012
Condensed Matter Physics group (CMT),
Physics Department, University of Antwerp, Belgium
Promoters: Dr. Arkady Shanenko, Prof. Dr. Francois Peeters
Thesis title: *Superconductivity in nanofilms and nanocylinders*.

Master of Nanophysics Sep. 2006 - Sep. 2007
Condensed Matter Physics group (CMT),
Physics Department, University of Antwerp, Belgium
Promoters: Prof. Dr. Mauro Doria, Prof. Dr. Francois Peeters
Thesis title: *Vortex Matter in a Mesoscopic Superconducting Cone*.

Bachelor of Science in Physics Sep. 2002 - Jul. 2006
Physics Department, Zhejiang University, P. R. China
Promoter: Prof. Dr. Mingxing Luo
Thesis title: *Applications of path integrals in quantum field theory*.

PUBLICATIONS

1. **Yajiang Chen**, Mauro M. Doria, and F. M. Peeters, *Vortices in a mesoscopic cone: A superconducting tip in the presence of an applied field*, Phys. Rev. B **77**, 054511 (2008).
2. **Yajiang Chen**, M. D. Croitoru, A. A. Shanenko, and F. M. Peeters, *Superconducting nanowires: quantum confinement and spatially dependent Hartree-Fock potential*, J. Phys.: Condens. Matter **21**, 435701 (2009).
3. **Yajiang Chen**, A. A. Shanenko, and F. M. Peeters, *Hollow nanocylinder: Multisubband superconductivity induced by quantum confinement*, Phys. Rev. B **81**, 134523 (2010).
4. **Yajiang Chen**, A. A. Shanenko, A. Perali, and F. M. Peeters, *Superconducting nanofilms: molecule-like pairing induced by quantum confinement*, J. Phys.: Condens. Matter **24**, 185701 (2012).
5. **Yajiang Chen**, A. A. Shanenko, M. D. Croitoru, and F. M. Peeters, *Quantum cascades in nano-engineered superconductors: geometrical, thermal and paramagnetic effects*, J. Phys.: Condens. Matter (accepted).
6. **Yajiang Chen**, A. A. Shanenko, and F. M. Peeters, *Superconducting quantum-size oscillations in Pb nanofilms: Impact of the thickness-dependent oscillations of the phonon mediated electron-electron coupling*, Phys. Rev. B (accepted).

7. L. Komendová, **Yajiang Chen**, A. A. Shanenko, M. V. Milošević, and F. M. Peeters, *Two-band superconductors: Hidden criticality deep in the superconducting state*, Phys. Rev. Lett. **108**, 207002 (2012).

SELECTED CONFERENCES

1. **Cryoconference 2008**, Series of Conferences and Training Courses Marie Curie Advanced Cryogenics Course, Madrid, Spain, 8 Sep.∼13 Sep. 2008.
2. **IAP General Meeting 2009**, Louvain-la-Neuve, Belgium, 25 Nov. 2009.
3. **DyProSo XXXII 2009**, Antwerp, Belgium, 13 Sep.∼17 Sep. 2009.
4. **Workshop: Superconductivity in nanosized system**, Lausanne, Switzerland, 5 Jul.∼8 Jul. 2010.

SKILLS AND ABILITIES

Programming: Matlab, C/C++, Fortran, COMSOL (finite element method software), MPI (message passing interface), Bash Shell
Others: Origin, Latex, Mathematica, Gnuplot, Arpack (numerical eigenvalue solver), Lapack (scientific numerical package)

LANGUAGE

English (fluent), Chinese (native)